# EXPERIMENTAL INVESTIGATION OF A GAS-EMBEDDED Z-PINCH

by

Mario Benjamin Favre Dominguez

A Thesis submitted in partial fulfilment of the requirements for the degree of Doctor of Philosophy of the University of London and for the Diploma of Membership of the Imperial College.

Plasma Physics Group
Physics Department
Imperial College
London SW7 2BZ

August 1985

TO MARINA AND JAVIERA

Abstract

The experimental investigation of a preheated laser initiated gas-embedded Z-pinch is reported. The pinch is initiated in 0.2-2.0 atmosphere hydrogen by a focussed ruby laser. The plasma is preheated by a low current for ~70ns and then heated by a fast rising current of 50kA peak ($\dot{I} \sim 10^{12} A.s^{-1}$). Holographic interferometry is used to measure time resolved electron and neutral particle density distributions and an electron temperature is inferred from time integrated soft X-ray observations.

During preheat the discharge channel is observed to expand radially with a velocity of $\sim 10^{6} cm.s^{-1}$. The electron exhibits a hollow distribution and a high density neutral layer is formed at the edge of the plasma channel as a result of a shock propagating in the background gas. For the first 10-40 ns during the main current the pinch is found to be in radial equilibrium with pinch radius 0.6-07mm. Typical electron density is about $2\text{-}5.10^{18} cm^{-3}$. A maximum Bennett temperature of 30eV is estimated, which indicates a fully diffuse current during the equilibrium. The electron line density is found to grow continuously with an e-folding time of ~20ns. The mean rate of increase of the electron line density agrees within a factor of two with the calculated rate of diffusion of neutrals into the plasma channel. Maximum stability time is about 5 Alfvén radial

transit times. An instability develops and the plasma column is transformed into an expanding helix. The observed growth rate of the instability is in good agreement with MHD calculations. The instability is observed to start inside the plasma channel as a sinusoidal perturbation of the number density around the pinch axis. An electron temperature of ~70eV is measured, which is estimated to correspond to the time when the instability develops.

CONTENTS

FIGURES

TABLES

# CHAPTER I

# INTRODUCTION

## 1.1. The Experiment

The work in this thesis describes experiments on a laser initiated gas-embedded Z-pinch. The aim of these experiments is to generate plasma conditions that make possible the ohmic heating of a linear discharge in radial equilibrium. Initiation by a laser pulse is used to generate a small diameter electric discharge in high pressure hydrogen which is then Joule heated by a fast rising current. Observations with high speed photography show three phases in the pinch evolution: preheat, equilibrium and instability. These three phases have been further investigated by holographic interferometry and observations of the soft X-ray emission from the plasma. Time resolved measurements of the electron and neutral particle distribution have been obtained and a time integrated electron temperature has been measured.

## 1.2. The Z-Pinch as a Fusion Device

The concept of the Z-pinch as a potential thermonuclear fusion device has been under investigation for many years. In the gas embedded pinch the aim is to produce a self-sustained ohmically heated axial discharge where the plasma density and containment time satisfy the Lawson

condition $n\tau \geq 10^{20} m^{-3} s$ for nuclear fusion (Lawson, 1957). Early studies, both theoretical and experimental, concluded that the Z-pinch configuration is highly susceptible to magnetohydrodynamic instabilities (Kruskal and Schwarzchild, 1954; Carruthers and Davenport, 1957). The experiments were characterized by plasma densities of $10^{19}$-$10^{23} m^{-3}$ requiring energy confinement times between $10^{-1}$ to $10^{-3}$s which are much longer than both the observed and calculated instability growth time.

The plasma focus, which in its final stage has similar characteristics to that of the Z-pinch, can achieve plasma densities of the order $10^{25} m^{-3}$ with observed stability times of the order of $10^{-7}$s (Decker and Wienecke, 1976). Despite stability times which are longer than predicted by M.H.D. theory the $10^{-5}$s confinement time required by the Lawson condition is not satisfied.

Technical and theoretical developments have made possible a new generation of pinches where higher plasma densities can be achieved with the requirement of shorter confinement times (Haines, 1981).

These developments together with the increasing technical complexities of current magnetic confinement schemes have stimulated theoretical research into the thermonuclear fusion potential of the high density Z-pinch.

Conceptual fusion reactor parameters in a Joule heated pinch have been calculated by Haines (1978) with typical plasma densities $\sim 10^{27} m^{-3}$ and confinement times of $\sim 10^{-7} s$. These conditions can be achieved in a short ($\ell \sim 0.1m$) and narrow ($r \sim 20\mu m$) deuterium discharge with a ~1MA current. Similar parameters have been calculated by Hagenson et al (1980) and Robson (1984).

## 1.3. Ohmic Heating of a Z-Pinch in Radial Equilibrium

In a Z-pinch plasma heating and confinement are both determined by the pinch current. If the current rises too slowly it allows the plasma to heat-up faster than the build-up of the confining magnetic field resulting in the expansion of the plasma column. On the other hand, if the current rises too fast the heating rate is slow compared with the build-up of the confining field and the plasma column pinches. It is expected that there is a particular current waveform which allows the plasma to be heated in radial equilibrium.

The heating process of a Z-pinch in radial equilibrium is characterized by two equations: the energy balance and the pressure balance equations:

$$\frac{d}{dt}\left[\frac{3}{2}\left(n_i kT_i + n_e kT_e\right)\right] + L_c + L_b = \eta J^2 \qquad 1\text{-}1$$

$$\frac{d}{dr}\left[n_i kT_i + n_e kT_e\right] = -JB \qquad 1\text{-}2$$

where $n_i$ and $n_e$ are the ion and electron density, k is the Boltzman constant, $T_i$ and $T_e$ are the ion and electron temperature, $L_c$ and $L_b$ are the conduction and radiation losses, $\eta$ is the plasma resistivity, J is the current density and B is the magnetic field generated by the pinch current.

Eq. 1-2 neglects any contribution from off-diagonal terms in the pressure tensor. Conduction losses can be separated into axial losses $L_a$ and radial losses $L_r$. The effect of radial losses in a gas embedded Z-pinch is discussed in Section 1.5.2.

In a high current Z-pinch the azimuthal magnetic field would tend to reduce the axial transport of heat and in the limit $\Omega_e \tau_e = \infty$, where $\Omega_e$ is the electron-cyclotron frequency and $\tau_e$ the electron collision time, the axial heat flux is carried entirely by the enthalpy flow due to the electron current (Haines, 1961). In this approximation the axial losses can be written as:

$$L_a = \frac{5}{2} n_e kT_e \frac{v_e}{z_o} \ (W \cdot m^{-3}) \qquad 1\text{-}3$$

where $v_e$ is the electron drift velocity and $z_o$ is the pinch length.

In a high temperature hydrogen plasma the radiation losses are due to bremsstrahlung radiation, which is given by (Griem, 1964):

$$L_b = 1.56 \cdot 10^{-28} \left( \frac{kT_e}{E_H} \right)^{1/2} n_e^2 \ (W \cdot m^{-3}) \qquad 1\text{-}4$$

where $E_H$ is the ionization energy of hydrogen.

Using transport coefficients calculated by Marshall (1958) in the limit $\Omega_e \tau_e \gg 1$, the resistivity is given by:

$$\eta = 9.0 \cdot 10^{-32} (kT_e)^{-3/2} \qquad 1\text{-}5$$

In a quasi-neutral hydrogen plasma $n_i = n_e = n$. If the ion and electron temperature are the same and uniform over the cross-section of the pinch, namely $T_i = T_e = T$, an integration of Eq.1-1 over the pinch section assuming a uniform current distribution and neglecting radial losses gives:

$$\frac{d}{dt}(NT) + 3.52 \cdot 10^{-20} \frac{N^2 T^{\frac{1}{2}}}{\pi a^2} + 5.2 \cdot 10^{18} \frac{T \cdot I_o}{Z_o} = 2.9 \cdot 10^{15} \frac{I_o^2}{\pi a^2 \cdot T^{3/2}} \qquad 1\text{-}6$$

where N is the plasma line density, T is the plasma temperature in eV, a is the pinch radius and $I_o$ is the pinch current. Using Ampere's law and with the same assumption for the temperature distribution, integration of Eq.1-2 over the pinch section results in the Bennett relation:

$$I_o^2 = 6.4.10^{-12}NT \qquad 1\text{-}7$$

Assuming radial equilibrium, Eqs.1-6 and 1-7 can be combined to give:

$$\frac{dT}{dt} = \frac{\phi}{T^{\frac{1}{2}}} - \psi T^{\frac{1}{2}} - \lambda T^{3/2} \qquad 1\text{-}8$$

where T is in eV and:

$$\phi = \frac{1.87.10^4}{\pi a^2} \qquad 1\text{-}9\text{-}a$$

$$\psi = 3.52.10^{-20}\,\frac{N}{\pi a^2} \qquad 1\text{-}9\text{-}b$$

$$\lambda = \frac{1.3.10^{13}}{Z_o N^{\frac{1}{2}}} \qquad 1\text{-}9\text{-}c$$

are in MKS units.

In steady state with no axial heat losses:

$$\frac{\phi}{T} = \psi T^{\frac{1}{2}} \qquad 1\text{-}10$$

giving:

$$T = \frac{5.3.10^{23}}{N} \text{ eV} \qquad 1\text{-}11$$

and

$$I = 1.8 \cdot 10^6 \text{ A} \qquad 1\text{-}12$$

Eqn.1-12 corresponds to the Pease-Braginskii limit current which balances Joule heating and bremsstrahlung radiation losses (Pease, 1957).

A steady state solution of Eq.1-8 with axial and radiation losses and including axial dependence of the plasma temperature was obtained by Haines (1961). Two extreme cases were considered: $\Omega_e \tau_e = 0$ and $\Omega_e \tau_e = \infty$, giving almost identical results. For $\Omega_e \tau_e = \infty$ the steady state temperature $T_m$ calculated by Haines is:

$$T_m^{5/2} = 1.41.10^{-3} \frac{Z_o}{\pi a^2} I\left(1 - \frac{I^2}{I^2_{p-B}}\right) \qquad 1\text{-}14$$

where $I_{p-B} = 1.68.10^6 A$ is the modified Pease-Braginskii limit.

This equation defines a steady state current which for any given set of plasma parameters balances Joule heating with axial and bremsstrahlung losses. Steady state can exist for any current below the Pease-Braginskii limit with a temperature $T_m$ given by Eq.1-14. Maximum steady state temperature is achieved when $I = \frac{I_{p-B}}{\sqrt{3}} = 0.97MA$.
If axial heat losses are neglected and only radiation losses are included in Eq.1-8:

$$\frac{dT}{dt} = \frac{\phi}{T^{\frac{1}{2}}} - \psi T^{\frac{1}{2}} \qquad 1\text{-}15$$

This equation can be integrated to give:

$$\tau_1 = \ell n\left(\frac{1+z^{\frac{1}{2}}}{1-z^{\frac{1}{2}}}\right) - \ell n\left(\frac{1+z_1^{\frac{1}{2}}}{1-z_1^{\frac{1}{2}}}\right) - 2z^{\frac{1}{2}}+2z_1^{\frac{1}{2}} \qquad 1\text{-}16$$

where:

$$z = \frac{\psi}{\phi} T \; ; \; \tau_1 = \left(\frac{\psi^3}{\phi}\right)^{\frac{1}{2}} t$$

If axial heat losses are taken into account, the integration of Eq.1-18 gives:

$$\tau_2 = (\gamma^2+4\gamma)^{-\frac{1}{2}}\{\theta_-^{\frac{1}{2}}.\ell n\left(\frac{\theta_-^{\frac{1}{2}}+x^{\frac{1}{2}}}{\theta_-^{\frac{1}{2}}-x^{\frac{1}{2}}}\right) - \theta_-^{\frac{1}{2}}.\ell n\left(\frac{\theta_-^{\frac{1}{2}}+x_1^{\frac{1}{2}}}{\theta_-^{\frac{1}{2}}-x_1^{\frac{1}{2}}}\right)$$

$$- 2\theta_+^{\frac{1}{2}}.\tan^{-1}\left(\frac{x}{\theta_+}\right)^{\frac{1}{2}} + 2\theta_+^{\frac{1}{2}}\tan^{-1}\left(\frac{x_1}{\theta_+}\right)^{\frac{1}{2}}\} \qquad 1\text{-}17$$

where:

$$x = \frac{\lambda}{4} T; \; \tau_2 = \phi \left(\frac{\lambda}{\psi}\right)^{3/2} t; \; \theta_\pm = \tfrac{1}{2}\left[\left(1 + \frac{4}{\gamma}\right)^{\frac{1}{2}} \pm 1\right] ; \gamma = \frac{4^2}{\lambda\phi}$$

Typical plasma parameters calculated by Haines (1978) for a thermonulcear pinch are:

$N = 5.6.10^{18} m^{-1}$

$z_o = 0.1m$

$a = 16.4\mu m$

These plasma parameters have been used in Eqs.1-16

and 1-17 to calculate the current profile required to heat up a Z-pinch in radial equilibrium with axial and bremsstrahlung radiation losses. Fig.1-1 shows the calculated current waveforms. The figure indicates that at early times a very large rate of rise of current is required.

At early times energy losses are not very important. If the loss terms in Eq.1-8 are neglected, the resulting equation is:

$$\frac{dT}{dt} = \frac{\phi}{T} \qquad 1\text{-}18$$

From this equation can be derived the rate of current rise $\dot{I}$ required at early times to heat-up a Z-pinch in radial equilibrium, resulting in:

$$\dot{I} \approx 1.5.10^{-2} \frac{N}{a^2.T} \quad A.s^{-1} \qquad 1\text{-}19$$

The small radius and high density of the proposed thermonculear Z-pinch requires an initial $\dot{I}$ of the order of $10^{15} - 10^{16} A.s^{-1}$ Present pulse power technology has achieved values of I of $\sim 1.5.10^{14} A.s^{-1}$ (Sincerny et al, 1985).

The theory of the equilibrium depends for its validity on the current being uniform across the pinch section. Haines (1960) has shown that for ohmic heating in

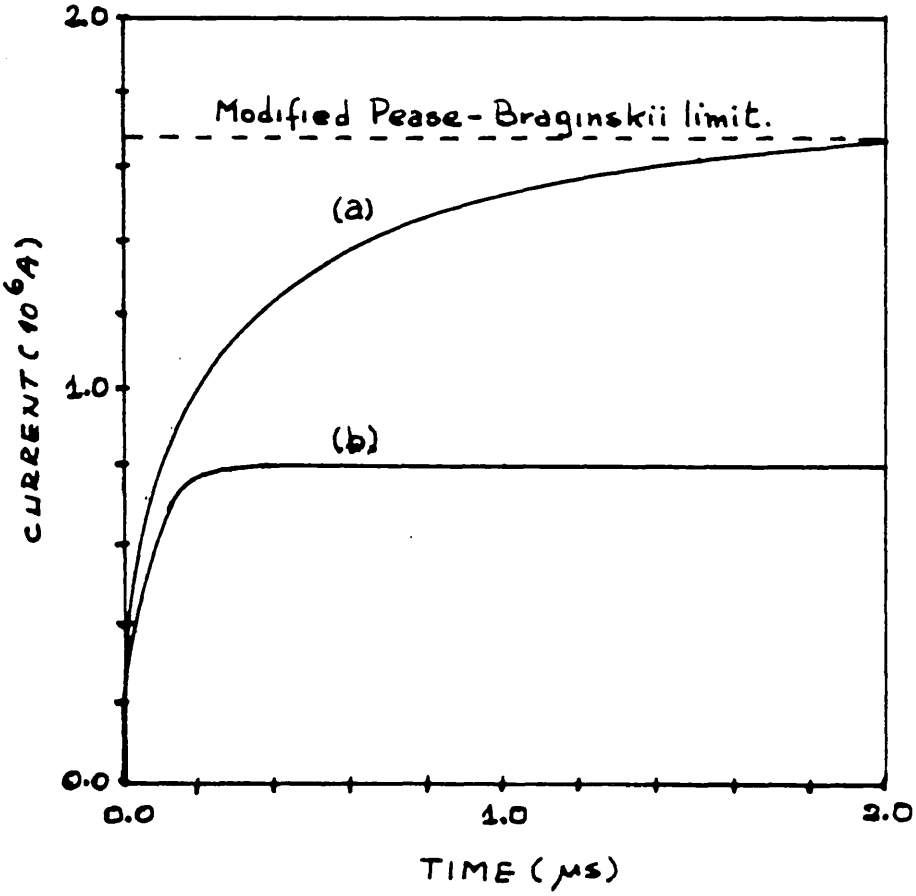


Fig. 1-1: Current time history required to heat a Z-pinch in pressure balance.
(a) Joule heating balanced with bremsstrahlung radiation losses.
(b) Joule heating balanced with bremsstrahlung radiation and axial heat losses.

pressure balance the current distribution has only a weak dependence on the pinch radius given by $I_o(1.656r/a)$ where $I_o$ is the modified Bessel function of zero order. This result indicates that the ratio between the current density at the pinch center and at the pinch boundary is 1.79, which suggests that the current density is not far from being uniform during the heating process under pressure balance.

For a high density Z-pinch with mean plasma density $\bar{n}=10^{27}-10^{28}m^{-3}$ the Lawson condition requires an energy confinement time of the order of $10^{-6}$ to $10^{-7}$s. Haines (1978) has calculated the time required to reach thermonuclear temperatures by ohmic heating of a Z-pinch in pressure balance. Neglecting losses but including equipartition of energy between electrons and ions the heating time is calculated to be 3.2 times the confinement time for the same plasma parameters. It is then required that a Z-pinch of thermonuclear interest remains stable for times of the same order as the confinement time.

## 1.4. The Stability of a Z-Pinch

It is well known that the most disruptive instabilities in a Z-pinch are the m=0 and m=1 M.H.D. modes.

In a cylindrical plasma column a perturbation from the equilibrium can be assumed to take the form:

$$\xi=\xi_o \exp(im\theta + ikz + \gamma t) \qquad 1\text{-}20$$

where $\theta$ is the azimuthal coordinate, z the axial coordinate, $k=2\pi/\lambda$ is the wave number associated with the instability and $\gamma$ the growth rate.

Kruskal and Schwarzschild (1954) have calculated the growth rate for an m=1 mode in the limits $ka >> 1$ and $ka << 1$. If the pinch is surrounded by vacuum and a skin current is assumed, the growth rates for the m=1 mode are:

$$\gamma=k\{2\frac{p_o}{\rho_o}(\ell n(\frac{2}{ka}) + 0.4228\}^{\frac{1}{2}} \quad \text{for } ka<<1 \qquad 1\text{-}21$$

and

$$\gamma=(\frac{2kp_o}{a\rho_o})^{\frac{1}{2}} \quad \text{for } ka<<1 \qquad 1\text{-}22$$

where $p_o$ is the pressure on the axis and $\rho_o$ the uniform plasma density. Eqs.1-21 and 1-22 can be written in terms of the Alfvén velocity $V_A=\frac{B_o}{(\mu_o\rho_o)^{\frac{1}{2}}}$ as:

$$\gamma=kV_A(\ell n(\frac{2}{ka}) + 0.4228)^{\frac{1}{2}} \quad \text{for } ka << 1 \qquad 1\text{-}23$$

$$\gamma=kV_A(ka)^{-\frac{1}{2}} \quad \text{for } ka >> 1 \qquad 1\text{-}24$$

Kruskal and Schwarzschild calculations predict an infinite growth rate in the zero wavelength limit.

Tayler (1957) has calculated growth rates for the m=1 M.H.D. mode assuming that the current is uniform across the pinch section. Under this condition the growth rate is found to be:

$$\omega = Y_o \cdot \frac{V_A}{a} \quad \text{for} \quad 0 \leq ka \leq \infty \qquad 1\text{-}25$$

where $0 \leq Y_o \leq 1$ is a nondimensional growth rate which has been calculated as a function of ka. Eq.1-25 indicates that the radial Alfven transit time $a/V_A$ is the characteristic 1/e growth time for the instability. Tayler's calculation predicts a finite growth rate in the zero wavelength limit.

Table 1-1 shows characteristics 1/e growth times for the m=1 M.H.D. mode in a dense Z-pinch with the same plasma parameters as used in the calculation of Fig.1-1.

Table 1-1

1/e growth times for the m=1 M.H.D. instability

| ka | $\tau_{k-s}$(s) | $\tau_T$(s) |
|---|---|---|
| 0.1 | $2.8.10^{-11}$ | $2.3.10^{-11}$ |
| 10.0 | $1.6.10^{-12}$ | $5.4.10^{-12}$ |

$\tau_{k-s}$ : Kruskal and Schwarzschild calculation

$\tau_T$ : Tayler calculation

These calculated m=1 M.H.D. growth times are several orders of magnitude shorter than the confinement time required by a dense Z-pinch of thermonuculear interest, so pinch stability has to be extended far beyond the M.H.D. limit.

Finite Larmor radius effects (F.L.R.) arise when the pinch radius is comparable to the ion Larmor radius $a_i$. Potter (1971) showed numerically that the inclusion of F.L.R. effects can extend the stability time for the m=O M.H.D. mode beyond conventional M.H.D. theory, thus explaining the enhanced stability observed in plasma focus experiments. Bowers and Haines (1971) have shown theoretically that F.L.R. effects stabilize the m=1 M.H.D. mode in a θ-pinch. The stability effect of F.L.R. on the m=1 M.H.D. mode of a Z-pinch is currently under theoretical investigation (Coppins, 1984).

The ratio of the ion Larmor radius $a_i$ to the pinch radius is given by:

$$\frac{a_i}{a} = \left( \frac{2\pi m_i}{\mu_o e} \right)^{\frac{1}{2}} \frac{1}{N_e^{\frac{1}{2}}} \qquad 1\text{-}27$$

This equation shows that for a Z-pinch in radial equilibrium $a_i/a$ depends only on the line density. For a deuterium plasma:

$$\frac{a_i}{a} = 8.08.10^{8} N_e^{-\frac{1}{2}} \qquad 1\text{-}28$$

For $N_e = 5.6.10^{-18} m^{-1}$, $a_i/a$ is calculated to be 0.34. Under these conditions conventional M.H.D. theory is inapplicable and F.L.R. stabilization might be expected.

## 1.5. The Gas Embedded Z-Pinch

It has been suggested that the high density and small plasma radius required by a thermonuclear pinch can be achieved in the gas-embedded configuration (Falthämmar, 1961; Tidman, 1971), where a narrow electric discharge is produced in a high pressure gas. The neutral gas surrounding the plasma provides insulation from the wall avoiding radiation losses due to plasma contamination with large Z-impurities.

### 1.5.1. M.H.D. instabilities in the gas embedded Z-pinch

The growth rates for M.H.D. instabilities are expected to be reduced due to the mass loading generated by the high pressure gas blanket surrounding the plasma. Manheimer et al (1973) have calculated growth rates for the m=1 M.H.D. mode in the $ka \ll 1$ approximation. For a pinch surrounded by neutral gas and without a coronal region separating the plasma and the neutrals, the growth rate they calculate is:

$$\gamma \simeq kV_A \cdot \left(\frac{\rho_p}{\rho_g}\right)^{\frac{1}{2}} \cdot \left(\ell n\left(\frac{2}{ka}\right) - 0.5772\right)^{\frac{1}{2}} \qquad 1\text{-}29$$

where $\rho_p$ and $\rho_g$ are the pinch and neutral gas density. If Eq.1-29 is compared with the Kruskal and Schwarzschild calculation Eq.1-23, the growth rate is reduced by the factor $(\rho_p/\rho_g)^{\frac{1}{2}}$. In a Z-pinch under fusion conditions the plasma density is expected to be of the order of $10^{27}m^{-3}$, which corresponds to a gas pressure of around 40 Atm. According to Eq.1-29 no significant reduction in the instability growth rate can be expected unless the background gas pressure is several orders of magnitude higher.

### 1.5.2. Energy losses in a gas embedded Z-pinch

In a gas embedded pinch losses are expected to be higher than in a vacuum pinch due to radial heat flow. Falthämmar (1961) has calculated the steady state energy and pressure balance for radial heat flow in a gas embedded Z-pinch. In this calculation Joule heating is balanced in steady state by ion thermal conduction across the magnetic field. The plasma temperature and current distribution were found to be essentially flat for $r < r_1$ and then to fall steeply to $10^{-3}$ of their values in a distance of the order of $0.1 \cdot r_1$. Haines (1982) has used the heat flow calculated by Falthammar to infer that in a high density Z-pinch the radial heat loss is expected to be only 15% of the axial loss.

Scudder (1983) has calculated numerically the steady state radial profiles of a gas embedded Z-pinch with bremsstrahlung radiation and radial ion thermal conduction in the high B field limit. A nearly uniform temperature distribution is found, followed by a sharp drop at the pinch boundary which increases as the current approaches the Pease Braginskii limit. These theoretical calculations indicate that radial heat losses do not preclude the establishment of a dense Z-pinch of thermonuclear temperature in the gas embedded configuration.

. Bremsstrahlung radiation emitted by the plasma can be absorbed by the surrounding gas leading to ionization and possibly electric breakdown. Eddleman and Hartman (1975) have studied the photon-induced breakdown in the gas embedded Z-pinch using parameters corresponding to a thermonuclear situation. Two mechanisms have been considered: (i) direct heating of the gas by photoionization and (ii) ohmic heating by photo electrons drifting in the applied electric field. Their results indicate that for most parameters of interest ohmic heating dominates. The time for the gas to become conducting is found to be strongly dependent on the 3-body recombination coefficient $\alpha$. A calculation for hydrogen indicates that a pinch of thermonuclear interest can be produced before the onset of ionization in the surrounding gas, provided that $\alpha \simeq 10^{-6} cm^{3} s^{-1}$. A plasma temperature of $10^{4} eV$ and a neutral

density of $10^{27}m^{-3}$ have been assumed in the calculation.

### 1.5.3. The initiation of a gas embedded Z-pinch

For a Z-pinch of thermonuclear interest a uniform small diameter plasma column is required. Axial electric discharges can be initiated in high pressure gases by a single-pulse laser beam (Pechacek, 1972), resulting in a low jitter small diameter discharge. This mechanism can in principle avoid the erratic behaviour associated with self-breakdown discharges.

### 1.5.4. Previous work in gas embedded Z-pinches

Table 1-2 summarizes three previous experiments in gas embedded Z-pinches. In the experiments by Smars (1964) the history of the discharge was found to depend strongly on the state of the pre-ionized column. If the diameter and particle density of the pre-ionized region were sufficiently small, pinching of the discharge was observed followed by the transformation into a spiral which then expanded into the cold neutral gas. In the experiments by Jones et al (1981), the measured plasma parameters are compared with 2-D M.H.D. calculations to deduce the plasma density. The initial radius of the plasma channel was estimated at around 150μm. The column was observed to expand continuously and to change into a helical structure around 30ns after initiation. In the experiments by Hammel et al (1983)

a uniform expanding column was observed for about 60ns with a typical initial radius of 300μm. Helical structures were observed at later times. From the measured electron density distributions a continuous increase in the electron line density has been inferred, which is interpreted as plasma accretion caused by expansion of the plasma into the surrounding neutral gas.

Common features of these experiments are:

i) Transformation of the uniform plasma column into an expanding helical structure, through an m=1 M.H.D. instability.

ii) No observation of an m=0 M.H.D. instability.

iii) Continuous expansion or pinching with no radial equilibrium.

## 1.6. Organization of this Thesis

The experimental apparatus is presented in Chapter 2. The different diagnostics applied in the experiments are described in Chapter 3. The experimental results are presented in Chapter 4, where optical and interferometric observations are used to characterize three different stages in the pinch evolution:
i) initiation and preheat, ii) equilibrium and,
iii) instability. A measurement of the electron temperature

which is time integrated over the duration of the pinch, is given in this chapter. Chapter 5 is dedicated to the interpretation of the experimental observations. Chapter 6 presents a summary of the main results and a general discussion on the shortcomings of the experiment. Future work in the gas-embedded Z-pinch is also proposed in this final chapter. Appendix A outlines the method used to calculate particle density distribution from the observed fringe shift in interferograms.

## 1.7. Units

Units are in M.K.s unless otherwise stated. However, due to common usage in the field, some parameters will be defined in other units. For example:

i) Temperatures are in electron volts.

ii) Pressures are in atmosphere or in lb/sq inch.

iii) Number densities are quoted in $cm^{-3}$.

iv) Line densities are quoted in $cm^{-1}$, some formulae use $m^{-1}$.

## 1.8. Trade Names

Some trade names have been used. These are:

i) Perspex: polymethylmethacrylate

ii) Kim-foil: $C_{16}H_{14}O_3$

Table 1-2

Previous work in gas embedded Z-pinches

| Author | Power Source | Initiation | Pre-ionization | gas | $\dot{I}$ ($A.s^{-1}$) | $n_e$ ($cm^{-3}$) | $T_e$ (eV) | a (μm) | Life time (ns) |
|---|---|---|---|---|---|---|---|---|---|
| Smars | capacitor bank | D.C. arc. | 1 A arc. | H-N-$H_e$ | $10^{11}$ | (a) $10^{19}$-$10^{20}$ | (d) 15 | 300 | 70 |
| Jones et al | Marx + transmission line | 5J Nd laser | none | H | $10^{12}$ | (b) $10^{20}$ | (e) 100-150 | 150 | 20 |
| Hammel et al | Marx + transmission line | 10J Nd Gag laser | none | H | $5.10^{12}$ | (c) $10^{20}$ | (e) 200-800 | 300 | 60 |

(a) : measured spectroscopically

(b) : deduced from a 2-D MHD simulation

(c) : measured with Moire-schlieren technique

(d) : measured spectroscopically

(e) : measured with two filter X-ray ratio technique.

# CHAPTER II

## The Apparatus

### 2.1. Introduction

In this chapter the current generator and Z-pinch are described.

The current generator consists of a 4-capacitor conventional Marx which charges a two section, 3Ω water dielectric coaxial transmission line. The two sections are separated by a $SF_6$ self breakdown switch. Typical operational conditions for the generator were 120-150kV at the Marx output with a 40-50kA, 100ns half-width current pulse delivered into a short circuit load.

The generator diagnostics consist of a resistor divider at the Marx output to monitor the charging of the transmission line and Marx performance, a capacitor divider to measure the voltage across the load at the end of the transmission line and a single turn coil at the return electrode in the pinch assembly to measure the pinch current.

## 2.2. The Current Generator

Fig. 2-1 is a diagram of the current generator with the location of the electric monitors indicated. The laser shown is used for pinch initiation as well as diagnostics.

## 2.3. The Marx

The general characteristics of the Marx are:

4 capacitors, 0.5μF, 100kV maximum voltage.
Maximum operational voltage: 28kV per capacitor.
Series capacity: 125nF
Inductance: 3μH (inferred)
Jitter: 40ns (measured).

In Fig. 2-2 is shown the electric circuit of the Marx. It is designed for +/- charging. Resistors are made of $CuSO_4$ solution inside p.v.c. tubes. Two spark gaps connect the capacitors in series when the Marx is erected. Fig. 2-3 is a cross-section diagram of a spark gap with the connections to the capacitors and trigger generator. The mid plane electrode is used for trigger. The spark gaps are located one on top of the other inside a column. Nitrogen and dry air are used as insulating gas. A +/- 50kV power supply unit is used to charge the Marx.

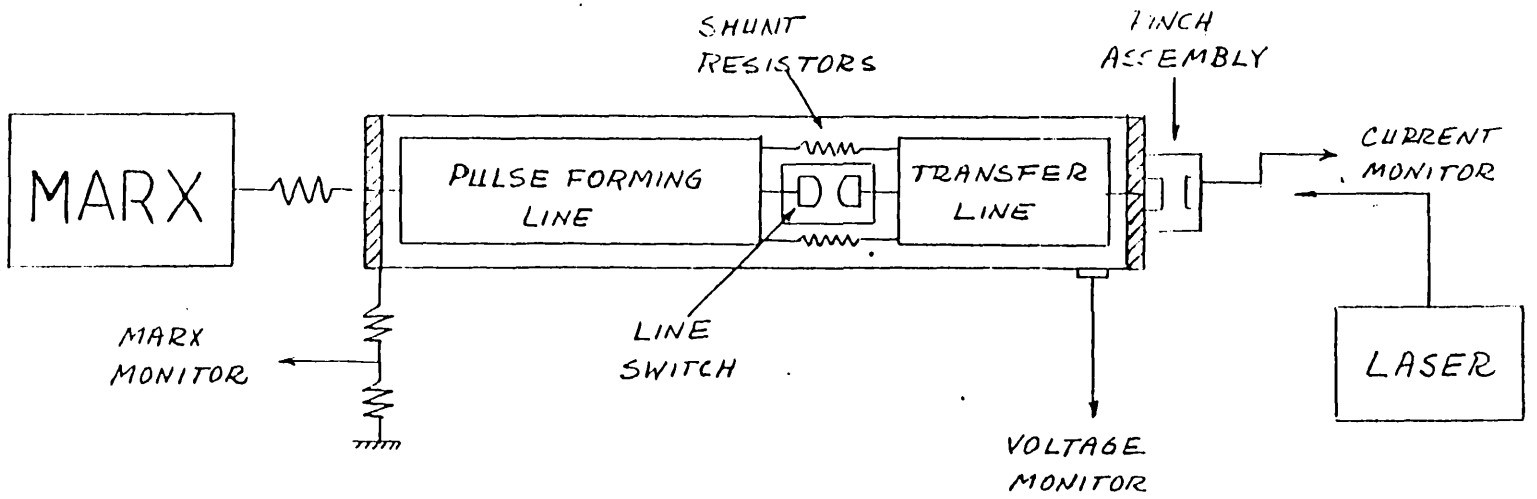


Fig. 2-1: the Current Generator.

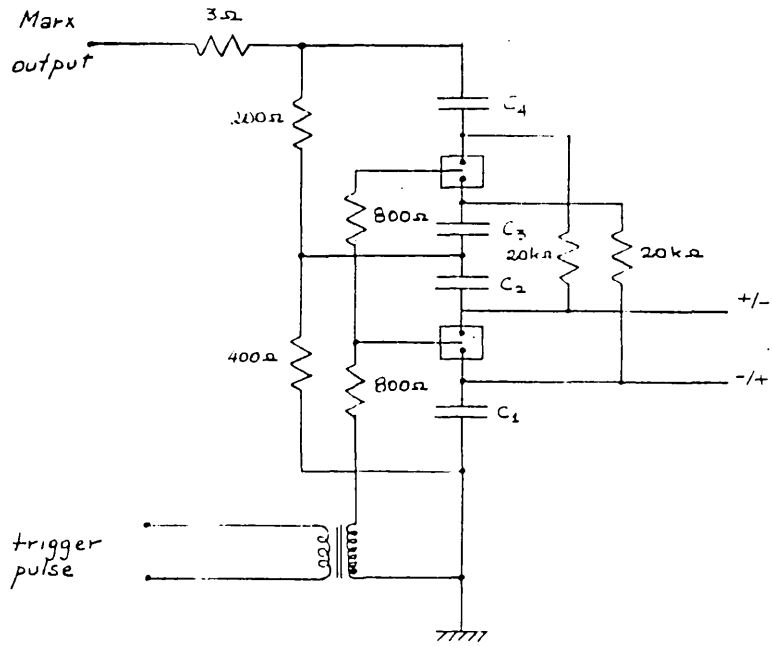


Fig. 2-2: Marx electric circuit.

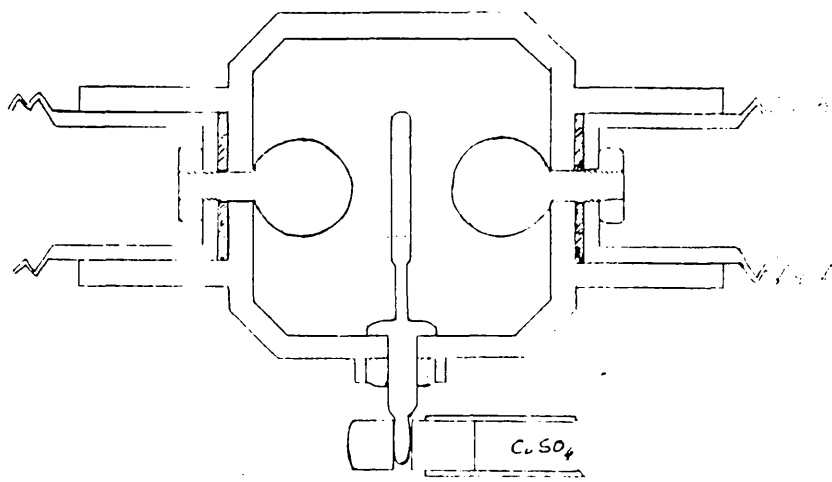


Fig. 2-3: cross-section view of a Marx spark-gap.

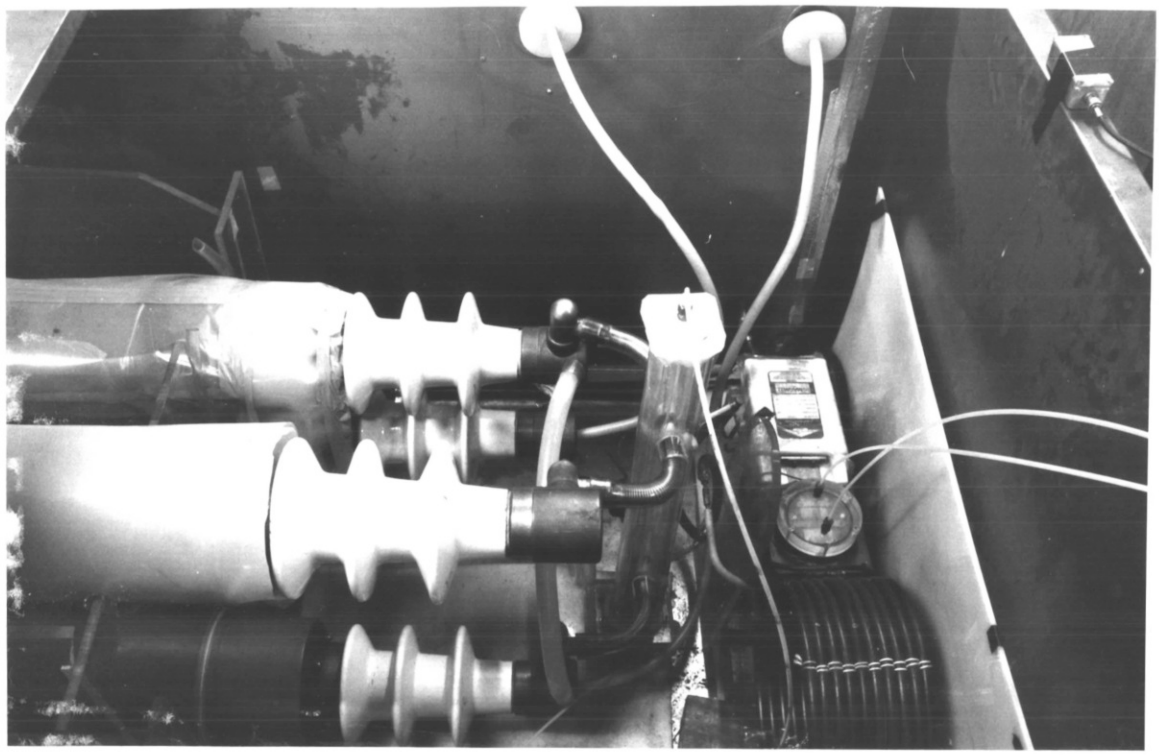

Fig. 2-4: Photograph of the Marx. The Marx trigger column and four cylindrical capacitors can be seen.

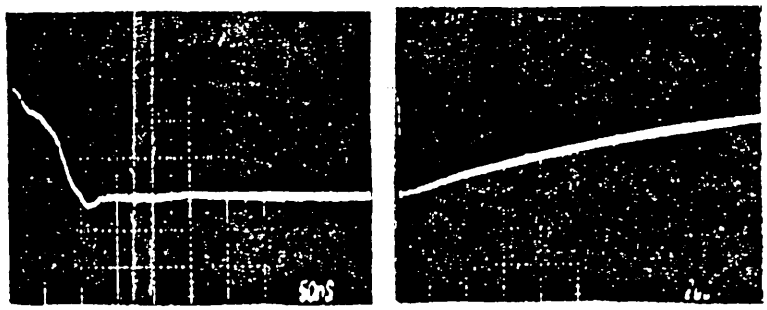

(a) (b)

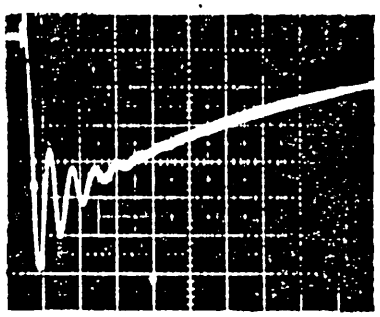

(c)

Fig. 2-5: (a) Marx output into open circuit: 30 kV/div; 50 ns/div. (b) Marx output into open circuit: 30 kV/div; 2$\mu$s/div. (c) Marx output into transmission line with open switch: 20 kV/div; 2$\mu$s/div.

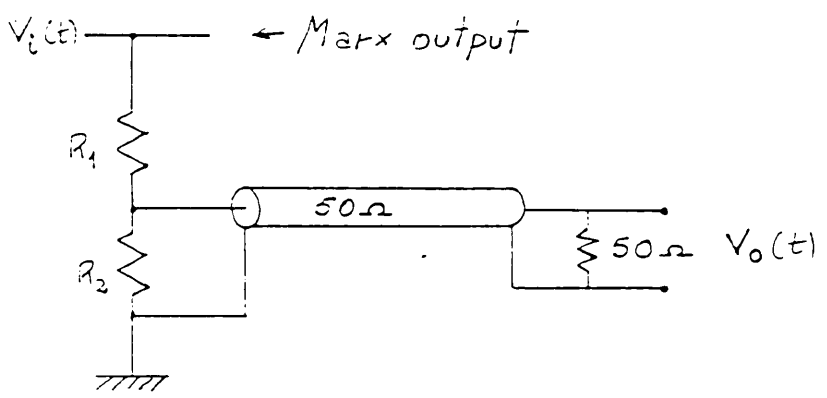


Fig 2-6:Marx voltage monitor.

A photograph of the Marx is shown in Fig. 2-4. The capacitors, spark gap column and trigger transformer are housed in a steel case to reduce E-M interference. Due to air breakdown the charging voltage is limited to 30kV.

The Marx output voltage waveform into an open circuit and the Marx discharge voltage waveform into the transmission line with the line switch open are shown in Fig. 2-5.

### 2.3.1. The Marx voltage monitor

A resistive divider connected to the Marx output is used to monitor the Marx voltage. A diagram of the divider is shown in Fig. 2-6. It consists of a $CuSO_4$ resistor of nominal resistance 2kΩ, six 120Ω carbon resistors connected in parallel and a 50Ω terminated cable. Calibration was performed with a 200V, 1μs voltage pulse. The duration of the pulse approximates the characteristic charging time of the transmission line. The measured sensitivity is 1V/kV in excellent agreement with the design parameters.

## 2.4. The Transmission Line

Fig. 2-7 is a photograph of the transmission line and pinch assembly. It is a water dielectric coaxial line with the pulse forming and a transfer section separated by a

self-breakdown switch. The characteristics of the line are:

Pulse forming section:

Impedance: z = 3.2Ω (measured)

Capacity: c = 12nF (calculated)

Inductance: L = 90nH (calculated)

Transit time: $\tau$ = 33ns

Transfer section:

Impedance: z = 3.2Ω (measured)

Capacity: c = 3.5nF (calculated

Industance: L = 26nH (calculated)

Transit time: $\tau$ = 9.5ns

The line was designed to stand 150kV with a charging time of 1μs. It is made of brass with a 15cm square section outer conductor and a 5cm radius cylindrical section inner conductor. The water is continuously circulated through a resin ion exchange bed (Elga Products) which maintains a volume resistivity of the order of $10^4 \Omega.m$.

A schematic view of the line is shown in Fig. 2-8. The interface between the Marx case and the line is a 2.5cm thick, 65cm square piece of perspex followed by a water dielectric reduction section. The front end of the line is a 2.5cm thick piece of perspex.

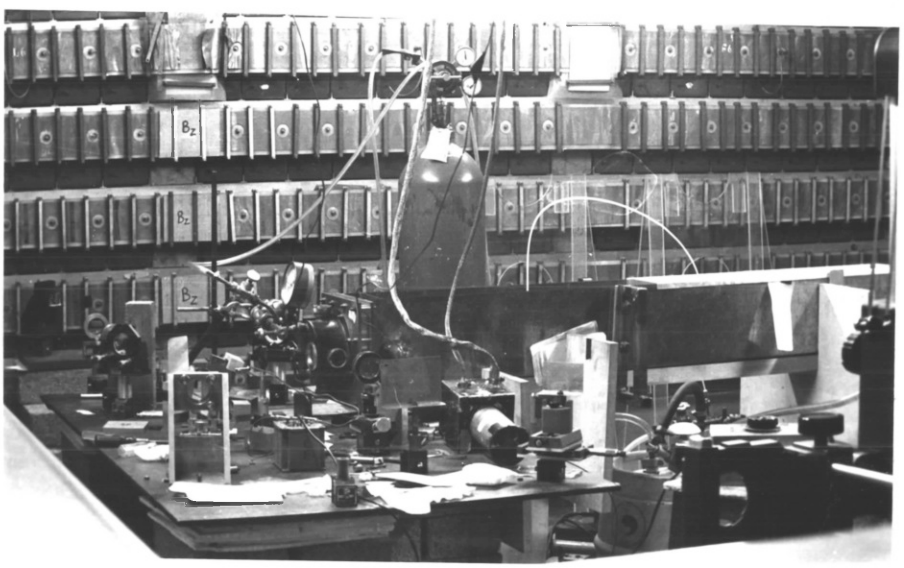

Fig. 2-7: Photograph of the transmission line. Some of the optical components for holographic interferometry can be seen in the picture.

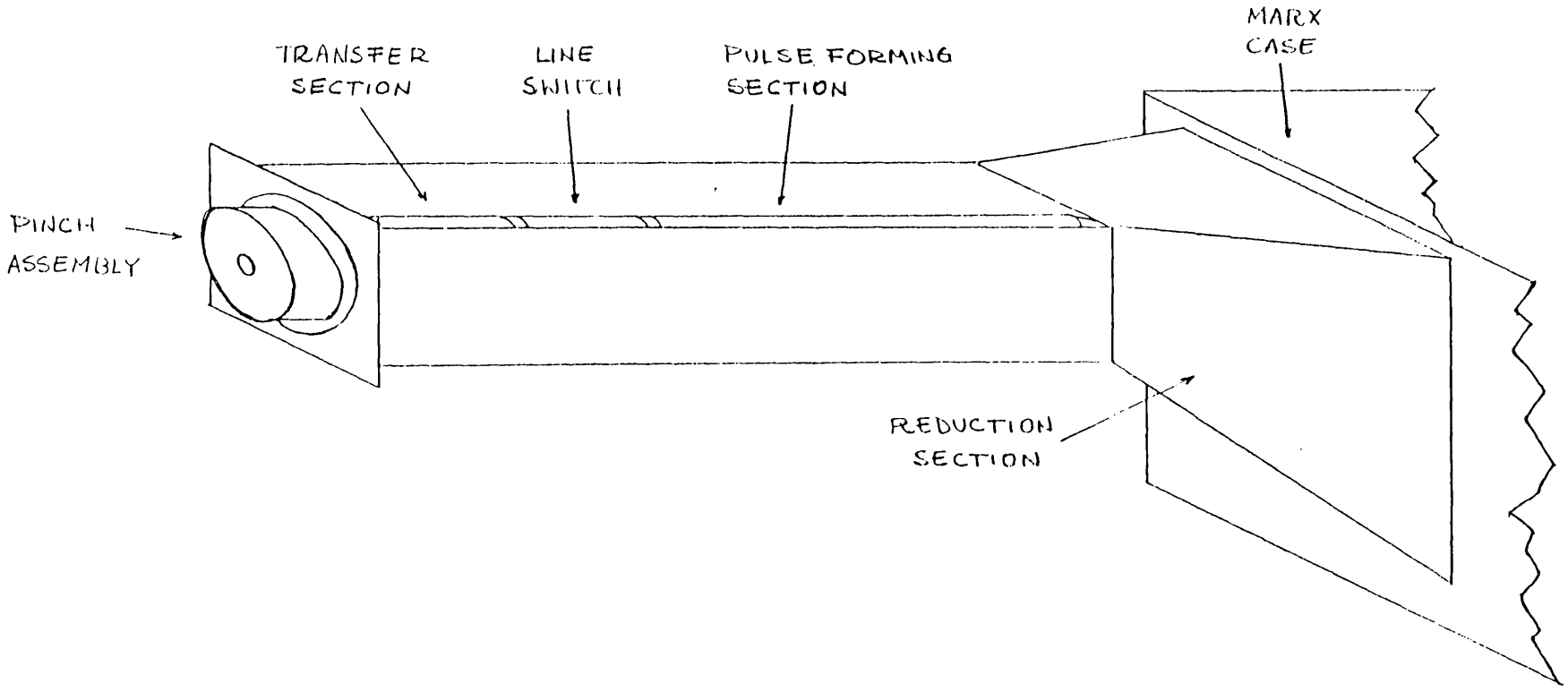


Fig. 2-8: projection of the transmission line.

### 2.4.1. The line switch

The characteristics of the switch are:

| | |
|---|---|
| Inductance: | L = 50nH (calculated) |
| Jitter: | 20ns |
| Self-breakdown voltage: | 100-150kV (pulsed) |
| Operating pressure: | 10-30p.s.i.g. $SF_6$ |

Fig. 2-9 is a cross-section diagram of the switch. It has a smaller jitter than a self-breakdown water spark gap used in the early stages of the experiment.

The insulator of the switch was machined from a solid cast block of annealed perspex. The brass electrodes are spring loaded to absorb the breakdown shock. The spark gap can be laser triggered if focussing lenses are located inside the hollow electrode. In these experiments the switch was operated at pressures ranging from 10 to 15p.s.i.g. (above atmospheric pressure) in $SF_6$, with 1cm electrode separation.

### 2.4.2. Preheating circuit

Four $CuSO_4$ resistors, of nominal value 800Ω, across the line switch allow the transfer section to be charged up to a voltage that is a fraction of the voltage in the pulse forming section. Discharging of the transfer section into

the plasma filament provides a preheating current of around 5kA peak and ~80ns ringing period.

The period and maximum current of the preheating discharge are consistent with the L-C characteristics of the circuit formed by the plasma filament, pinch chamber and transfer section of the line. The combined inductance of the plasma filament and pinch chamber is calculated to be $L_e \simeq 50nH$. Using the calculated capacity of the transfer section, the period $T_p$ and peak current $I_p$ of the preheating discharge are calculated to be:

$$T_p = 2\pi \sqrt{L_e . c} \simeq 83ns$$

$$I_p = V_p \sqrt{\frac{c}{L_e}} \simeq 5.3kA$$

where $V_p = 2.10^4 kV$ is the typical charging voltage for the transfer section.

The voltage in the transfer section agrees with the results of a numerical simulation of the performance of the line. The observed and predicted voltage waveforms are presented in Section 2.7.

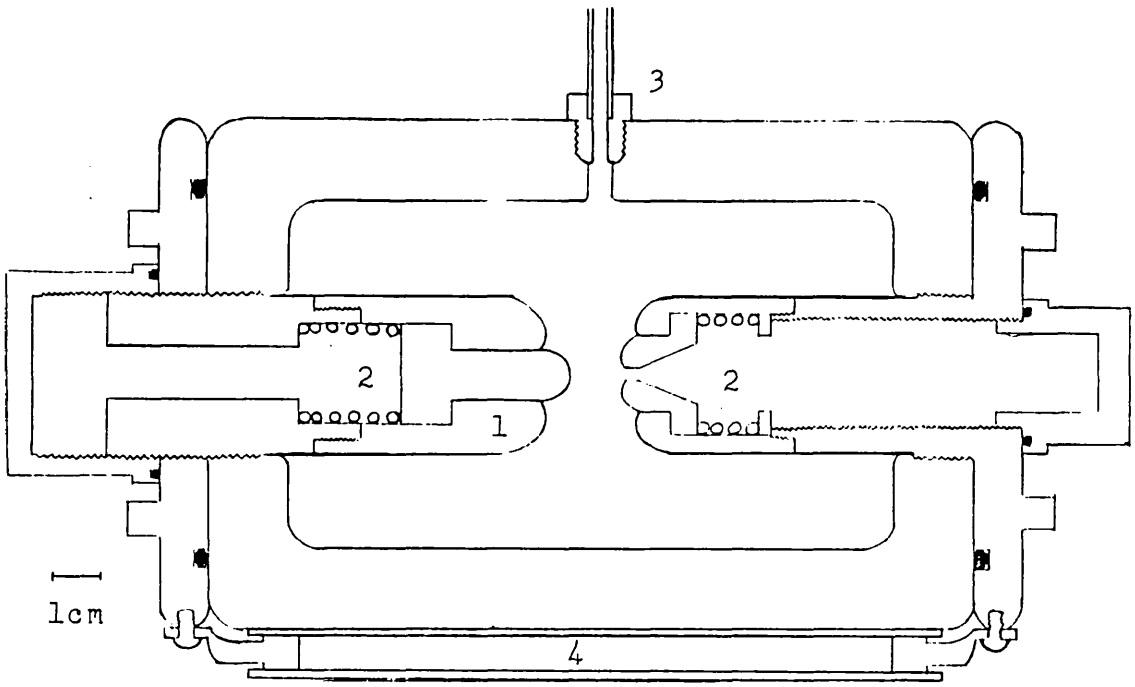


Fig. 2-9: Transmission line switch.
(1) Live electrode. (2) Spring. (3) Gas in-let.
(4) Preheating resistor.

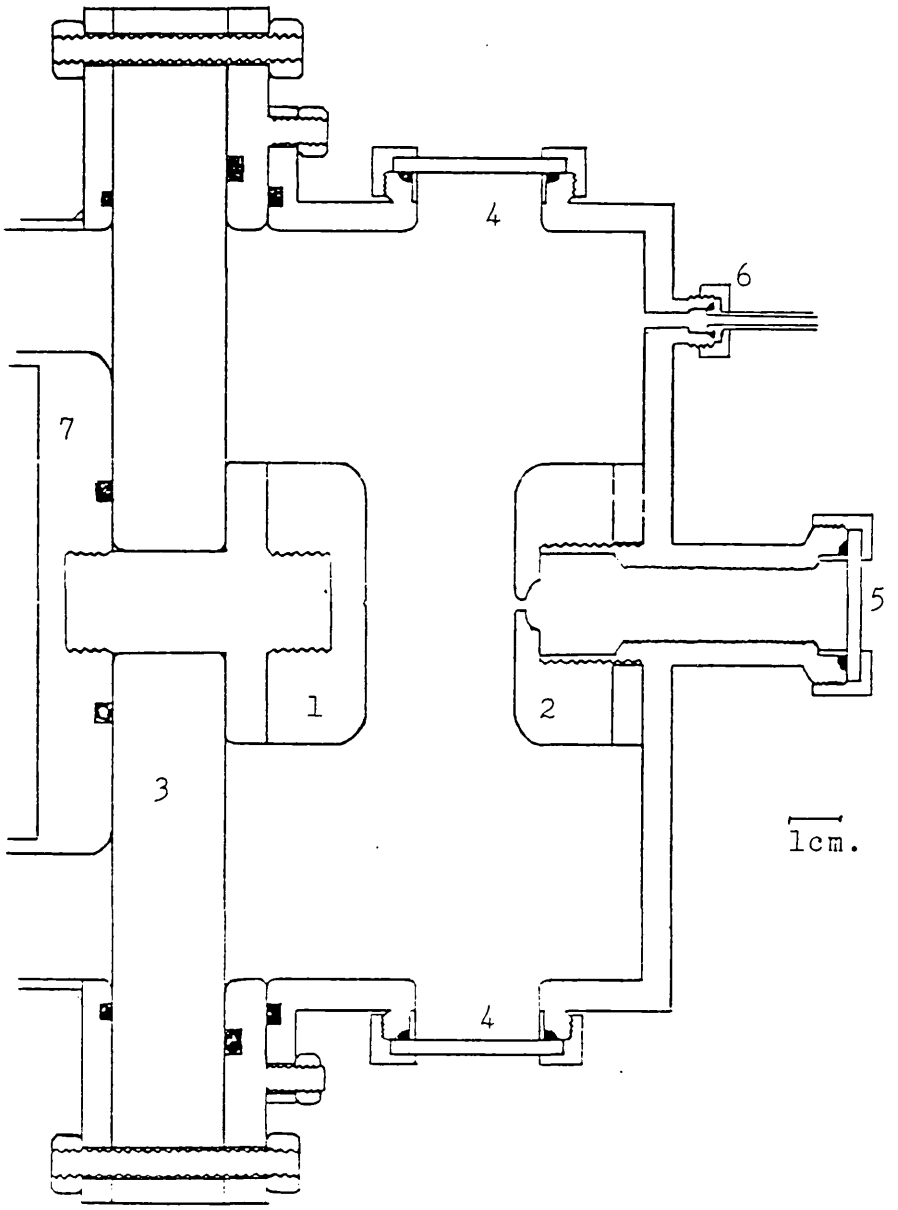


Fig. 2-10: Pinch assembly.
(1) Live electrode. (2) Return electrode.
(3) Insulator. (4) Observation port.
(5) Axial port for laser initiation.
(6) Gas in-let. (7) Inner conductor of the transmission line.

## 2.5. Pinch Assembly

Fig. 2-10 is a cross-section diagram of the pinch assembly. The main characteristics are:

Radius: 7.5cm

Length: 7.5cm

Electrode separation: 3cm (adjustable)

Operational pressure: 0.2 - 2.0 Atm

A 1.8cm diameter axial window allows a laser beam to be focussed onto the live electrode through a 2mm diameter hole in the return electrode.

## 2.6. Electric monitoring

### 2.6.1. Voltage monitor

Fig. 2-11 is a cross-section diagram of the voltage monitor. A flat ended brass cylinder iscapacitivelycoupled through the water dielectric to the inner conductor of the line and the outer case of the monitor. The equivalent electric circuit is shown in Fig. 2-12, where $C_1$ and $R_1$ represent the capacity and resistance of the dielectric across the line and $C_2$ and $R_2$ represent the capacity and resistance of the dielectric across the monitor. With the series resistance R, the input voltage $V_i$ and the output voltage $V_o$ are related by:

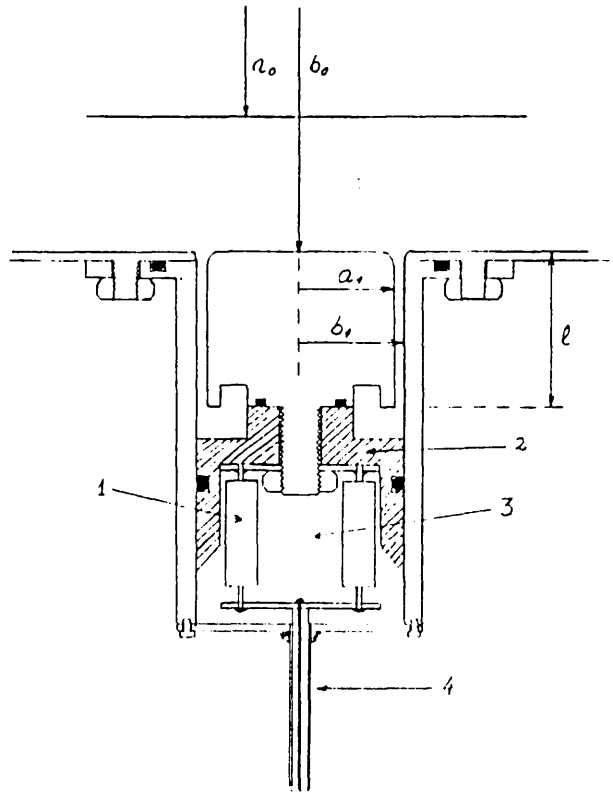


Fig. 2-11: cross-section of the voltage monitor. Dimensions: a =5 cm, b =7.5 cm, a =1.75 cm, b =1.95 cm, l=2.9 cm. (1) 8.2 kΩ resistor (8 in paralell). (2) Nylon insulator. (3) Silicon rubber. (4) Solid coaxial 50 Ω signal cable.

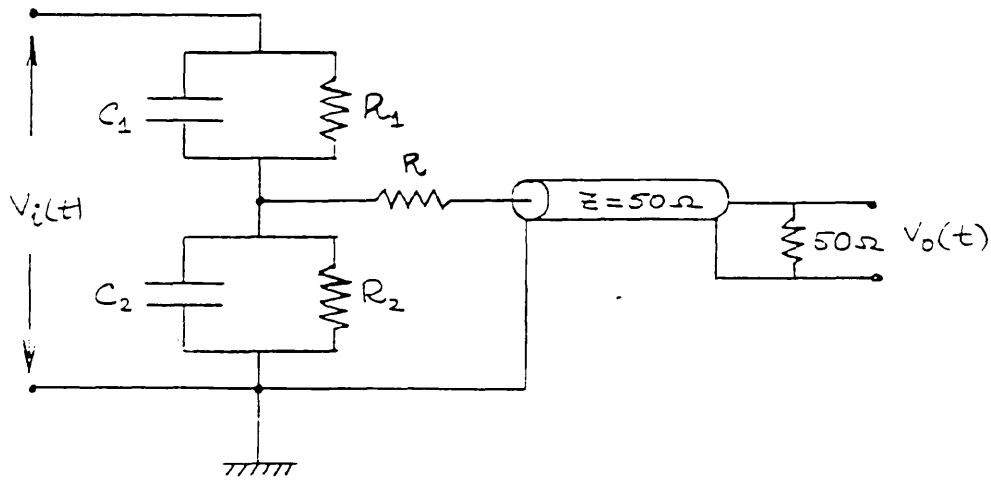


Fig. 2-12: Electric circuit for the vlotage monitor.

$$\frac{dV_i}{dt} + \frac{1}{C_1 R_1} V_i = \frac{C_1+C_2}{C_1} \cdot \frac{R + Z}{Z} \cdot \frac{dV_o}{dt} + \frac{1}{\tau^*} V_o \qquad 2\text{-}1$$

where

$$\frac{1}{\tau^*} = \frac{1}{C_1 Z} \{1 + 2 \cdot \frac{R + Z}{R_1} + \frac{R + Z}{R_2} \} \qquad 2\text{-}2$$

If $\tau$ is the longest time of interest and:

$$\tau << \min \{C_1 . R_1 ; \tau^*\} \qquad 2\text{-}3$$

Eq. 2-1 can be integrated to give:

$$V_o(t) = \frac{C_1}{C_1 + C_2} \cdot \frac{Z}{Z + R} V_i(t) \qquad 2\text{-}4$$

With the circuit parameters shown in Fig. 2-11, Eq. 2-3 is satisfied if $\tau << 6.10^{-6}$s. This time is about one order of magnitude longer than the characteristic times associated with the experiment.

Eq. 2-4 gives $V_o(t) = 8.8.10^{-4} V_i(t)$

Two different voltage signals were fed into the transfer section to check the dividing ratio of the monitor:

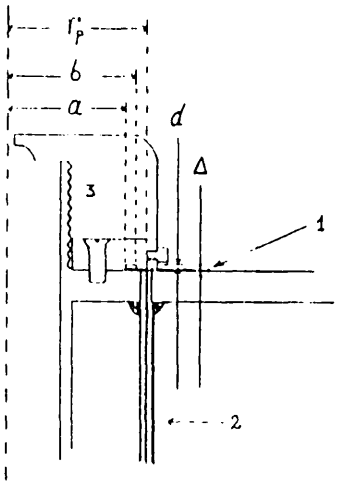


Fig. 2-13: Cross-section of the current monitor. Dimensions: $r_p$=2.45 cm, a=2.18 cm, b=2.42 cm, d=0.203 cm, Δ=0.02 cm. (1) Insulator. (2) Solid coaxial cable. (3) Return electrode.

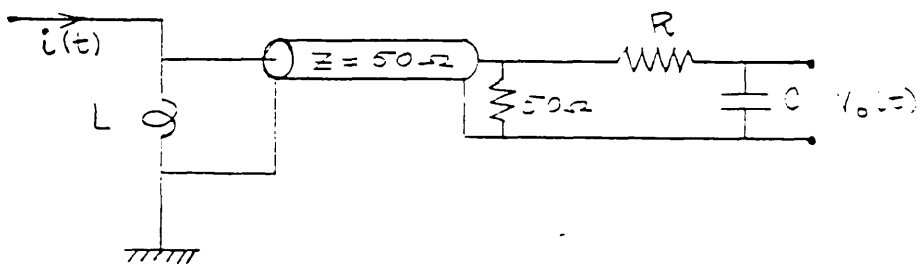


Fig. 2-14: Electric circuit for the current monitor.

(i) a 200V, 1μs voltage pulse and, (ii) a 12.5V, 68ns period oscillating signal. The characteristic times of the calibration signals are similar to those of the experiment. In both cases the ratio was 1.4V/kV.

## 2.6.2. The current monitor

Fig. 2-13 is a cross-section diagram of the current monitor. This is similar to that described by Ekdahl (1980). It consists of a coaxial annular channel machined into the return electrode. The insulator causes the current to flow around the channel and the variation of the magnetic flux inside the channel induces a voltage across the pick-up point. The equivalent circuit of the monitor is shown in Fig.2-14. The equation for the circuit is:

$$L \frac{di}{dt} = RC \frac{dV_o}{dt} + V_o \qquad 2\text{-}5$$

where L is the inductance of the channel plus insulator gap and is given by:

$$L = \frac{\mu_o}{2\pi} (d+\Delta) \ln \left( \frac{b}{c} \right) + \frac{\mu_o}{2\pi} \Delta \ln \left( \frac{b}{a} \right) \qquad 2\text{-}6$$

The notation of Fig. 2-13 has been used. Eq. 2-6 gives L = 45.8pH. If $\tau$ is the longest time of interest and

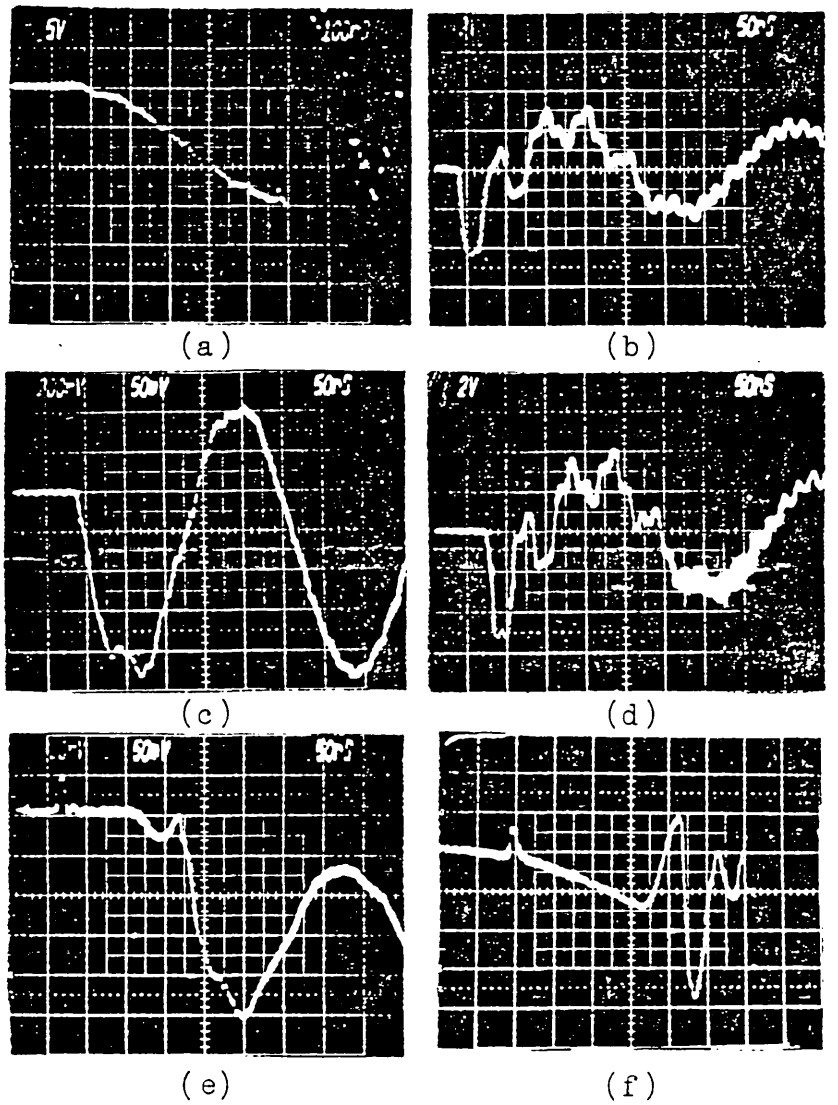


Fig. 2-15: Characteristic waveforms.
(a) Line charging voltage: 50 kV/div; 100 ns/div.
(b) Voltage into short-circuit: 28 kV/div; 50 ns/div.
(c) Current into short-circuit: 8.8 kA/div; 50 ns/div.
(d) dI/dt into short-circuit: 4.4 $10^{11}$ $A \cdot s^{-1}$/div; 50 ns/div.
(e) Current into plasma: 8.8 kA/div; 50 ns/div.
(f) Voltage into plasma: 14 kV/div; 50 ns/div.

$\tau << RC$, Eq.2-5 can be integrated to give:

$$i(t) = \frac{RC}{L} V_o(t) \qquad 2\text{-}7$$

With an integration time RC = 2μs the calculated ratio is 43.7kA/V. A calibration was performed by discharging a capacitor through the anode electrode. A 2nF capacitor charged up to 1kV was used, generating a calibration signal with a period of ~100ns, which is of the order of the characteristic times of the experiment. The measured ratio was 4.2kA/V, with a 2μs integration time.

## 2.7. Voltage and Current Waveforms

Characteristic waveforms of the current generator are shown in Fig. 2-15.

Peak voltage in the line is 150kV with 28kV charging voltage on the Marx. The line charging time up to switch breakdown is 520ns.

The voltage monitor signal and the unintegrated current monitor signal corresponding to a short-circuit load are almost identical, which is indicative of a good monitor response.

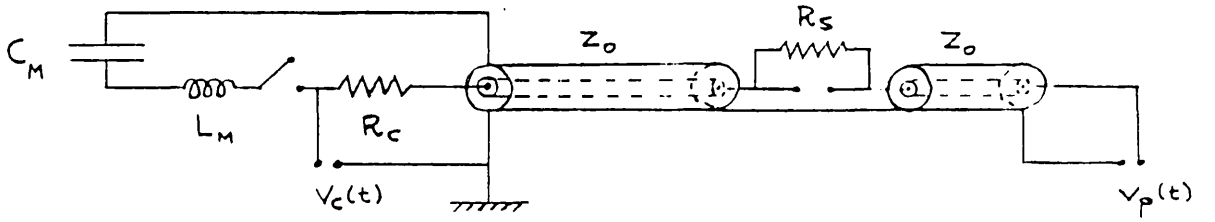


Fig. 2-16: Electric circuit assumed in the line simulation, simulation.

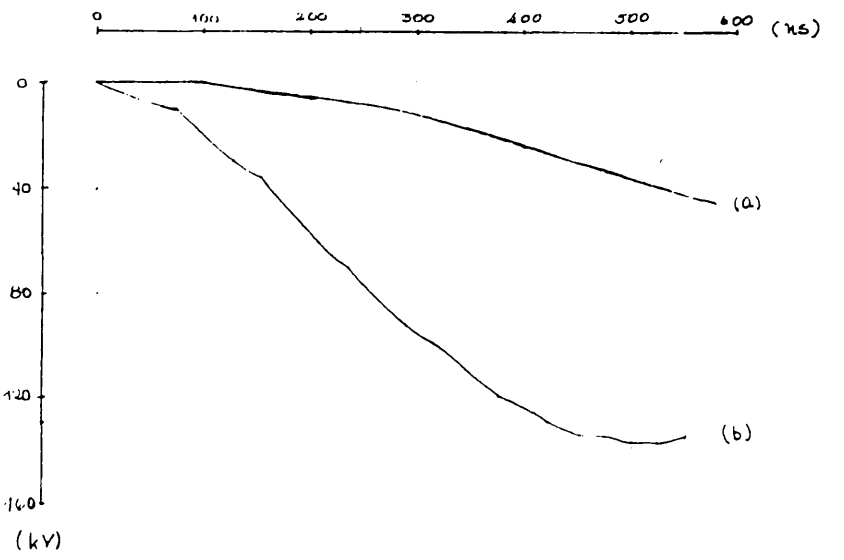


Fig. 2-17: Simulated voltage waveforms. Conditions: 28 kV Marx charging voltage, 250Ω across the line switch. (a) Line charging voltage. (b) Voltage across the end of the transmission line.

The unintegrated current monitor signal indicates that a maximum $dI/dt = 1.14.10^{12}A.s^{-1}$ is achieved around 5ns after the initiation of the current pulse. Using the voltage monitor signal and a calculated inductance of the short circuit load, a maximum $dI/dt \simeq 1.4.10^{12}A.s^{-1}$ is estimated, showing good agreement with the unintegrated current monitor signal.

With a charging voltage on the Marx of 25kV a maximum current of 40kA is delivered into a short circuit load. Rise time to 90% of peak current is 40ns. The current reverses in 150ns.

Current and voltage waveforms for a plasma filament are shown. Filling pressure in the pinch chamber was 0.33 Atm and the Marx was charged up to 28kV. The current waveform shows a 55ns, 5.3kA peak preheating current pulse followed by the main current pulse. Maximum current is 45.8kA with 40ns rise time to 80% of plasma current. The fact that the plasma current does not reverse after peak is attributed to crow-barring across insulator ("3", Fig. 2-10). The voltage monitor signal shows the pre-breakdown voltage. The voltage at the time of breakdown is 19.6kV. A maximum voltage of 53.2kV is reached 10ns after the main current starts. Using a calculated inductance of the plasma filament, maximum $dI/dt$ is estimated to be $1.1.10^{12}A.s^{-1}$.

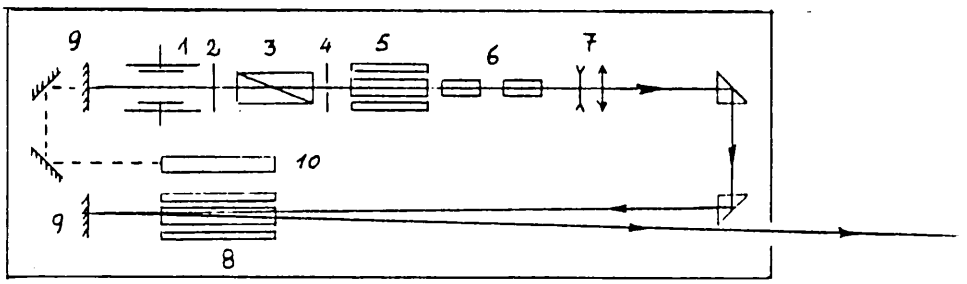


Fig. 2-18: Diagram of the laser.
(1) Oscillator Pockell's cell. (2) $\lambda/4$ plate.
(3) Nicol's prism. (4) Pin-hole. (5) Oscillator.
(6) Etalons. (7) Beam expander. (8) Amplifier.
(9) 100% reflecting mirror. (10) He-Ne laser.

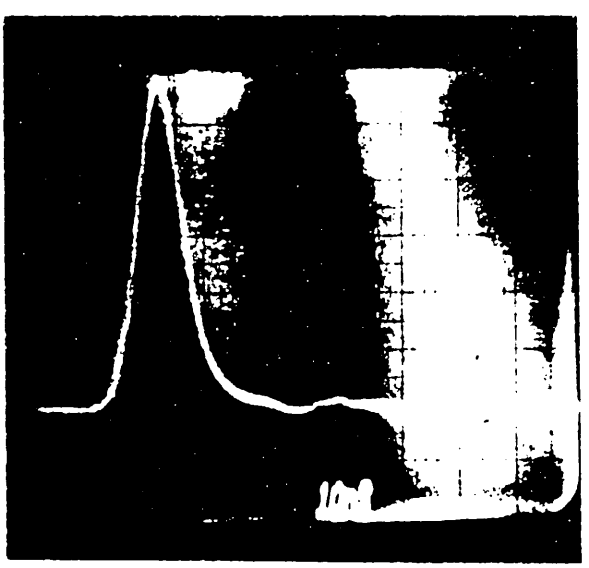

Fig. 2-19: Oscilloscope trace of the laser pulse at the output from the oscillator; 10 ns/div.

A numerical simulation of the charging of the line was carried out to investigate the relation between the charging voltage in the transfer section and the resistor across the line switch. The electric circuit used in the modelling is shown in Fig.2-16. The calculated voltage waveforms are shown in Fig.2-17. Conditions are: 28kV Marx charging voltage and a 250Ω resistor across the switch. The simulation shows good agreement with the line charging voltage and the voltage monitor pre-breakdown signal shown in Fig.2-15.

## 2.8. The Laser

A Q-switched ruby laser (Quantel) is used for pinch initiation and diagnostics. It consists of an oscillator and a double pass amplifier. Main characteristics of the laser are:

| | |
|---|---|
| Oscillator output: | 65mJ with H.T. = 1.85kV |
| Amplifier output: | 1.4J with H.T. = 1.4kV |
| F.W.H.M.: | 8 ns |
| Spot size: | $\phi \approx 1$cm (at the output from laser housing |
| Power density: | $1.3 - 10^{8}$W.cm$^{2}$ |
| Divergence: | $6.10^{-4}$rad. |

Fig.2-18 is a diagram of the laser system. A reflection from one of the optical components inside the

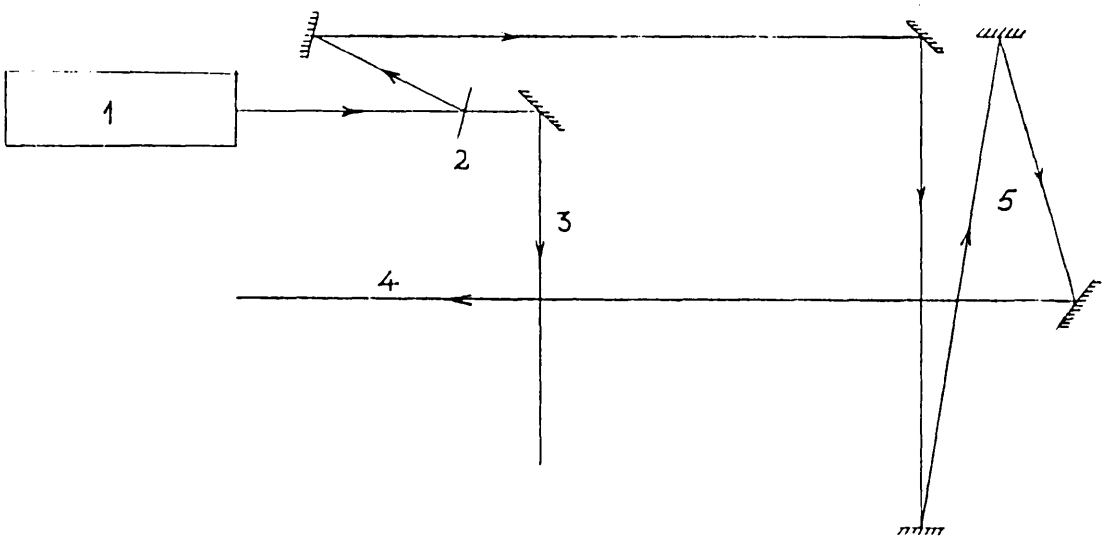


Fig. 2-20: Laser beam path.
(1) Laser housing.
(2) Beam splitter.
(3) 0.8 J laser beam for pinch initiation.
(4) 80 mJ diagnostic laser beam.
(5) Delay path.

laser housing is used to monitor the laser beam, providing a time marker for the experiment.

Fig.2-19 is an oscilloscope trace corresponding to a laser pulse delivered by the oscillator.

Fig.2-20 is a diagram of the laser beam path. The beam splitter provides a 80mJ pulse which is used for diagnostics.

## 2.9. Firing Sequence

Fig.2-21 is a block diagram of the firing sequence. The Marx trigger delay is ~1μs. The line charging time is ~600ns. The laser oscillator Pockell's cell trigger signal is used to initiate the Marx firing sequence.

The firing sequence is as follows:

1. At t=0 the laser amplifier flash lamp is triggered.

2. At $t_1$=350μs the laser oscillator flash lamp is triggered.

3. At $t_2$=650μs + $t_1$ the Marx is triggered.

4. At $t_3 \approx 1.5\mu s + t_2$ the oscillator Pockell's cell is triggered and an electric discharge is initiated across the pinch electrodes. Energy stored in the

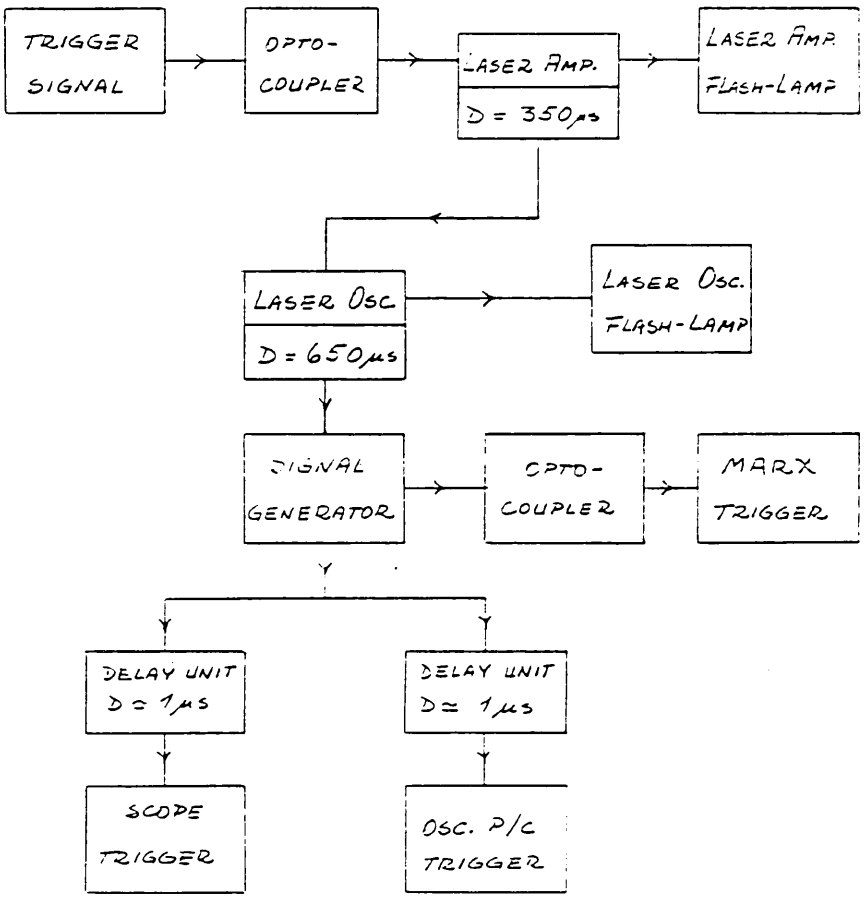


Fig. 2-21: Block diagram of the firing sequence.

transfer section is discharged to generate a preheat current.

5. At $t_4 \approx 70ns + t_3$ the line switch closes and the main current powered by the pulse forming section of the line is applied to heat the plasma channel.

Initiation of the main current has a 5ns jitter with respect to the initiating laser pulse.

# CHAPTER III

## The Diagnostics

### 3.1. Introduction

In this chapter are described the different plasma diagnostics used in the experiment.

The diagnostics are:

i) Streak and framing photography, which provides information about the pinch dynamics;

ii) Schlieren photography, which allows the location and evolution of particle density gradients to be observed;

iii) Holographic interferometry which gives time resolved measurements of the particle density distributions;

iv) Scintillator photo-multiplier observations of the soft X-ray emission to investigate the temperature evolution; and

v) Two filter soft X-ray pinhole photography which allows the electron temperature to be inferred.

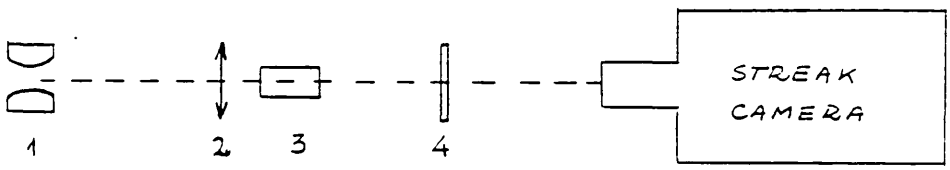


Fig. 3-1 : Streak-camera set-up.
(1) Pinch. (2) Relay lens. (3) Dove prism.
(4) Groud glass screen.

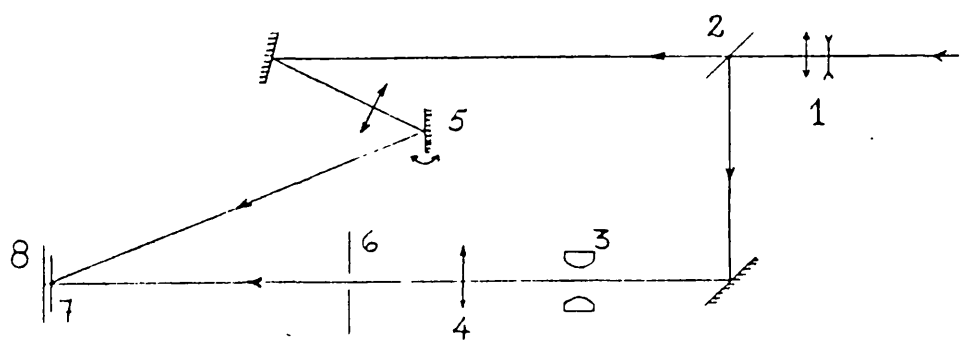


Fig. 3-2 : Optical set-up for holographic interferometry.
(1) Beam expander. (2) 50% beam splitter.
(3) Pinch assembly. (4) Imaging lens.
(5) Tilting mirror. (6) Diaphragm. (7) Red filter.
(8) Film.

## 3.2. High Speed Photography

A Hadland Imacon 675 camera with an image intensifier was used to take side-on streak and framing photographs of the pinch. Typical streak speeds of 50 to 100ns.cm$^{-1}$ and framing rates of $7.5.10^7$ and $3.8.10^8$ frames.s$^{-1}$ were used.

Figure 3-1 is a diagram of the set-up. To increase magnification a relay lens was used in both modes. A typical magnification of 7:1 was used. In framing mode the pinch was imaged onto a ground glass screen and the pinch image rotated by 90° with a Dove prism. This procedure allowed vertical images to be framed. The ground glass screen was used to overcome alignment problems.

## 3.3. Holographic Interferometry

Interferograms of the pinch were obtained using image plane holography (Ostrovsky et al, 1980). With this technique the object is focussed onto the plane of the hologram, so the amplitude-phase distribution of the probing beam at the object is reproduced on a one-to-one basis on the hologram.

Fig. 3-2 is a diagram of the optical set-up. Two successive holograms are recorded on the same holographic plate, the first with the pinch chamber filled with hydrogen at the required pressure, the second at a predetermined time

during the pinch discharge. When the resulting hologram is illuminated these two images interfere as a result of the difference in optical path due to the plasma.

Background interference fringes are produced by tilting one of the mirrors in the reference beam path between exposures. This background fringe pattern is used as a reference frame for the fringe shift introduced by the plasma.

A 20cm focal length lens was used to focus the pinch onto the hologram plane giving a 6:1 magnification. Holograms were recorded on Agfa 10E75 holographic film. Processing of the film was as follows:

i) Developing in Ilford PQ Universal for 3 min;

ii) Fixing in Ilford Hypam for 3 min;

iii) Washing in tap water for 5 min;

iv) Bleaching in a potassium ferricyanide solution.

With this procedure high diffraction efficiency holograms were obtained.

For reconstruction the holograms were illuminated from the back with red diffuse light produced by a tungsten bulb

and a red gelatine filter. A 35mm camera with a macro lens was used to take photographs focussing onto the hologram plane. A diagram of the reconstruction set-up is shown in Fig.3-3. Enlarged photographs were produced from the 35mm negatives with a typical final magnification of 25:1. A resolution better than 30μm was obtained, which was determined by the width of the fringes.

Neglecting any angular deflection caused by inhomogenieties in the plasma, the phase shift $\Delta\phi$ due to the plasma is given by:

$$\Delta\phi \simeq \frac{2\pi}{\lambda} \int (\mu(x,y,z) - \mu_o)\, d\ell \qquad 3\text{-}1$$

where $\mu(x,y,z)$ and $\mu_o$ are the refractive index of the plasma and background gas and $\lambda$ is the wavelength of the probing beam.

The plasma refractive index is given by

$$\mu - 1 = \sum_j (\mu-1)_j = \sum_j K_j\, n_j \qquad 3\text{-}2$$

where $K_j$ and $n_j$ are the refractivity and density of the different plasma components.

If $\omega >> \omega_{ei}$ , $\omega >> \omega_{eo}$ , $\omega >> \Omega_e$ and $\omega >> \omega_p$, where $\omega$ is the frequency of the probing beam light, $\omega_{ei}$ and $\omega_{eo}$ are the electron-ion and electron-neutral collision frequency and $\Omega_e$ and $\omega_p$ are the electron cyclotron and plasma frequency, the refractive index due to electrons is given by:

$$(\mu - 1)_e \simeq - \frac{1}{2} \frac{\omega_p^2}{\omega^2} \qquad 3\text{-}3$$

Substituting for $\omega$ and $\omega_p$ in Eq.3-3:

$$(\mu - 1)_e \simeq - 4.49.10^{-14} \lambda^2 n_e \qquad 3\text{-}4$$

Assuming that the neutral atoms are in the ground state and if $\omega >> \omega_{ij}$, where $\omega_{ij}$ is the frequency of the atom resonant line, the refractivity due to neutral atoms can be approximated by a one term Cauchy dispersion formula:

$$(\mu - 1)_a \simeq (A + \frac{B}{\lambda^2}) \frac{n}{n_L} \qquad 3\text{-}5$$

where $n$ is the density of neutral atoms and $n_L$ is the Loschmidt's number.

In the visible usually $B/\lambda^2 << A$, so the refractivity of atoms and molecules is not very dependent on wavelength.

The refractive index due to protons is smaller than the refractive index due to electrons by a factor $(m_e/m_p)^2$, so it can be neglected.

Measured values for the constants A and B for atomic hydrogen at STP are (Allen, 1963):

$$A = 1.345.10^{-4}$$

$$B = 1.022.10^{-14}\ cm^2$$

The refractivity of molecular hydrogen can be approximated by the atomic refractivity. At $\lambda$ = 670.9nm the refractive index of molecular hydrogen at 1.00Atm is $n_{H_2} - 1 = 1.385.10^{-4}$ ( Gray, D. E., 1963). At the same wavelength and pressure Eq.3-5 gives $n_H - 1 = 1.368.10^{-4}$ for atomic hydrogen. The difference in refractive index at this wavelength is ~1%.

At the ruby laser wavelength ($\lambda$ = 694.3nm) the electron and neutral refractive indices given by Eqs.2-11 and 2-12 are:

$$(\mu - 1)_e = - 2.16.10^{-22} n_e \qquad 3\text{-}6$$

$$(\mu - 1)_a = 5.085.10^{-24} n_a \qquad 3\text{-}7$$

with $n_e$ and $n_a$ in $cm^{-3}$.

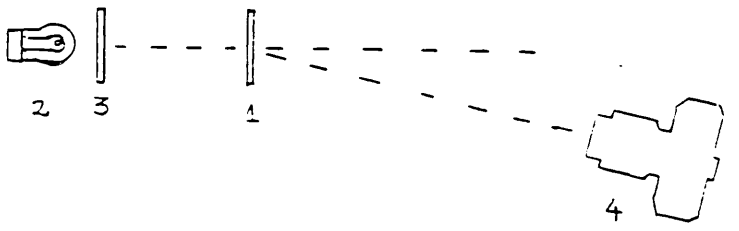


Fig. 3-3 : Hologram reconstruction set-up.
(1) Hologram. (2) Tungsten bulb.
(3) Red gelatin filter.
(4) 35 mm camera with macro lens.

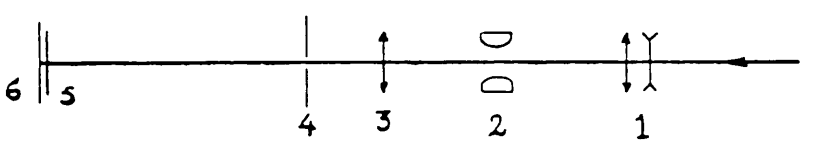


Fig. 3-4 : Schlieren optical set-up.
(1) Beam expander. (2) Pinch assembly.
(3) Lens. (4) Pin-hole. (5) Red filter.
(6) Film.

The fringe shift s associated with a phase change $\Delta\phi$ is given by:

$$S = \frac{\Delta\phi}{2\pi} = \frac{1}{\lambda} \int \left[ (\mu - 1)_e + (\mu - 1)_a - (\mu - 1)_o \right] d\ell \qquad 3\text{-}8$$

Note that the fringe shifts due to electrons and neutrals have opposite signs. The fringe shift due to electrons is ~40 times the fringe shift due to neutrals at the same density and for the same path length.

An Abel inversion of the fringe shift gives the particle density distribution. Details of the procedure involved in the calculation and a discussion of the accuracy of the particle density measurements are presented in Appendix A.

## 3.4. Schlieren Photography

A diagram of the Schlieren set-up is shown in Fig.3-4. The Schlieren technique is based on the angular deviations generated in a probing beam due to refractive index gradients. The angular deflection $\theta$ of the probing beam is given by:

$$\theta \simeq \frac{1}{\mu} \int_{z_1}^{z_2} \nabla (\mu(x,y,z) - 1) \, dx \qquad 3\text{-}9$$

If a constant density gradient $\frac{\partial \mu}{\partial x}$ is assumed, Eq.3-9 can be approximated to give:

$$\theta \simeq \frac{1}{\mu} \frac{\partial \mu}{\partial x} \Delta \ell \qquad 3\text{-}10$$

where $\Delta \ell$ is the characteristic length of the inhomogeneity along the ray path. Using Eqs.3-6 and 3-7 the angular deflections due to electrons $\theta_e$ and neutrals $\theta_n$ are given by:

$$\theta_e \simeq 2.2.10^{-22} \frac{\Delta n_e}{\Delta x} . \Delta \ell \qquad 3\text{-}11$$

$$\theta_n \simeq 5.1.10^{-24} \frac{\Delta n_n}{\Delta x} . \Delta \ell \qquad 3\text{-}12$$

The probing beam is focussed with a lens and a diaphragm is positioned at the focal plane of the lens. The angle $\theta$ subtended by the diaphragm at the lens is given by:

$$\theta = \frac{d}{2f} \qquad 3\text{-}13$$

when d is the diameter of the diaphragm and f the focal length of the lens. An f = 20cm lens and a d = 0.8mm diaphragm were used, giving $\theta$ = 2.0 mrad. Under these

conditions the density gradient resolution for electrons and neutrals was, according to Eqs.3-11 and 3-12:

$$\frac{\Delta n_e}{\Delta x} \simeq 1.8\ 10^{20} cm^{-4}$$

$$\frac{\Delta U_n}{\Delta x} \simeq 7.8\ 10^{21}\ cm^{-4}$$

A characteristic $\Delta \ell = 5.10^{-2}$cm has been assumed. Schlieren images were recorded on Polaroid 410 film with a 7:3 magnification.

## 3.5. Time Resolved Soft X-ray Observations

A scintillator-photomultiplier arrangement was used to investigate the time dependence in the soft X-ray emission by the plasma. Fig.3-5 is a cross-section of the scintillator holder and PM tube attachment. Also shown in the figure is the relative position of the scintillator-PM to the pinch. The scintillator consisted of a 0.5cm radius, 1.0cm long cylinder of NE 102 plastic. A 250nm layer of aluminium was evaporated onto the scintillator surface to block plasma light. The aluminium layer strongly attenuates radiation below 30eV. Aluminium covered NE 102 plastic scintillator has a linear energy response in the 1 to 10keV photon energy range (Meyerott et al, 1964). In Fig.3-6 is shown the

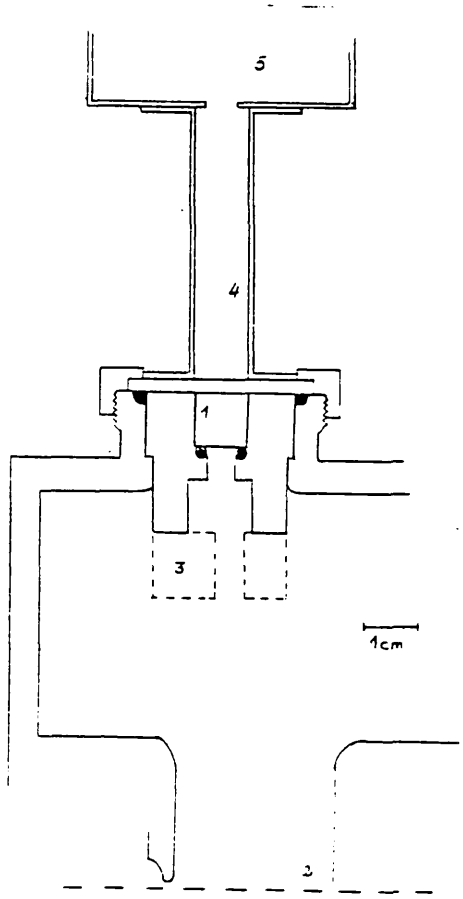


Fig. 3-5 : Cross-section diagram of the scintillator-PM arrangement. (1) Scintillator. (2) Pinch. (3) Collimator. (4) Light pipe. (5) PM case.

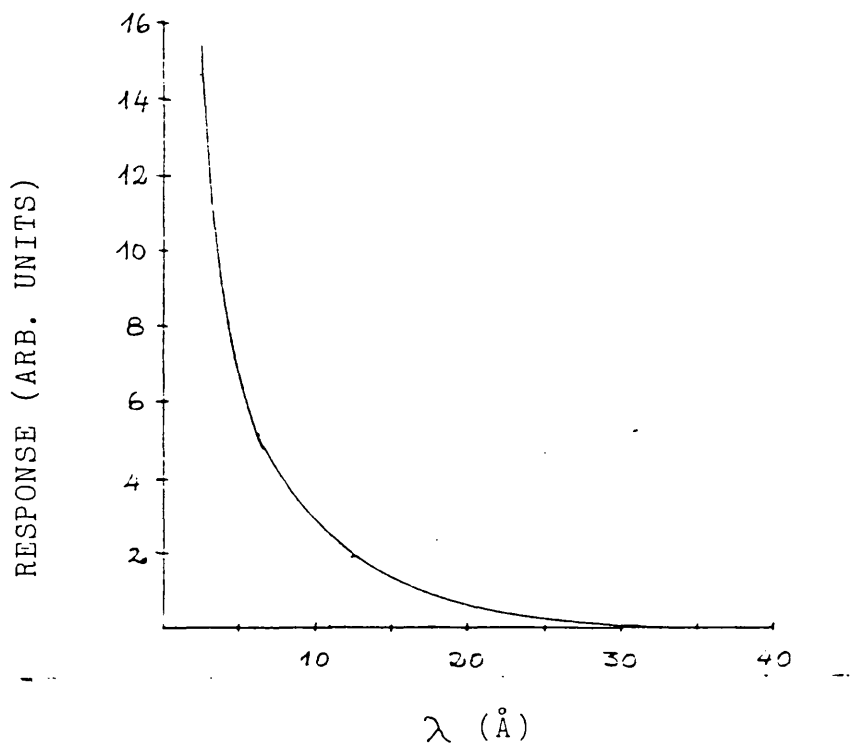


Fig. 3-6 : NE 102 plastic scintillator response.

response of NE 102 for photon wavelengths in the range 5 to 30Å.

A 5cm long, 1 cm radius insulator tube was used as a light pipe to attach the PM window to the pinch chamber. A 7265 RCA PM with an S20 photocathode was used. Typical signal levels of 0.1V were obained with an H.T. of 1.8kV. Noise level was 5mV.

For some recordings a collimator was attached to the front of the scintillator holder in order to exclude radiation emitted from or near the electrodes. It is shown in the dotted line in Fig.3-5.

To determine the time correlation of the soft X-ray emission with the pinch current, the initiating laser pulse was used as a fiducial time marker on the current and PM tube trace.

### 3.6. Soft X-ray Pinhole Photographs

A double pinhole camera with separated X-ray filters was used to record time integrated soft X-ray images of the pinch. In Fig.3-7 is shown a cross-section of the double pinhole camera and its position relative to the pinch. 300μm diameter pinholes were used. The camera is placed about 5cm from the plasma and produces images with

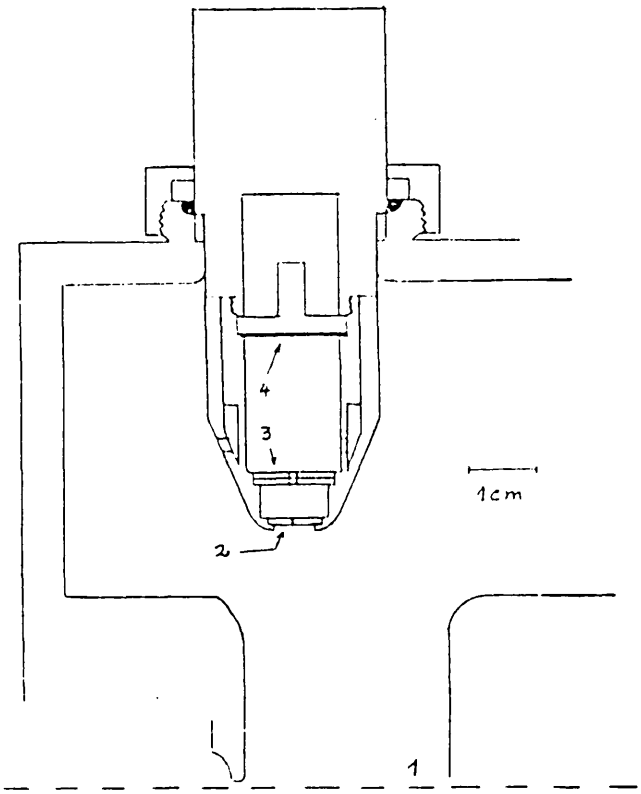


Fig. 3-7 : Cross-section diagram of double pin-hole camera. (1) Pinch. (2) Pin-holes ($\phi$=150 m). (3) Filters. (4) X-ray film.

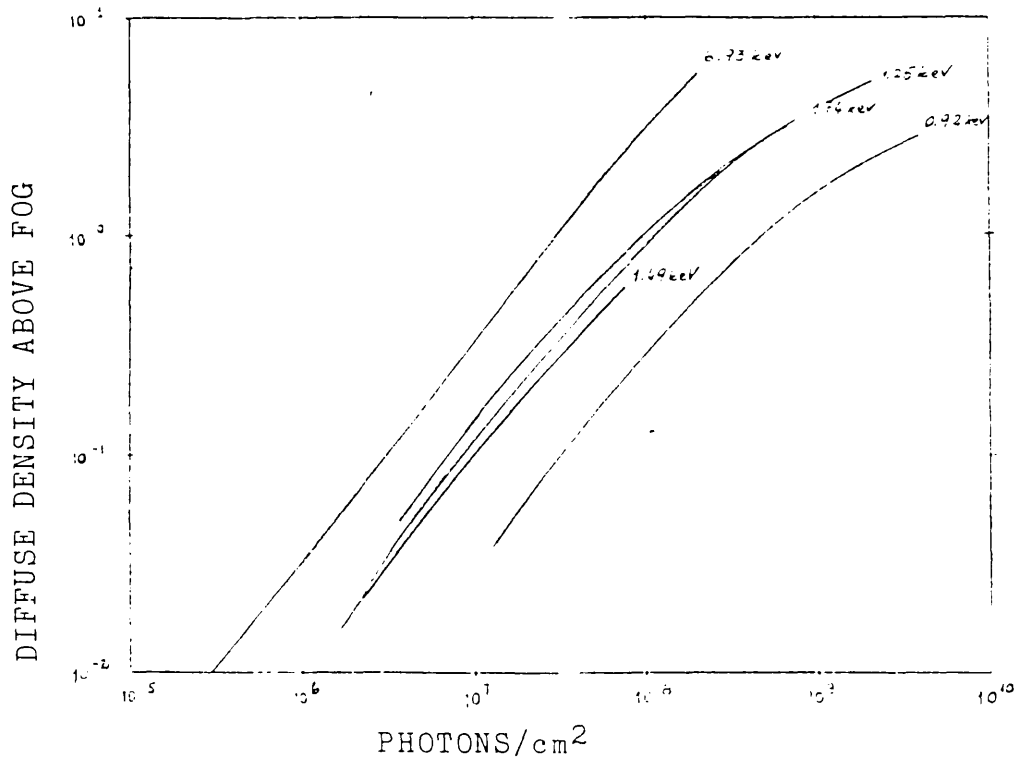


Fig. 3-8 : DEF film callibration. (Rockett, 1984).

approximately 2:1 reduction. Venting is through a light baffle to enable filling with hydrogen at the working pressure. This arrangement allows fragile plastic filters to be used. Diferent thicknesses of aluminium and silver filters produced by evaporation onto a 2.5μm Kim-foil substrate were used. The X-ray film used is the new direct exposure film, DEF, from Kodak. It has a ground fog level lower than Kodak no-screen with a slightly higher sensitivity. A recent calibration of DEF film by Rockett (1984) is shown in Fig.3-8. This callibration is limited to a few wavelengths in the range from 2 to 20Å. Developing of the film is as for Kodak no-screen.

## 3.7. The Two-Filter Ratio Technique

The radiation emitted by a pure hydrogen plasma was found insufficient to expose the X-ray film on a single shot basis. A mixture of hydrogen with 4% air was used as filling gas in order to enhance plasma radiation.

The two-filter ratio technique has been used to obtain a measurement of the electron temperature from the double pinhole photographs described in Section 3.6. This measurement is time integrated over the duration of the pinch.

The observed ratio of X-ray film exposure is compared with the calculated ratio of exposure for the same filter arrangement, which depends on the temperature of the emitting plasma.

The film exposure, in terms of diffuse film density above background fog, is a function of the total number of photons emitted by the plasma, which have fallen onto the film. It is given by:

$$E(T_e,n_e,t)=E_o \int_o^t \cdot \int_o^{\lambda_{max}} I(\lambda,T_e,n_e).A(\lambda,s).D(\lambda)d\lambda dt' \qquad 3\text{-}14$$

where:

$I(\lambda,T_e,n_e)$ is the number of photons per unit volume, per unit wavelength, per unit time, per unit solid angle emitted by the plasma.

$A(\lambda,s)$ is the filter transmission coefficient for a filter of thickness s,

$D(\lambda)$ is the film sensitivity,

the exposure time,

$E_o$ a geometric factor, and

$\lambda_{max}$ is a wave cut-off defined by the filter transmission characteristics.

In a hydrogen plasma with impurities the photon emission due to radiation continuum is given by:

$$I(\lambda,T_e,n_e) = I_{f-f}(\lambda,T_e,n_e) + I_{f-b}(\lambda,T_e,n_e) \qquad 3\text{-}15$$

where $I_{f-f}(\lambda,T_e,n_e)$ is bremsstrahlung radiation due to free-free transitions of the electrons in the field of the ions and $I_{f-b}(\lambda,T_e,n_e)$ is due to recombination of electrons with ions.

If the electrons have a Maxwellian distribution, $I_{f-f}(\lambda,T_e,n_e)$ is given by:

$$|I_{f-f}(\lambda,T_e,n_e)| = \frac{1.5.10^{-14}}{\lambda\ T_e^{\frac{1}{2}}}\ n_e\left[\sum_{\alpha}\sum_{z} z^2\ n_z^{\alpha}\right]\ \bar{g}_{ff}$$

$$\cdot\exp\left(-1.24.10^{-4}/\lambda T_c\right)\ \text{photons.cm}^{-4}.\text{s}^{-1}.\text{sr}^{-1} \qquad 3\text{-}16$$

where $T_e$ is in eV, $\lambda$ in cm, $n_e$ and $n_z^{\alpha}$ are the density of electrons and ions of atomic species $\alpha$ and charge z in $cm^{-3}$ and $\bar{g}_{ff}$ is a mean Gaunt factor.

The quantity in brackets can be written in terms of the effective charge $z_{eff}$, which is given by:

$$Z_{eff} = \sum_{\alpha} \sum_{z} \frac{n_z^a \, z^2}{n_e} \qquad 3\text{-}17$$

Eq.3-16 then can be written as:

$$|I_{f-f}(\lambda, T_e, n_e)| = \frac{1.5.10^{-14}}{\lambda \cdot T_e^{\frac{1}{2}}} n_e^2 Z_{eff} \bar{g}_{ff} \exp(-1.24.10^{-4}/\lambda T_e)$$

$$\text{photons.cm}^{-4}.\text{s}^{-1}.\text{sr}^{-1} \qquad 3\text{-}18$$

If the electrons have a Maxwellian distribution and recombination takes place into the ground state of the ion, $I_{f-b}(\lambda, T_e, n_e)$ is given by:

$$|I_{f-b}(\lambda, T_e, n_e)| = \frac{1.5.10^{-14}}{\lambda \cdot T_e^{3/2}} n_e \sum_{\alpha} \sum_{z} \xi \, \chi_{z-1}^{\alpha} \, n_z^{\alpha} \frac{Z^2}{n_o^{\alpha 3}} \bar{g}_{fb}$$

$$\cdot \exp\left[ (- 1.24.10^{-4}/\lambda + \chi_{z-1}^{\alpha})/T_e \right]$$

$$\text{photons.cm}^{-4}.\text{s}^{-1}.\text{sr}^{-1} \qquad 3\text{-}19$$

where $\xi$ is the number of places which can be occupied by the electron in the ground state, $\chi_{z-1}^{\alpha}$ is the ionization energy of ions of atomic species $\alpha$ and charge (z-1) in eV, $\bar{g}_{fb}$ is a mean Gaunt factor and $n_o^{\alpha}$ is the principal quantum number of the ground state of the ion.

Eqs.3-18 and 3-19 require the density of ions of the different atomic species. To estimate the ion population it is necessary to assume a model of plasma conditions.

### 3.7.1. The ionization model

A time dependent corona model (Post, 1961) is used to calculate the different ion populations. It assumes that the electrons recombine into the ground state of the ions. The effect of recombination on the ion population is neglected. The continuum includes bremsstrahlung with a $z_{eff}$ due to hydrogen and nitrogen ions and recombination into H, $H_e$ and Li-like nitrogen ions. Oxygen and other impurities are neglected. A discussion of the model is presented in Section 3.7.2.

The rate equation for ions of charge z is:

$$\frac{dn_z}{dt} = n_{z-1}\,\nu_{z-1} - n_z\,\nu_z \qquad 3\text{-}20$$

where $\nu_z$ is the ionization frequency, which is given by:

$$\nu_z = n_e\,S_z\,(T_e) \qquad 3\text{-}21$$

where $S_z\,(T_e)$ is the ionization coefficient.

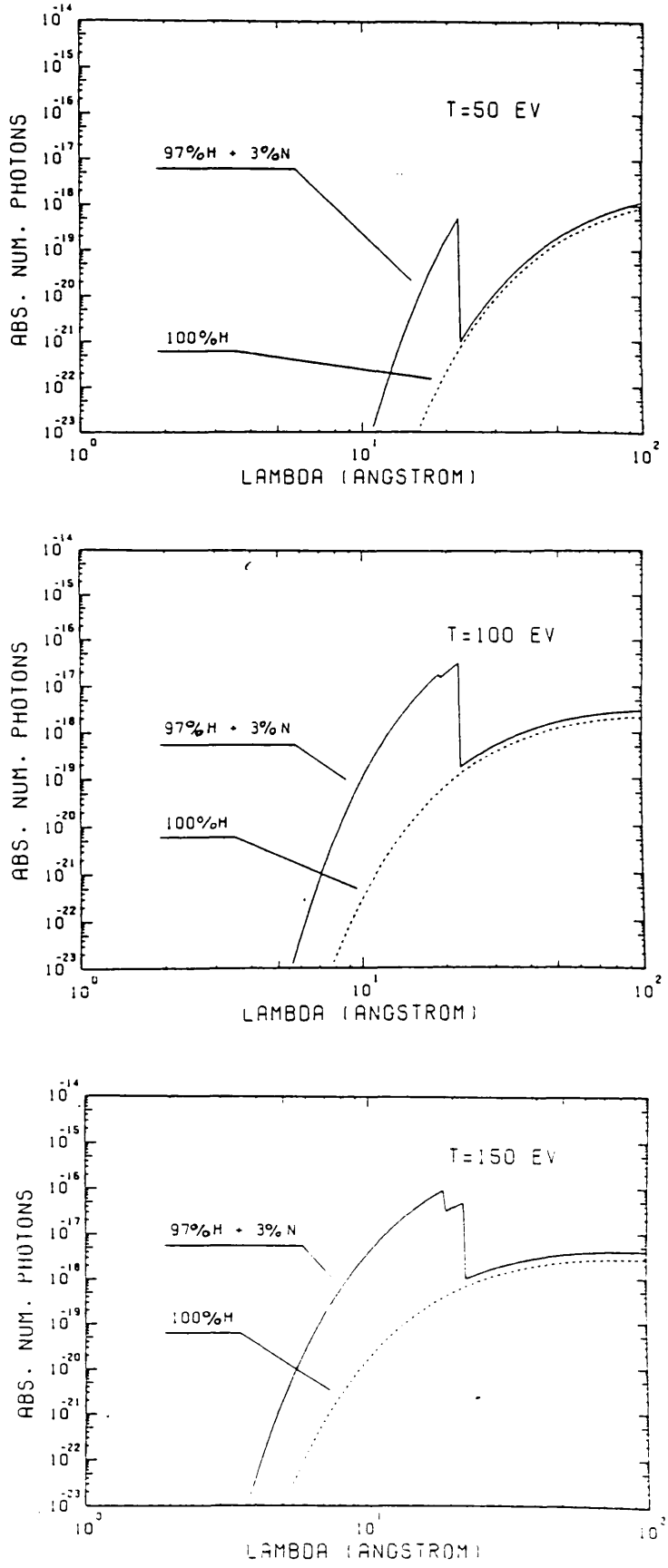


Fig. 3-9: Continuum emission from 97% H + 3% N plasma. The dotted line corresponds to bremsstrahlung emission from a pure hydrogen plasma. The recombination edges can be observed.

A formula proposed by Kolb and McWhirter (1964) which is obtained by integration of the excitation cross-section due to Seaton (1962) over a Maxwellian distribution is used for $S_z(T_e)$:

$$S_z(T_e) = \frac{1.64.10^{-6}}{\chi_z \, T_e^{\frac{1}{2}}} \exp(-\chi_z/T_e) \ cm^{-3}.s^{-1} \qquad 3\text{-}22$$

Eq.3-20 defines a set of equations which can be solved if initial conditions are specified.

A constant hydrogen filling density with 3% nitrogen is assumed. Hydrogen atoms are assumed to be fully ionized. The electron density is specified at t=0. The electron temperature is taken to be constant and the ion population is calculated as a function of time.

In Fig.3-9 is shown the continuum emission calculated for a hydrogen plasma with 3% nitrogen. Initial electron density is $3.10^{18} cm^{-3}$. The emission profiles for 50, 100 and 150eV are shown. The impurity thermalization time is 40ns. The H and He-like nitrogen recombination edges at 16 Å and 22.45Å are shown in the figures. The Li-like nitrogen recombination edge at 126.68Å is not shown.

### 3.7.2. Discussion of the ionization model

A calculation using the condition for L.T.E. by Griem (1964) indicates that at a temperature of 50eV, electron densities of $10^{20}cm^{-3}$ and higher are required for the ground and first excited level of Li to H-like nitrogen to be in L.T.E.

A calculation by House (1964) indicates that collisional-radiative equilibrium between He and H-like nitrogen ions in the ground state at Te=50eV requires $ne \simeq 10^{23}cm^{-3}$.

Steady state coronal equilibrium for H-like nitrogen at 50eV requires $n_e \leq 5.5.10^{+16}cm^{-3}$ (McWhirter, 1965).

The plasma in the experiment has a characteristic density of the order of $10^{18}cm^{-3}$, so ionization equilibrium does not apply and a time dependent model is required.

In a transient ionization process recombination becomes important when steady state is approached. The time $\tau$ to reach steady state in any corona model plasma is given, to an order of magnitude (McWhirter, 1965) by:

$$\tau \simeq \frac{10^{12}}{n_e} \text{ s} \qquad 3\text{-}23$$

Using a characteristic density of $3.10^{18}cm^{-3}$, $\tau$ is estimated to be ~30ns, which is of the same order as the duration of the equilibrium phase of the pinch.

It is therefore possible to neglect recombination to a first approximation and a simple model with collisional ionization can be adopted.

Ionization coefficients for Li-like nitrogen were found to calculated with Eq.3-22 agree within a factor of three with measurements at 70eV by Brown et al (1983) and within a factor of two with measurements at 110eV by Greves et al (1981).

The ionization model has been used to calculate the population of nitrogen and oxygen ions as a function of time. The calculation indicates that for $2.10^{18}cm^{-3} \leq n_e \leq 5.10^{18}cm^{-3}$, $30eV \leq T_e \leq 100eV$ and $10ns \leq t \leq 40ns$, He-like nitrogen and oxygen ions account for more than 90% of the ion population of each species. Using the calculated ion populations, the power radiated by recombination with nitrogen ions is estimated to be ~ four times higher than that for oxygen ions.

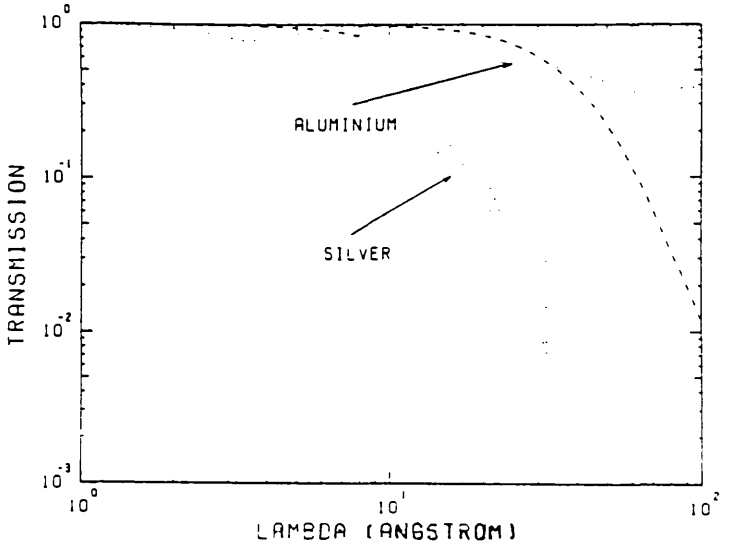


Fig. 3-10:Transmission curve for aluminium and silver.

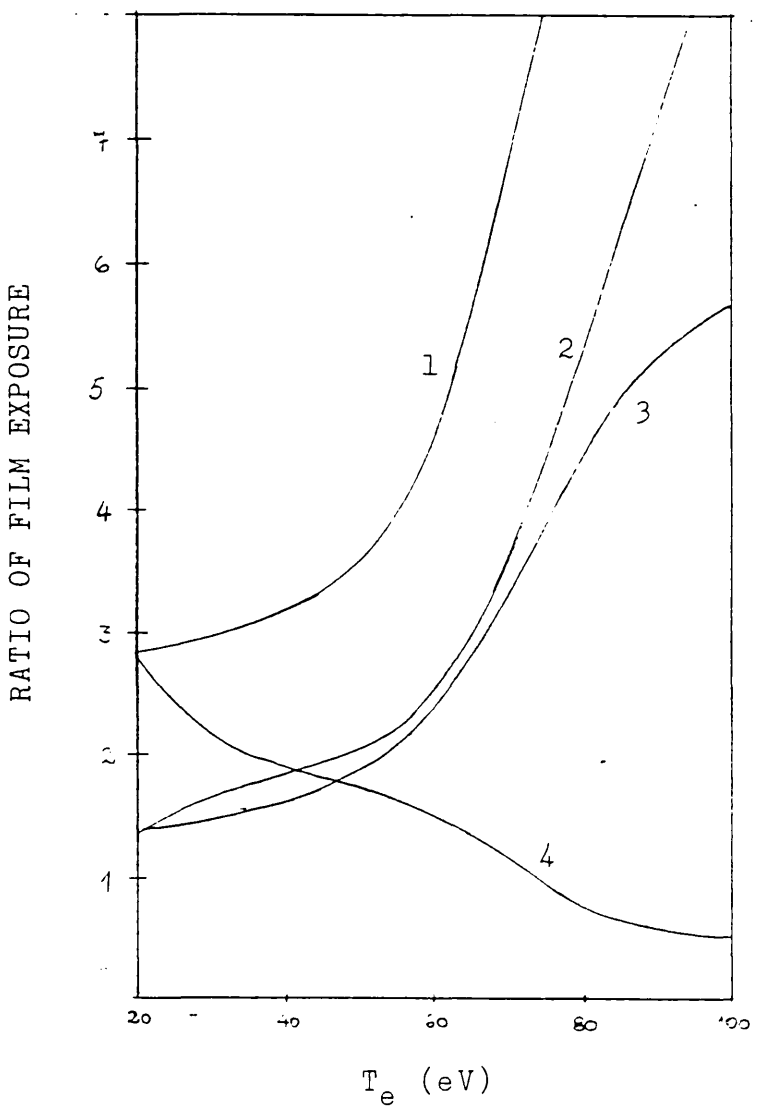


Fig 3-11:Calculated ratio of film exposure. Filter combinations: (1) F-4/F-1. (2) F-5/F-2. (3) F-3/F-4. (4) F-3/F-5. (Filters number as in Table 3-1)

### 3.7.3. X-ray filters

The characteristics required for the X-ray filter combinations are:

i) Different transmission bands in the wavelength range of interest;

ii) Opacity to ultraviolet and visible radiation;

iii) Low transmission of radiation with $\lambda > 100Å$, to avoid line emission from low Z impurity ions.

Aluminium and silver appear as suitable complementary filter materials. Both can be prepared to sub-micron thickness by vacuum deposition and have excellent visible and U.V. blocking properties. In Fig.3-10 is shown the transmission curve for Aℓ and Ag filters. Their transmission bands are conveniently located either side of the He-like recombination edge at $\lambda = 22.46Å$, with silver being more transparent in the long wavelength region. This combination of filters is expected to achieve good sensitivity at temperatures below 100eV.

The different filters used in the experiment are summarized in Table 3-1.

Mass absorption coefficients given by Henke and Ebisu (1973) have been used in the calculation of the filter transmission.

In Fig.3-11 is shown the calculated exposure ratio for some filter combinations. The curves indicate a good sensitivity in the range 20-100eV.

### 3.7.4. The film response

A wide spectrum calibration of DEF film is still not available. In Fig.3-12 is shown a sensitivity curve for Kodak no-screen film. It is due to a film model by Brown et al (1976) plus a calibration for long wavelengths by Koppel (1975). The available DEF data is included

The DEF calibration is not very different from that of no-screen, so the no-screen calibration has been used. In the computation of film exposure the callibration curve was approximated by the dotted line shown in Fig.3-12.

### 3.7.5. The accuracy of the temperature measurements

The three main sources of error in the te perature measurements are: i) the ionization model; ii) line radiation, and; iii) film calibration.

The ionization model assumes a constant temperature of the plasma, whereas in the real situation the temperature is expected to be increasing in time, with an initial low value. The model assumes neutral nitrogen atoms at t=0,

which regarding the effect of preheat and the low ionization potential for NI(14.53eV) and NII(29.6eV) is not true.

The net effect of these two approximations in the accuracy of the ionization populations is not known, but the assumption on the temperature could lead to an over estimation of the population of high ionization stages, which contribute to the recombination continuum. Neglecting the effect of recombination on the ionization rates could have a similar result.

Calculations based on this model indicate that for temperatures below 100eV the dominant ionization stage is He-like nitrogen, which is consistent with the fact that the ionization potential for He-like nitrogen is 552eV.

Addition of air in the filling hydrogen introduces the possibility of line radiation below 100Å arising from high Z oxygen and nitrogen ions. For $n_e \geq 10^{18} cm^{-3}$ line radiation from He-like ions is due mainly to the $1s^2 {}^1S_o - 1s2_p {}^1P_1$ resonance line (De Michelis and Mattioli, 1981) with a minor contribution from the $1s^2 1s_o - 1s2_p {}^3P$ intercombination line. Absolute estimations of line emission depend on the collisional population rates and transition probabilities of the corresponding levels and the accuracy relies on the model used in the calculations. It is fortunate that the nitrogen resonance and intercombination lines coincide with

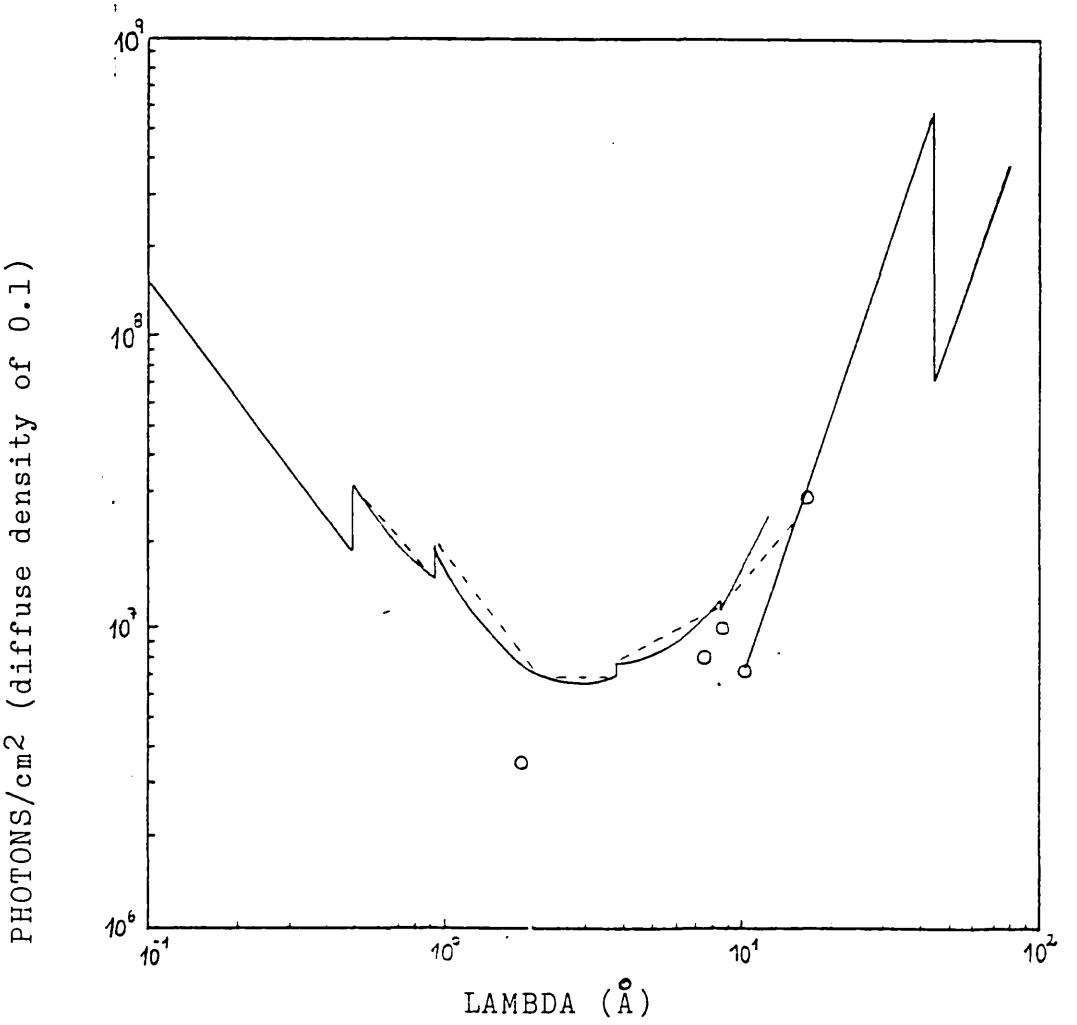


Fig. 3-12: Film callibration. Full line: Kodak no-screen. Dotted line: linear approximation. Circles correspond to Kodak DEF.

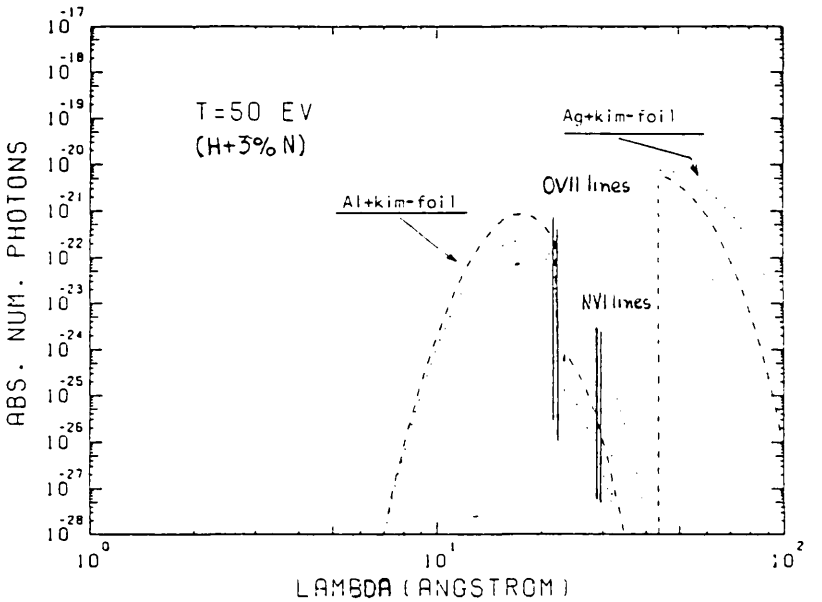


Fig. 3-13: Transmitted continuum for Al and Ag filters. The location of oxigen and nitrogen lines is indicated.

a low transmission band in the filters. In Fig.3-13 is shown the transmitted recombination and bremsstrahlung spectrum of a 50eV hydrogen plasma with 3% nitrogen. Filters are Aℓ and Ag on a Kim-foil substrate. The figure shows a drop in the transmitted intensity of at least one order of magnitude with respect to the neighbouring continuum at the wavelength of the nitrogen lines. Oxygen lines are at 21.6 and 21.8Å, close to the nitrogen recombination edge at 22.46Å, where filter transmission is high. The oxygen line emission at 50eV can be roughly estimated to be around two orders of magnitude lower than for nitrogen. This is due to the higher excitation energy of oxygen lines and the lower atomic concentration.

For temperatures below 100eV, the continuum emission at $\lambda \leq 5$Å is not important. In the relevant wavelength range DEF and no-screen callibrations are very similar and errors introduced by the callibration are reduced on considering the ratio of exposures.

It follows from this discussion that a temperature measurement using the filter-ratio technique and based on the enhancement of the radiation continuum due to recombination into impurity ions has to be seen as a crude approximation. A more sophisticated ionization model and an estimation of the relative intensity of line emission to the

continuum are required to improve the accuracy of the method.

It is important to note that because the technique relies on ratios of exposure it is less sensitive to errors in the calculted emission that an absolute measurement.

Table 3-1

X-ray Filters.

| Filter No | Material and thickness ($mg.cm^{-2}$) |
|---|---|
| 1 | Ag (0.34) + Kim-foil (0.528) |
| 2 | Ag (0.436) + Kim-foil (0.528) |
| 3 | Ag (0.218) + Kim-foil (0.528) |
| 4 | Aℓ (0.22) + Kim-foil (0.516) |
| 5 | Aℓ (0.22) + Kim-foil (0.78) |

# CHAPTER IV

## Experimental Observations

### 4.1. Introduction

The experimental observations resulting from the different diagnostics described in Chapter III are presented in this chapter.

Three well defined phases were observed in the evolution of the pinch: i) preheat phase, ii) equilibrium phase, and iii) unstable phase.

Time resolved measurements of the particle density distribution have been obtained for the first two phases.

The initial stages in the developing of the instability have been observed and growth rates have been measured.

A time integrated measurement of the electron temperature has been made, which is complemented by time resolved observations of the soft X-ray emission.

### 4.2. Characteristics of the Pinch Evolution

Fig. 4-1 shows streak photographs taken transversely to the pinch with and without a preheating discharge.

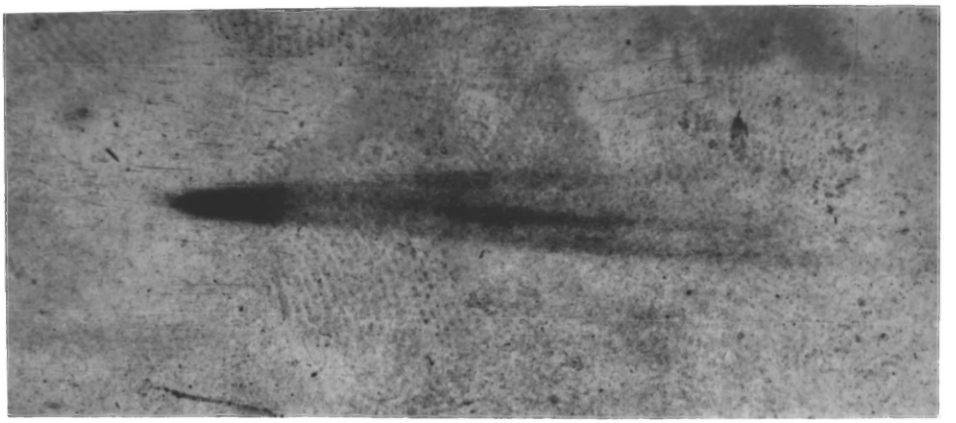

(a)

(b)

Fig. 4-1-a: Streak photographs of non-preheated discharges. Streak speed: 100 $ns.cm^{-1}$. (a) 0.33 Atm. (b) 1.00 Atm.

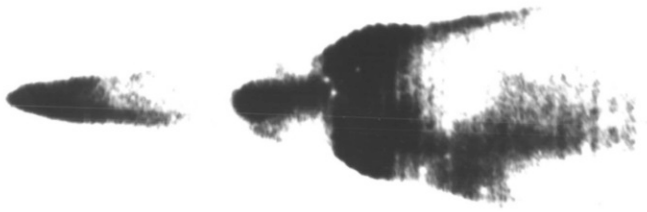

(a)

(b)

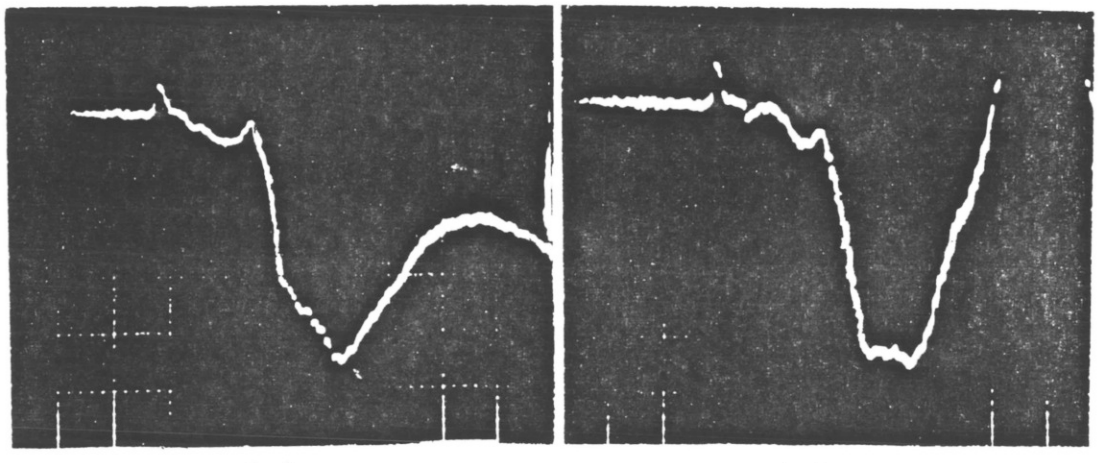

(a) (b)

Fig. 4-1-b: Streak photographs and current waveforms for preheated discharges. (a) 0.33 Atm. (b) 1.00 Atm.
Current traces: 8.8 kA/div, 50 ns/div. Streak speed: 100 $ns.cm^{-1}$.

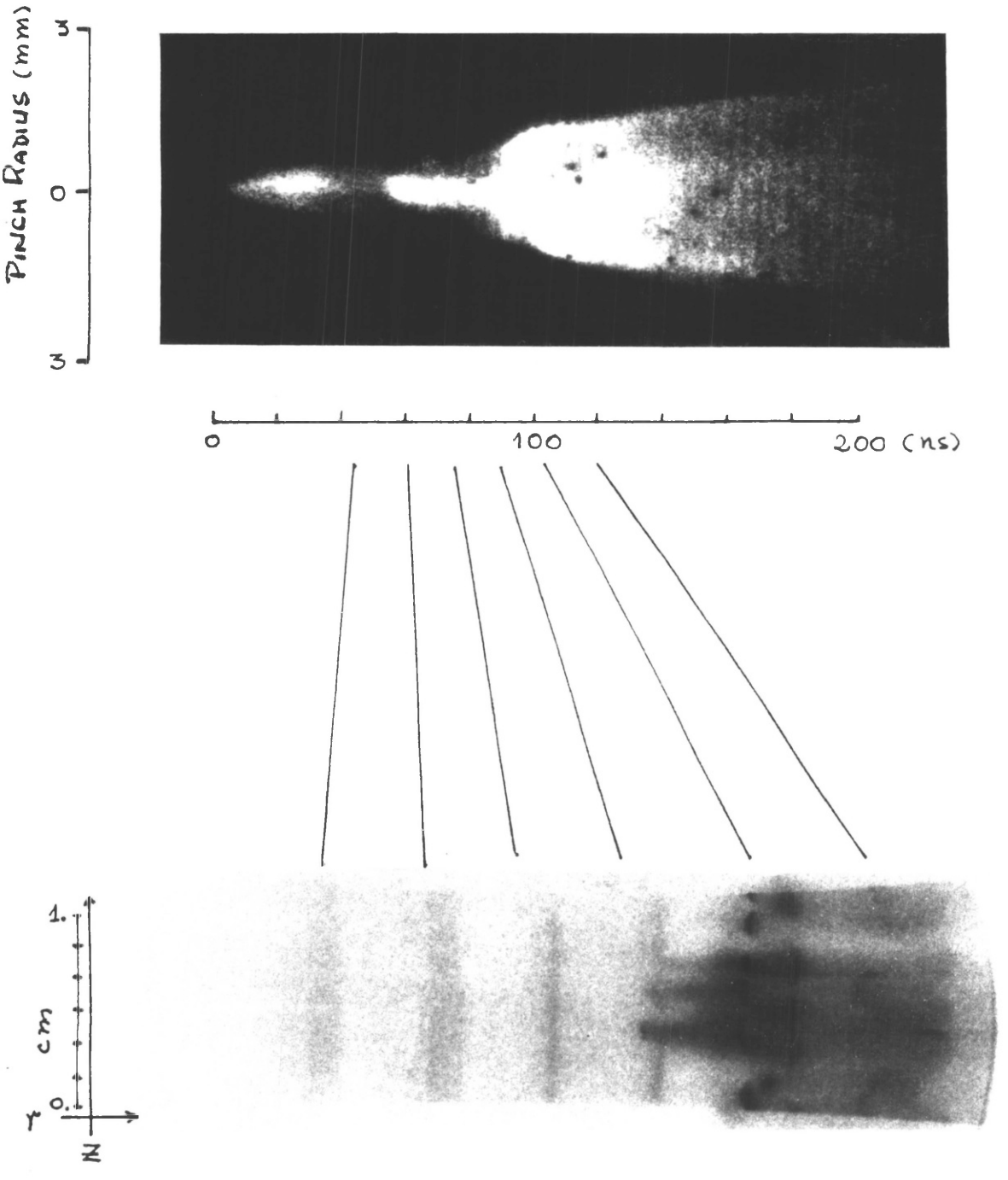


Fig. 4-2: Streak and framing photograph showing different phases in the pinch evolution. Streak speed: Streak speed: 100 ns.cm$^{-1}$. Framing rate: 7.5.10$^{7}$ s$^{-1}$. Pressure : 0.33 Atm.

Without preheat the pinch is seen to expand continuously. The same behaviour is observed over the 0.2-2.0 Atm. pressure range investigated.

With preheat, the pinch evolution is as follows:

i) It expands continuously during the preheating discharge;

ii) A constant radius phase begins at the time when the main current starts. The duration of this phase depends on the filling gas pressure;

iii) A fast expansion follows, which corresponds to the transformation of the pinch into an expanding helical structure.

These three phases can be observed in Fig.4-2. The figure shows a streak photograph and a time correlated sequence of framing photographs. First two frames correspond to the preheating discharge. The third one shows a uniform column which is narrower than during preheat. Following frames show the transition to a helical structure.

Most of the observations correspond to 0.33 and 1.00 Atm Typical duration of the preheating current is 60-80ns with a maximum current of 5-6kA. Mean rate of rise of the main

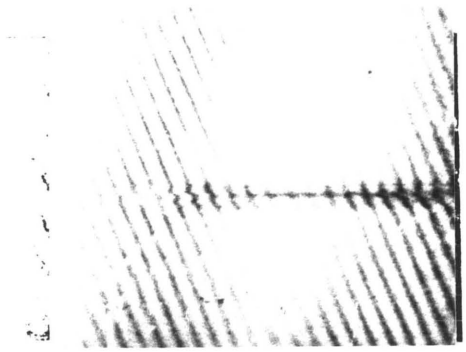

(a)

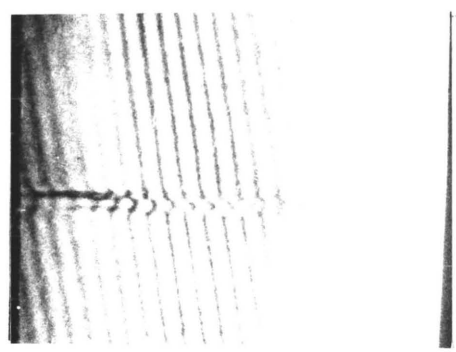

(b)

1mm.

Fig. 4-3: Interferograms at early times during the preheating discharge. t=14 ns. (a) 0.33 Atm. (b) 1.00 Atm.

current is $\sim 8.10^{11} A.s^{-1}$ at both pressures with a peak current of about 40kA. There is evidence to indicate that the decay in current observed after peak for the 0.33 Atm case is due to crowbarring.

The current traces show no conclusive evidence of any change in inductance associated with the transition of the pinch to a helical structure.

The next sections of this chapter present the experimental observations which characterize each of the pinch phases.

## 4.3. Preheat Phase

### 4.3.1. Initiation

There are two possibilities for the focussing of the initiating laser beam: i) on the electrode, ii) between the electrodes. The first possibility is generally better because it avoids a non-uniformity in the plasma column caused by the laser breakdown spot.

A 20cm focal length lens was used to focus the laser beam onto the cathode. Power density at the focal spot is estimated at $\sim 6.10^{11} W.cm^{-2}$. A plasma is generated by laser breakdown at the cathode surface.

Best operational conditions were found at a gas pressure of 0.33 Atm. A well defined uniform discharge column resulted with a reproducibility better than 90%. At 1.00 Atm the dischage channel was less reproducible and some axial non-uniformity was observed.

Fig. 4-3 shows interferograms corresponding to early stages in the developing of the preheating discharge. 14ns after intiation by the laser pulse a discharge channel typically 300-400μm diameter is already formed. The fringe shift indicates that the axial uniformity observed later is not present at early times.

4.3.2. Channel expansion

The discharge channel is observed to expand radially during the duration of the preheating discharge. Two independent measurements of the expansion velocity were obtained:

i) From streak photographs and for $t \leq 40ns$,

$v_r = 1.7.10^4 \pm 0.5.10^4 m.s^{-1}$.

ii) From interferograms and for $t \geq 30ns$,

$v_r = 8.7.10^3 \pm 1.7.10^3 m.s.^{-1}$

The expansion velocity was observed to be independent of the gas pressure for 0.33 and 1.00 Atm.

The streak photograph observations correspond to discharge initiated by a 30ns FWHM ruby laser pulse. This is longer than the 5ns FWHM laser pulse used for pinch initiation when the interferometric observations were performed. The long laser pulse could have some effect on the expansion at early time.

### 4.3.3. Particle density distributions

Fig.4-4 shows a typical interferogram of the preheating discharge at 0.33Atm. The fringe shift at the edge of the discharge column indicates a density of neutral particles which is higher than in the background gas. Fig.4-5 shows the corresponding particle density profile obtained by Abel inversion of the fringe shift. The inversion assumes that the electron and neutral particle distribution do not overlap. A flat electron density profile is observed with a layer of high density neutrals at the edge of the column.

Fig.4-6 shows a schlieren photograph of the preheating discharge. Single dark fringes are observed at each side of the pinch. To correlate the schlieren photograph with the interferometric observations the particle density profile

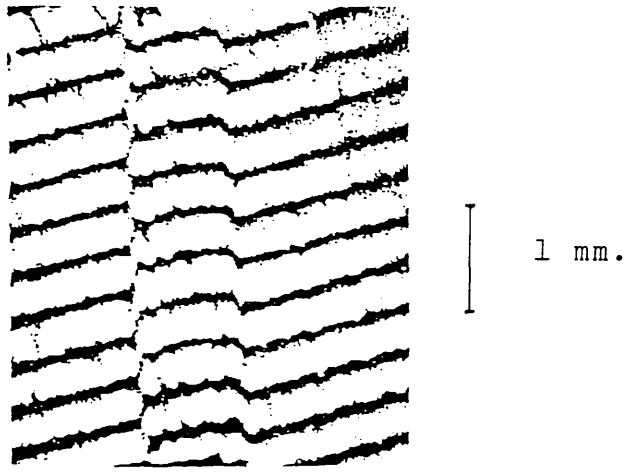


Fig. 4-4: Interferogram of the preheating discharge. t=52 ns. Pressure: 0.33 Atm.

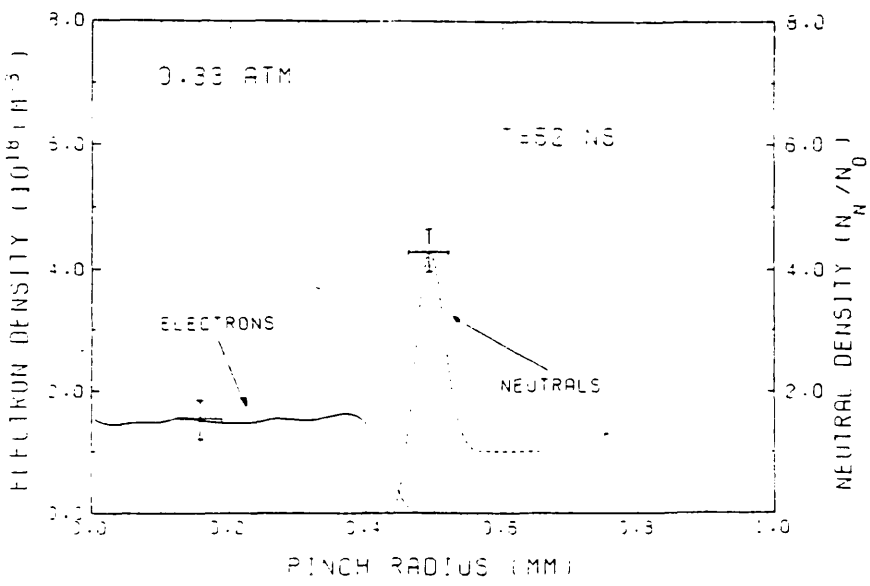


Fig. 4-5: Particle density profile corresponding to the interferogram shown in Fig. 4-4.

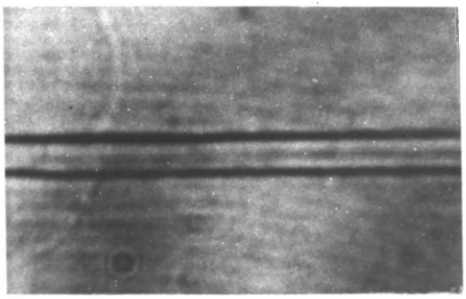

Fig. 4-6: Schlieren photograph of the preheat. t=48 ns.

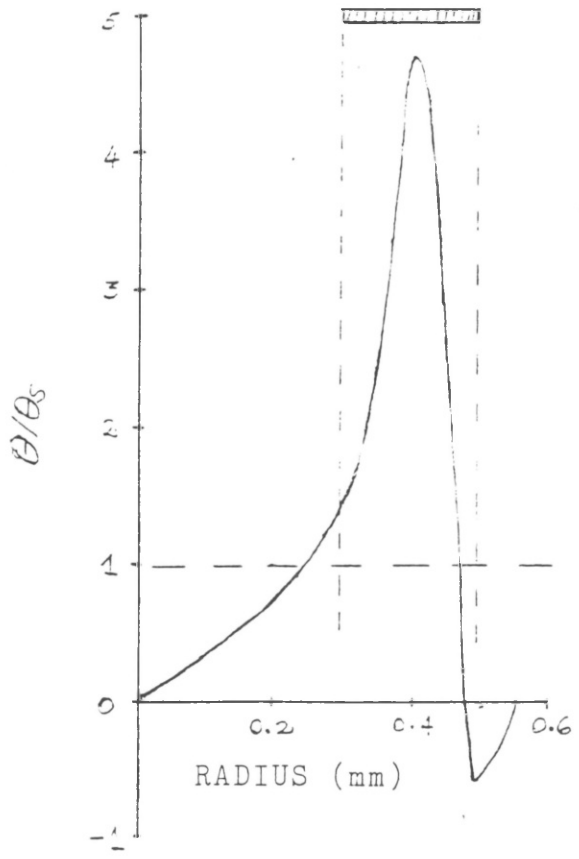


Fig. 4-7: Calculated schlieren deflection corresponding to the particle density profile shown in Fig. 4-5. The bar represents the dark fringe in the schlieren photograph shown in Fig. 4-6.

shown in Fig.4-5 was used to calculate the expected deflection angle as a function of the pinch radius. The result is shown in Fig.4-7. The deflection angle $\theta$ is normalized to the schlieren angle $\theta_s$ defined by the optical set-up. A dark fringe is obtained if $|\theta/\theta_s| \geq 1$. The calculated deflection shows very good agreement with the schlieren photograph indicated by the thick line on top of the figure. Positive deflection is due to the combined effect of the electron density gradient and the neutral density gradient on the inner side of the high density neutral layer. Negative deflection due to the falling density on the outer side of the high density neutral layer is less than the schlieren angle.

Fig. 4-8 shows the evolution of the electron density profile during preheat for 0.33 and 1.00 Atm. The electron distribution changes from a hollow to a flat profile with typical electron densities around $10^{18}cm^{-3}$.

The electron line density Ne can be calculated by integrating the electron density profile over the pinch section. Fig. 4-9 shows the evolution of the electron line density. Within the acuracy of the measurements it is observed to remain nearly constant.

The time development of the high density neutral layer at the pinch boundary is shown in Fig. 4-10.

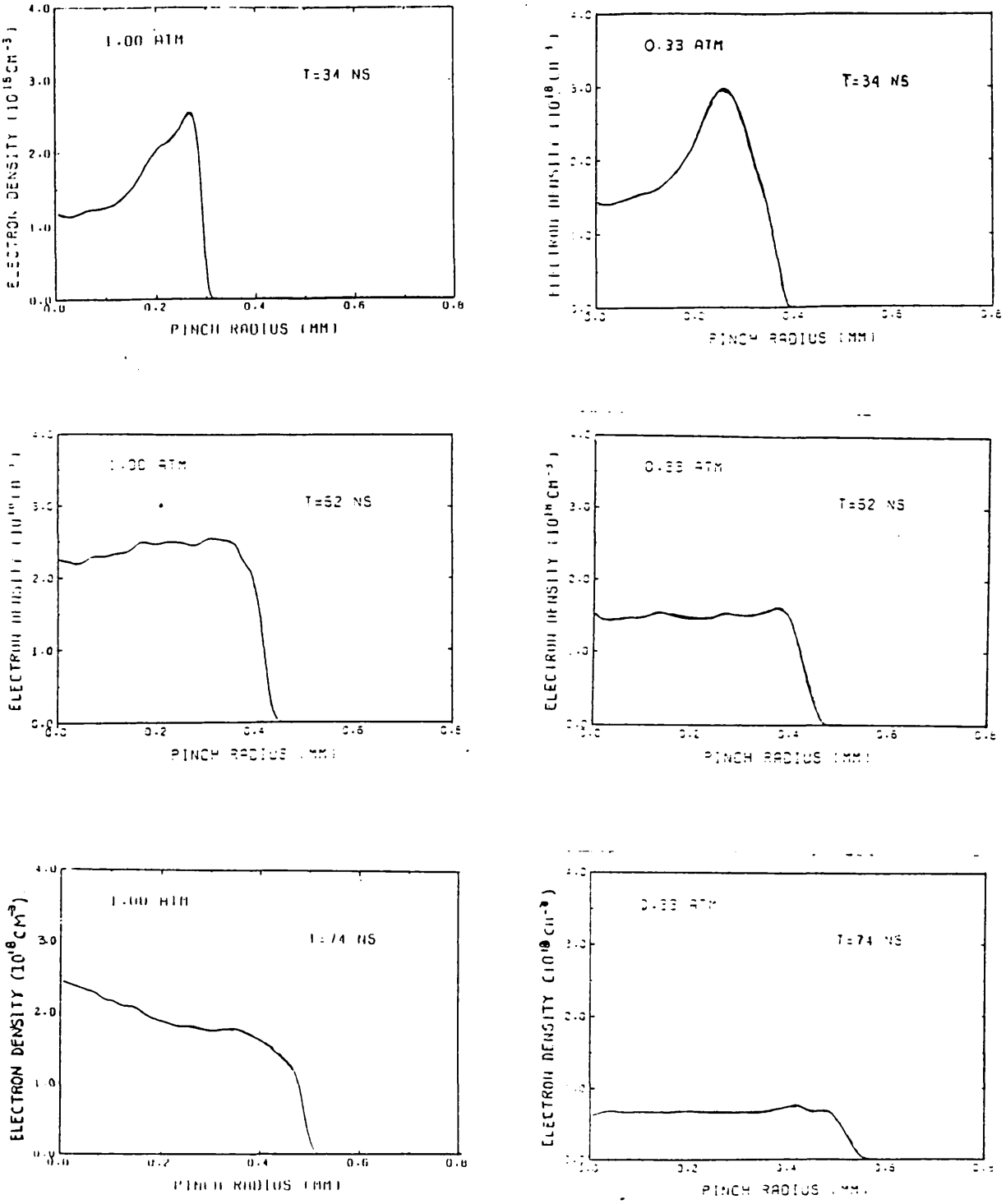


Fig. 4-8: Time history of the elctron density profile during preheat. (a) 1.00 Atm. (b) 0.33 Atm.

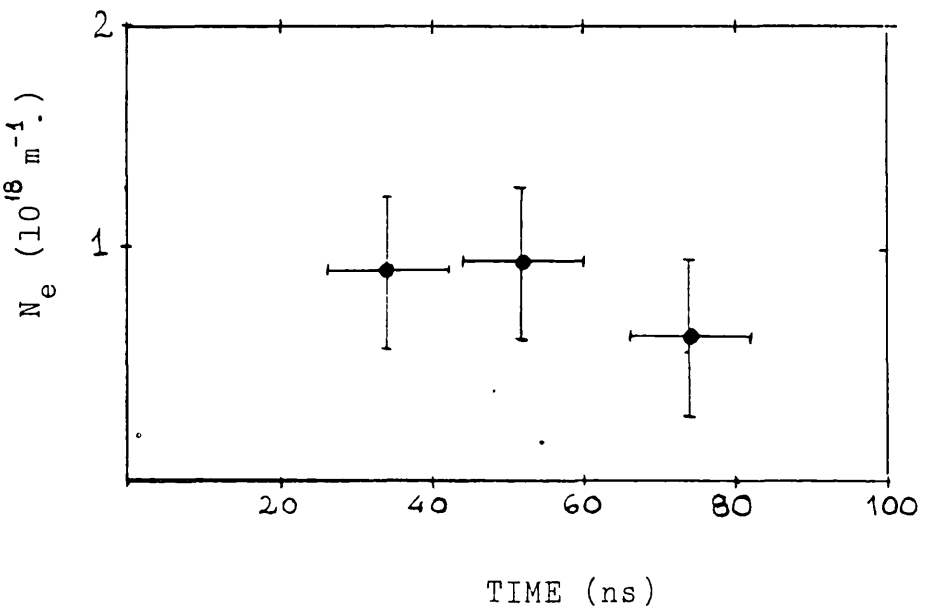


Fig. 4-9: The electron line density during preheat.
Pressure: 0.33 Atm.

For particle conservation in the discharge column the ratio $(N_e + 2N_N)/2N_o$ must be constant. $N_N$ is the neutral line density in the high density neutral layer and $N_o$ is the molecular density of neutral molecular hydrogen at background pressure, filling a column of the same radius as the discharge channel. If the number of particles is conserved, $(N_e + 2N_N)/2N_o = 1$. Fig.4-11 shows $(Ne + 2N_N)/2N_o$ during preheat for 0.33 Atm. The figure indicates that a fraction of the neutrals in the high density neutral layer corresponds to hydrogen atoms resulting from molecular dissociation.

The dynamics of the preheating channel expansion and characteristic parameters of the high density neutral layer are discussed in Chapter 5.

## 4.4. Equilibrium Phase

### 4.4.1. Duration of the equilibrium

Table 4-1 shows the duration of the equilibrium phase, as determined from streak photographs, for the pressure range 0.2 - 1.7 Atm.

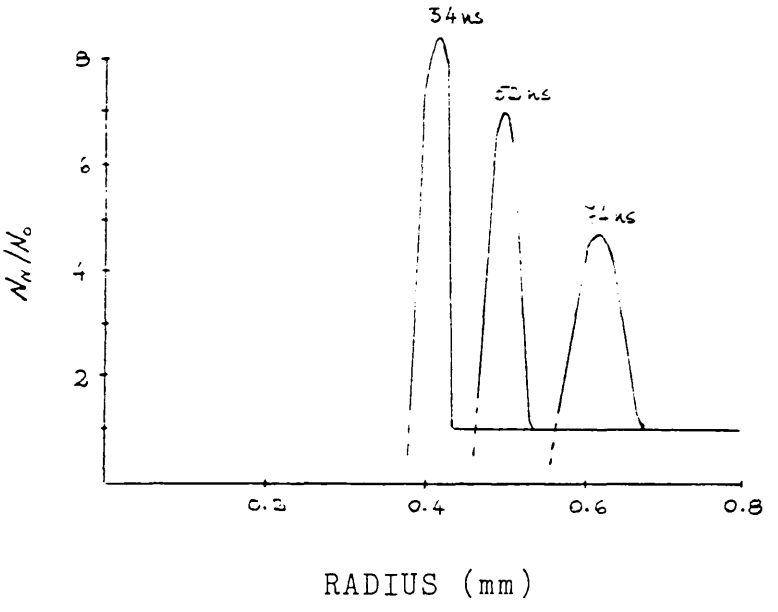


Fig. 4-10: The high density neutral layer during preheat. Pressure: 0.33 Atm.

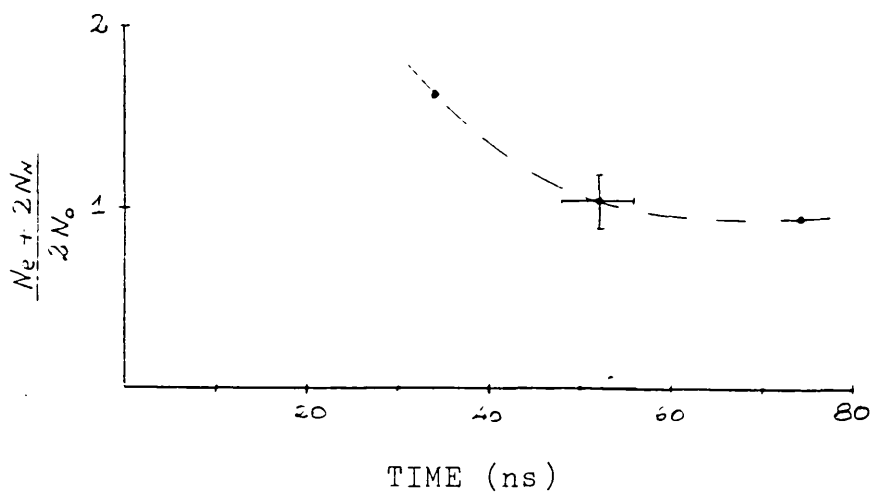


Fig. 4-11: Particle conservation during preheat. A high dissociation fraction is observed at early time. Pressure: 0.33 Atm.

Table 4-1

Stability times

| Shot | pressure (Atm) | $\tau$(ns) | a($\mu$m) |
|---|---|---|---|
| 110582-04 | 0.20 | 30 | 400 |
| 120582-03 | 0.33 | 40 | 580 |
| 100582-03 | 1.00 | 15 | 380 |
| 170582-05 | 1.70 | 10 | 450 |

$\tau$ : duration of the equilibrium phase

a : radius of the light emitting column.

Schlieren observations indicate a duration of the equilibrium at 0.33 Atm which is in agreement with the streak observations. Interferometric observations at 1.00 Atm show similar agreement. Interferometric observations at 0.33 Atm corresponding to times longer than 25ns were not obtained.

A detailed study of the dependence of the equilibrium time with filling gas pressure is not available, however Table 4-1 shows that the equilibrium time decreases with pressure.

t=6 ns t=13 ns t=20 ns

(a)

2 mm.

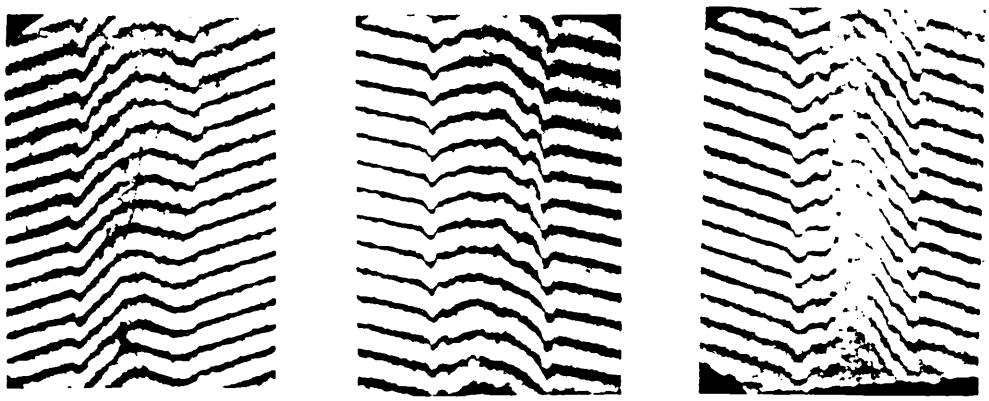

t=1 ns t=5 ns t=15 ns

(b)

Fig. 4-12: Sequence of interferograms corresponding to the equilibrium phase. (a) 0.33 Atm. (b) 1.00 Atm.

### 4.4.2 Interferometric observations

Fig. 4-12 is a sequence of interferograms corresponding to the equilibrium phase at 0.33 and 1.00 atmosphere. Note that the interferograms at 1.00 Atm. present less axial uniformity than at 0.33 Atm. This fact might be connected to the lower reproducibility observed at this pressure and discussed in §5.2.

### 4.4.3 The radius of the channel

Fig. 4-13 shows the radius of the plasma channel and high density neutral layer vs. time. The measurements were obtained from interferometric observations. The neutral boundary is seen to expand continuously with a mean velocity of 5.7 $m.s^{-1}$, which is less than the expansion velocity observed during preheat. The radius of the plasma channel is observed to remain constant within the accuracy of the measurement.

### 4.4.4 Particle density distributions

A typical interferogram corresponding to the equilibrium phase is shown in Fig. 4-14-a. The particle density profile obtained from the same interferogram is shown in Fig. 4-14-b. The elctron density distribution is observed to be peaked at the center. The high density neutral layer formed during preheat is seen at the edge of the electron density distribution.

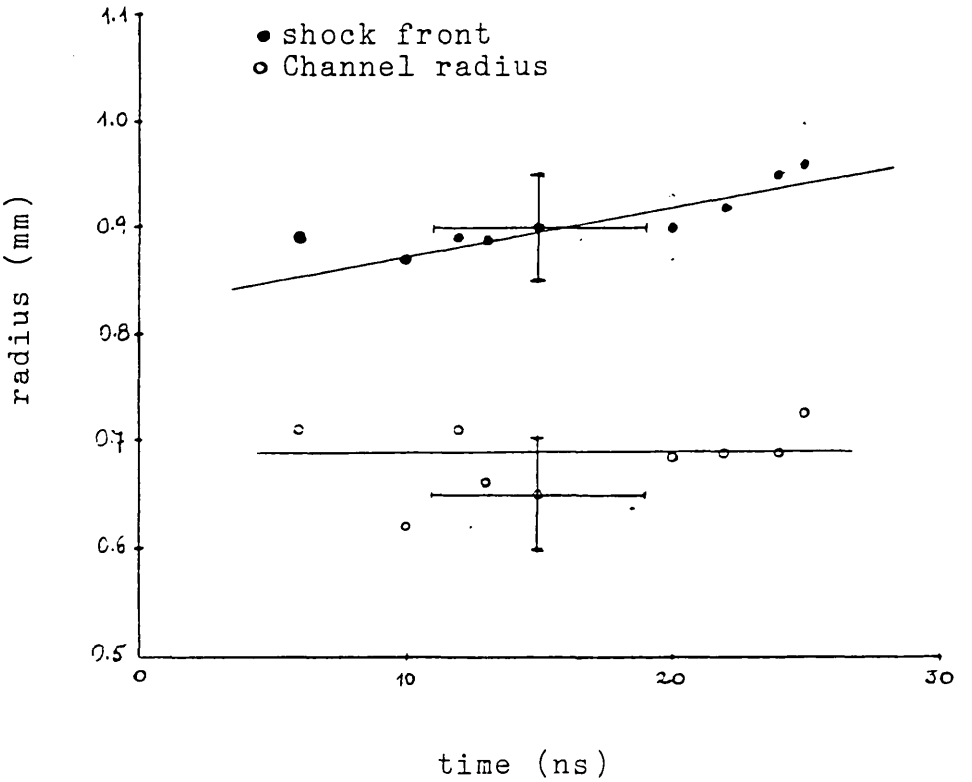


Fig. 4-13: The shock front and plasma channel radius during the equilibrium phase. Pressure: 0.33 Atm.

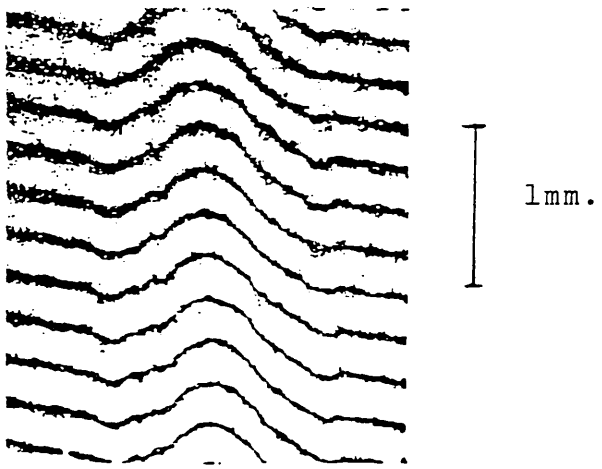


Fig. 4-14-a: Interferogram of the equilibrium phase. t=22 ns. Pressure: 0.33 Atm.

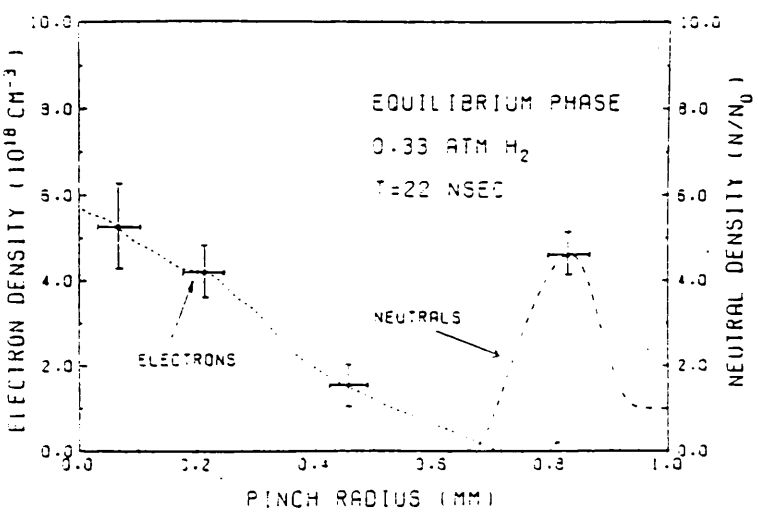


Fig. 4-14-b: Particle density profile corresponding to the interferogram shown in Fig. 4-14-a.

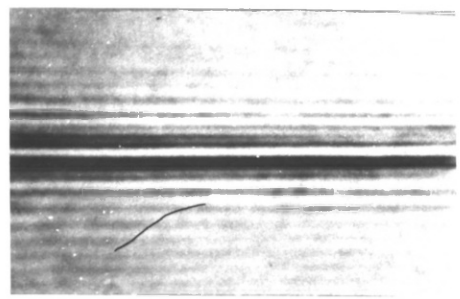

Fig. 4-15: Schlieren photograph of the equilibrium phase. t=28 ns.

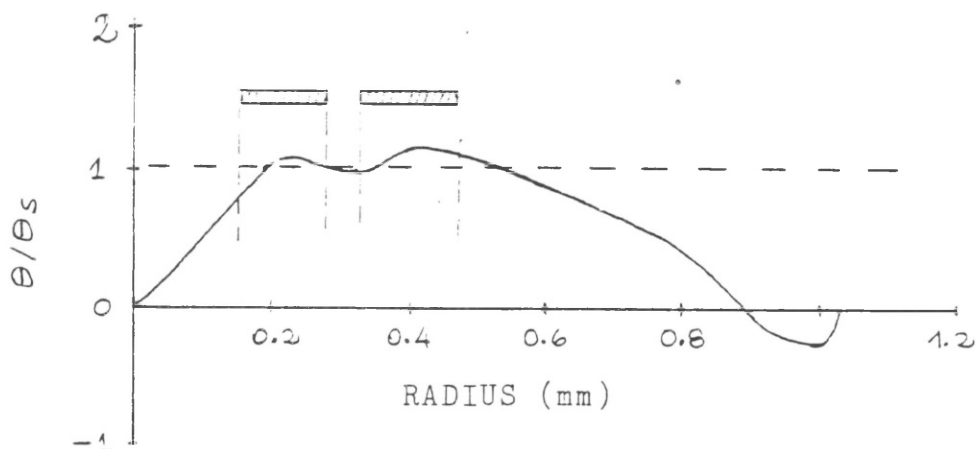


Fig. 3-16: Calculated schlieren defletion corresponding to the particle density profile shown in Fig. 4-14. The bars represent the dark fringes in the shlieren photograph shown in Fig. 4-15.

Fig. 4-15 is a schlieren photograph corresponding to the equilibrium phase at 0.33 Atm. Two dark fringes are observed each side of the pinch. In Fig. 4-16 is shown the calculated deflection angle for a particle density profile which correspondes to a similar time. The schlieren photograph is represented by thick lines on top of the figure. Good agreement is observed between the calculation and the schlieren photograph. The innermost fringe is due to the electron density gradient and the second one is produced by the inner side of the high density neutral layer. Deflection of light by the density gradient at the outer side of the high density neutral layer is calculated to be less than the schlieren angle.

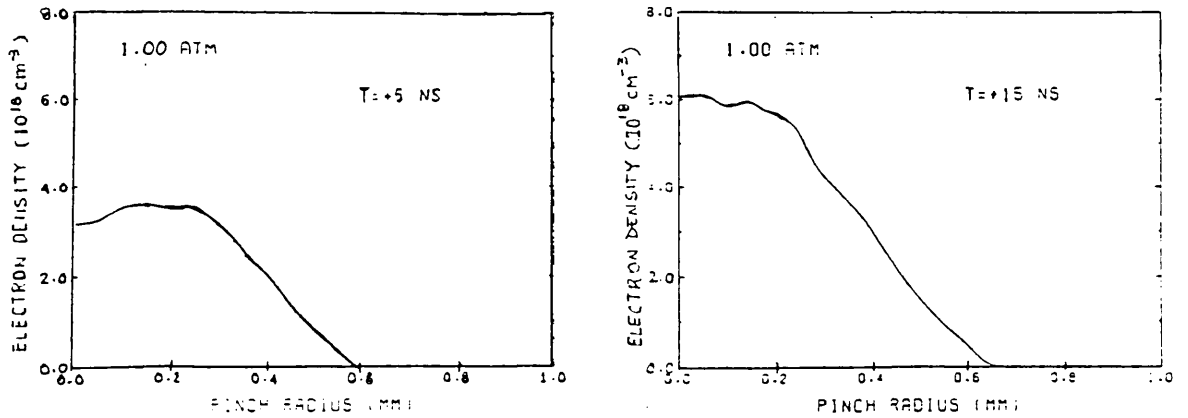


(a)

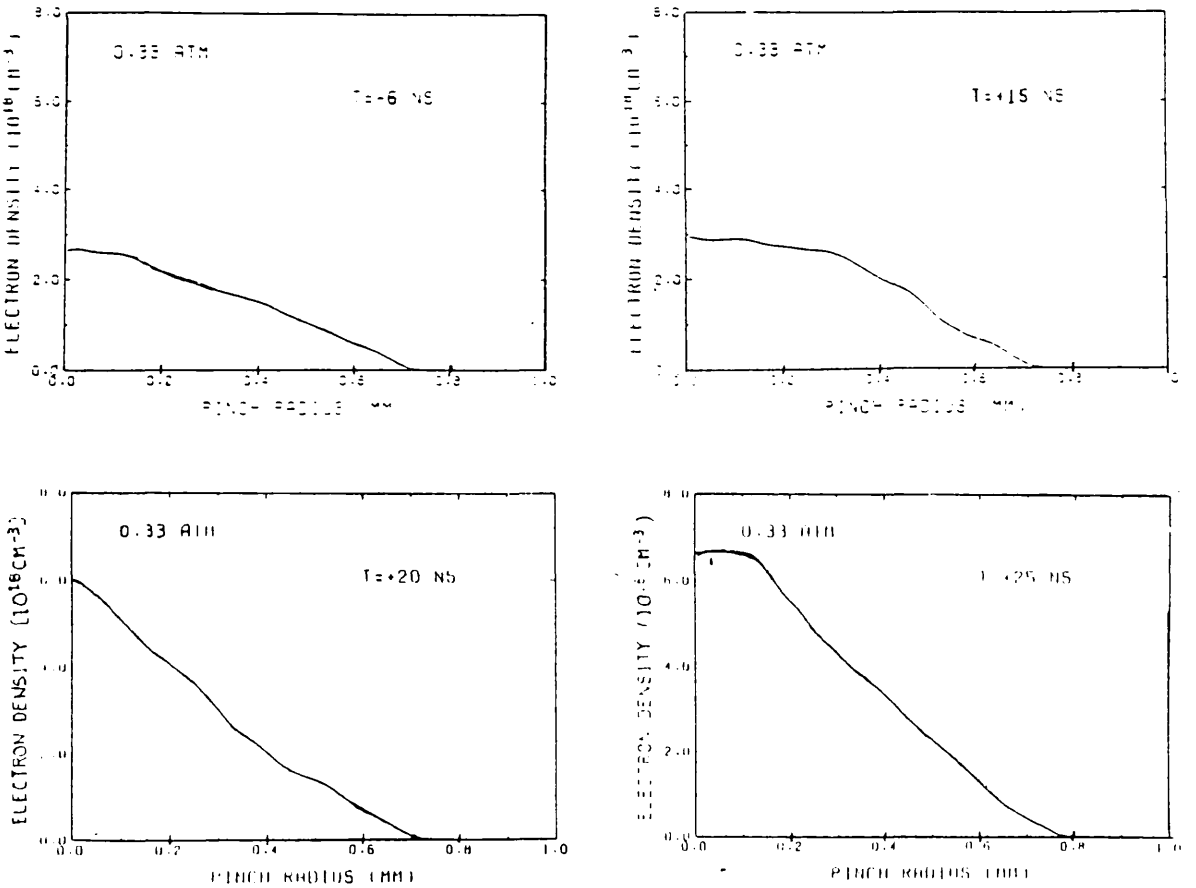


(b)

Fig. 4-17: Time history of the electron density profile during the equilibrium phase. (a) 1.00 Atm. (b) 0.33 Atm.

The evolution of the electron density profile at 0.33 and 1.00 Atm is shown in Fig. 4-17. The transition from a nearly flat electron distribution at the end of preheat to one that is peaked at the centre takes place in a very short time. Interferograms 6ns after the beginning of the main current show already a centre peaked electron density. A well defined pinch is observed throughout the equilibrium phase, with continuous increase of the electron density on axis.

Fig.4-18 shows the evolution of the electron line density during the equilibrium phase. Mean rates of increase of the electron line density estimated by a linear fit to the data are shown in Table 4-2. The increase in the electron line density can not be attributed to further ionization and it is indicative of plasma accretion, as discussed in § 5.4.5.

Table 4-2

Rate of increase of the electron line density

| pressure (Atm) | dNe/dt ($10^{17} m^{-1}$ $ns^{-1}$) |
|---|---|
| 0.33 | 0.7 ± 0.25 |
| 1.00 | 1.0 ± 0.25 |

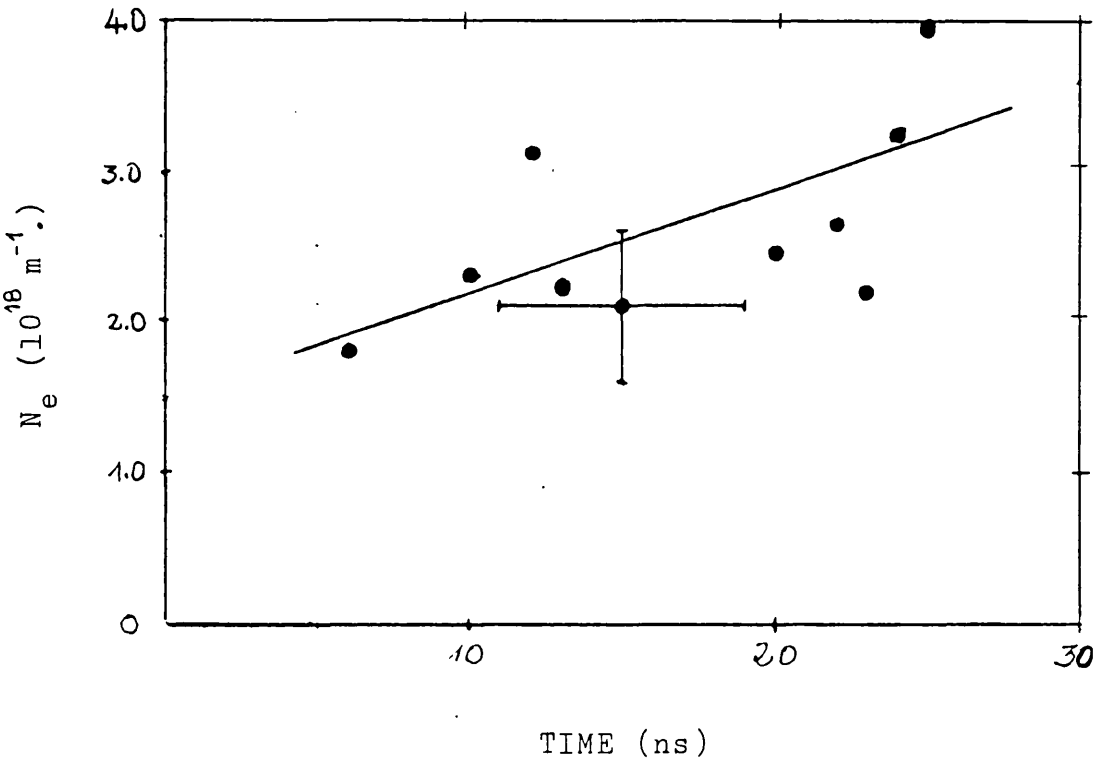


Fig. 4-18: The electron line density during the equilibrium phase. Pressure: 0.33 Atm.

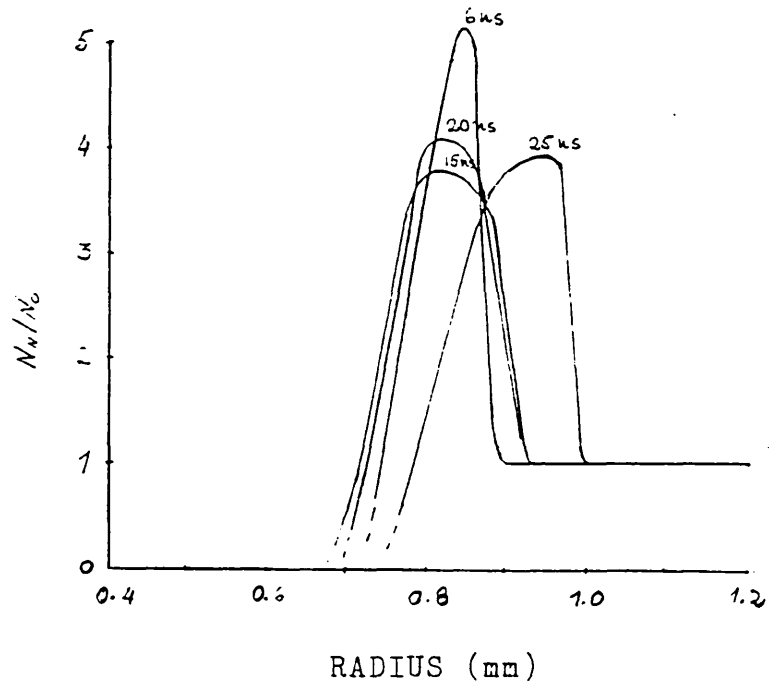


Fig. 4-19: The high density neutral layer during the equilibrium phase. Pressure: 0.33 Atm.

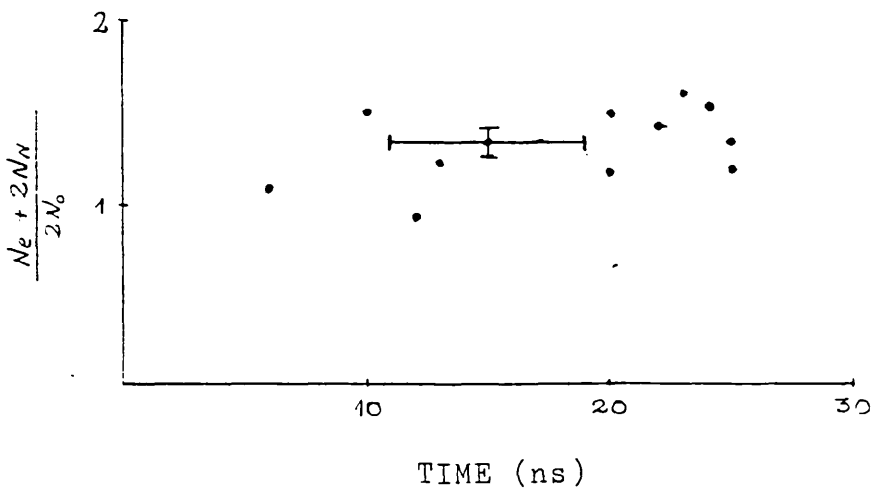


Fig. 4-20: Particle conservation during the equilibrium. A nearly constant degree of dissociation is observed. Pressure: 0.33 Atm.

The time development of the high density neutral layer at the pinch boundary is shown in Fig. 4-19.

Fig. 4-20 shows the evolution of the ratio $(Ne + 2N_N)/2N_o$ during preheat for 0.33 Atm. The ratio is observed to be greater than one during the time of observation, thus indicating molecular dissociation in the high density neutral layer. Fluctuations around mean value are within the acuracy of the observation, thus indicating a nearly constant ionization fraction.

## 4.5. The Unstable Phase

The equilibrium is followed by an unstable expansion of the plasma. The plasma column changes to a helical structure. Fig. 4-21 shows a sequence of framing camera photographs taken transversely to the pinch with a framing rate of $3.10^8$ frames. $s^{-1}$. The helix is observed to expand without disrupting.

Fig. 4-22 shows schlieren photographs taken transversely to the pinch at 1.00 Atm. It is observed that the instability is initially confined to the plasma channel. Later it grows reaching the boundary defined by the high density neutral layer, which is not affected in the early stages. Finally the whole column

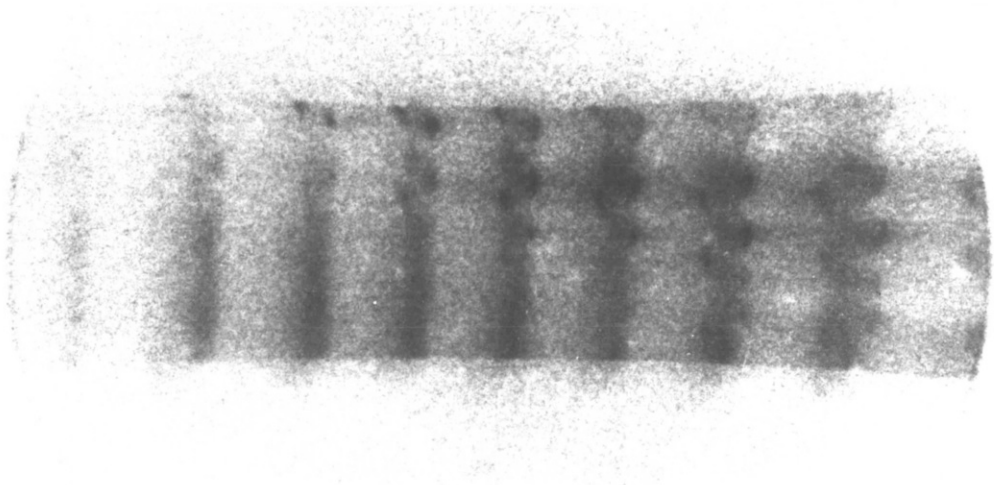

Fig. 4-21: Sequence of framing photographs showing the evolution of the helical instability.
Framing rate: $3.5 \cdot 10^{8}$ frames.$s^{-1}$.
Pressure: 1.00 atm.

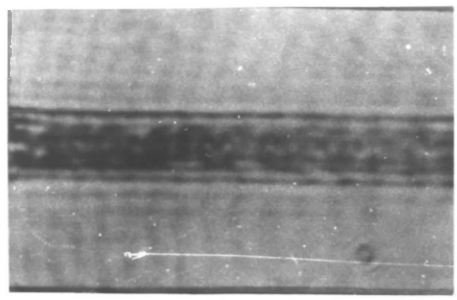

t=12 ns.

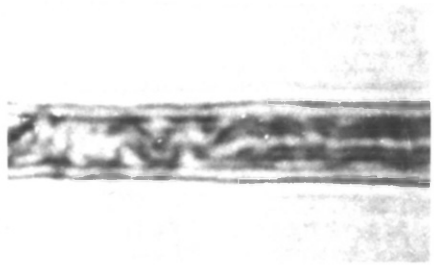

t=23 ns.

t=55 ns.

2mm.

Fig. 4-22: Sequence of side-on schlieren photograps showing the evolution of the helical instability. Pressure: 1.00 Atm.

turns into an expanding helical structure, which can be observed in the schlieren photograph at t=55 ns.

Fig. 4-23 shows an interferogram at 1.00 Atm filling pressure. Time is 22ns ± 4ns after the starting of the main current. Streak photographs indicate that typical duration of the equilibrium at 1.00 Atm is 15ns. A line tracing of the fringe pattern is included in the figure. A sinusoidal perturbation of the number density around the pinch axis is observed. The high density neutral layer at the pinch boundary is not disturbed. The wavelength associated to the perturbation is $\lambda$ = 0.89mm.

Fig. 4-24 shows an interferogram at t = 28 ± 4ns. The instability has grown and the whole column is perturbed. Fringes can not be followed to investigate the characteristics of the particle density distributions.

A measurement of the pitch of the instability can be obtained from the framing and schlieren observations. In a helical perturbation the wavelength corresponds to the pitch of the helix. Table 4-3 shows the observeed wavelengths. Corresponding values of $k.r_p$, where k is the wave number and $r_p$ the pinch radius, are also included in the table.

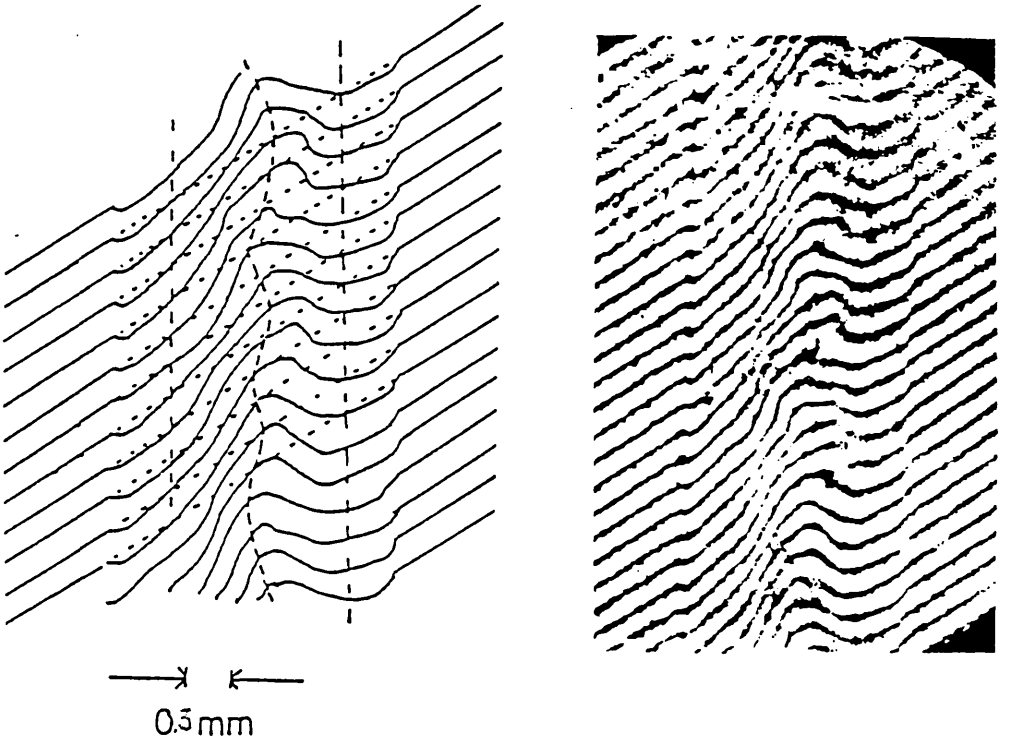


Fig. 4-23: Interferogram corresponding to the begining of the instability. Figure on the left is a hand trace showing that the neutral layer at the pinch boundary is not affected. Time=22 ns. Pressure=1.00 Atm.

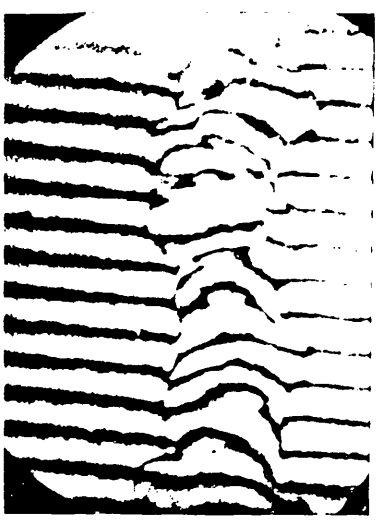

Fig. 4-24:Interferogram at later time showing the whole column perturbed by the instability. Time=28 ns. Pressure=1.00 Atm.

Table 4-3

Wavelength of the instability

| Pressure (Atm) | Diagnostics | $\lambda$ (mm) | $k.r_p$ |
|---|---|---|---|
| 0.33 | Framing | 1.6 | 1.7 |
| 0.33 | Schlieren | 2.0 | 1.64 |
| 1.00 | Schlieren | 1.3 | 1.67 |
| 1.00 | Interferometry | .89 | 4.16 |

The growth rate, $\gamma$, at early times of the instability can be measured from the radial expansion of the helix observed in the streak photographs. It is given by:

$$\gamma = \frac{1}{\xi(r)} \frac{d\xi(r)}{dt} \qquad 4\text{-}1$$

where $\xi(r)$ represents the position of a perturbed plasma element and $d\xi(r)$ the displacement from equilibrium. $d\xi(r)/dt$ and $\xi(r)$ can be measured from streak photographs. Table 4-4 shows typical growth rates in the pressure range 0.2-1.7 Atm.

Streak photographs show a decrease in growth rate when the radius of the helix is about four times the radius of the equilibrium pinch.

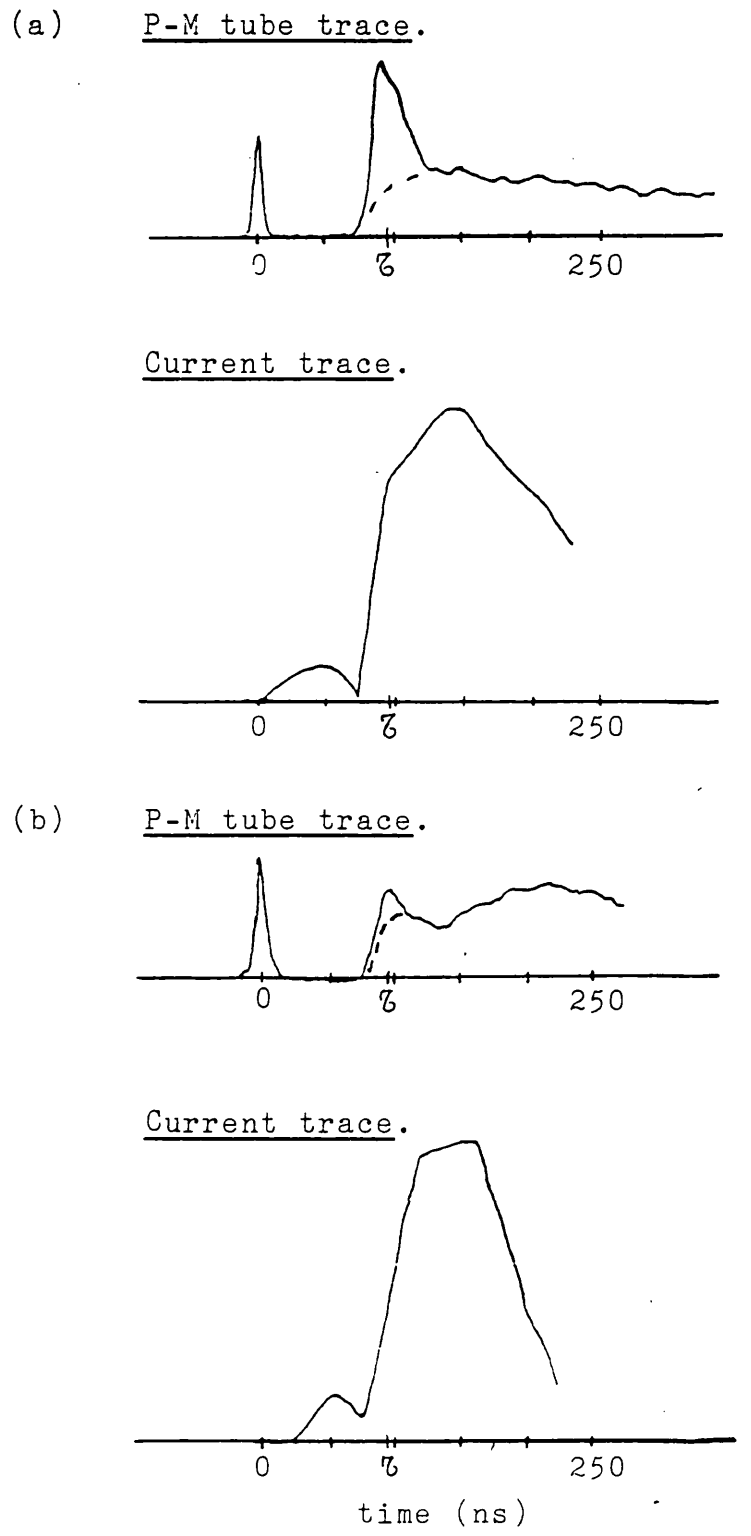


Fig. 4-25: Time correlated soft X-ray emission and current waveform. $\tau$ corresponds to the time when the instability develops. The dotted line corresponds to a collimated obsrvation that excludes emission from the electrodes. (a) 0.33 Atm. (b) 1.00 Atm.

Table 4.4

Measured growth rate of the instability

| Shot | Pressure (Atm) | $\gamma(10^8 s^{-1})$ |
|---|---|---|
| 110582 | 0.20 | 1.04 |
| 120582-04 | 0.33 | 0.73 |
| 040582-02 | 1.00 | 0.83 |
| 070582-06 | 1.70 | 0.60 |

## 4.6. Time Resolved X-ray Observations

Fig. 4-25 shows plasma emission at 0.33 and 1.00 Atm as a function of time. The current waveform is also shown to correlate the X-ray emission with the different pinch phases. $\tau$ on the time axis corresponds to the typical time of transition to the helical structure. The narrow signal at t=0 on both P-M traces corresponds to emission associated with plasma generated on the cathode by the initiating laser pulse.

X-ray emission from the plasma column starts at a time which is more or less coincident with the beginning of the main current pulse and reaches its maximum around the time when the pinch becomes unstable. When pinch emission is collimated to exclude radiation emitted from or near the

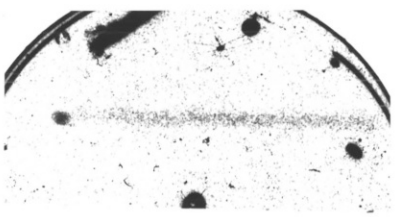

(a) Single shot - 0.33 Atm.

(b) Four shots - 0.33 Atm.

Fig. 4-26: Pin-hole X-ray photographs.
Filters: Al+Kim-foil. Radius of emitting region:~0.5mm.

electrodes, the P-M trace changes to the dotted line shown in the figure.

## 4.7. Time Integratd Soft X-ray Observations

Radiation from a pure hydrogen plasma was found insufficient to expose the X-ray film on a single shot basis: a mixture of hydrogen with 4% air was used as filling gas in order to enhance plasma radiation. A faint exposure was obtained in a single shot. To increase signal to noise ratio over background fog level, most of the results were obtained by integration over 3 to 5 shots. This procedure requires a high shot to shot reproducibility, so observations were concentrated on 0.33 Atm which represents a compromise between high temperature and reproducibility of plasma conditions.

Fig. 4-26 shows time integrated X-ray pin-hole photographs. Exposure varies from 3 to 5 shots. A column ~400μm radius is observed in each photograph. the dimensions are in general agreement with interferometric observations. The columns are not uniform and some structures can be seen. The spot at the end of the column appears in every photograph, regardless of the filling pressure and it is located close to the anode surface. Geometry of the pin-hole camera excludes the cathode from the observed volume, but preliminary observations showed

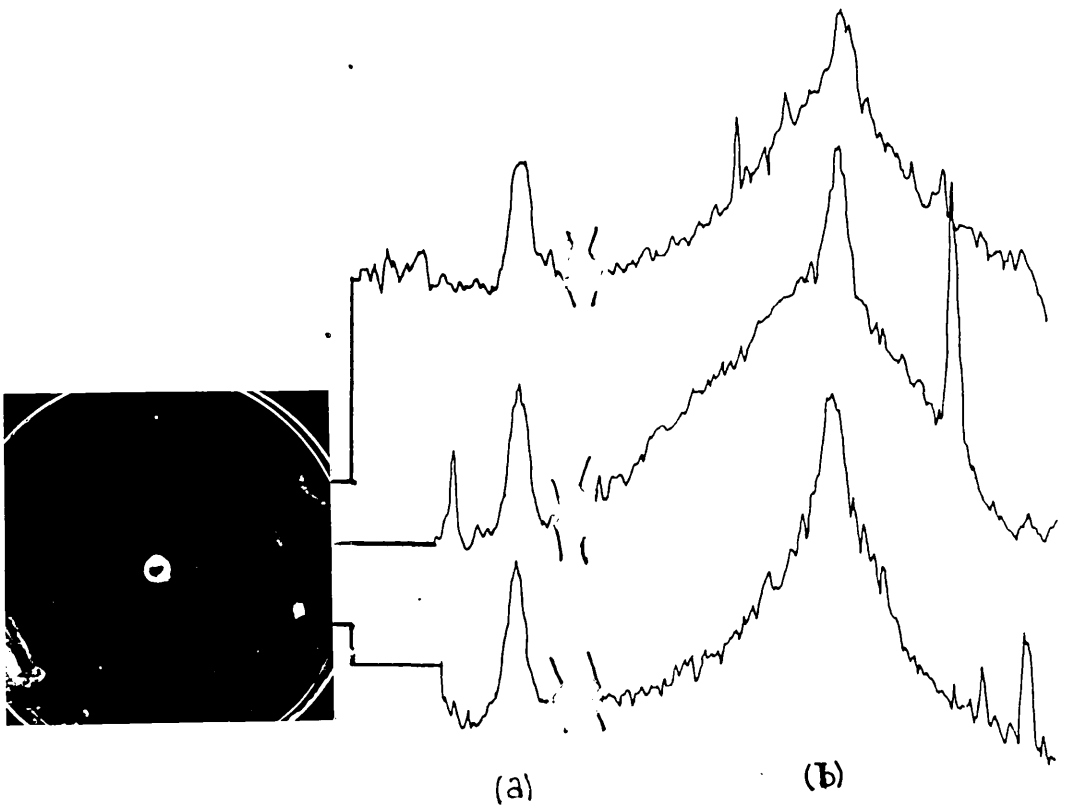


Fig. 4-27: Microdensitometer traces corresponding to three axial positions. Filters: (a) Al+Kim-foil, (b) Ag+Kim-foil. Pressure: 0.33 Atm.

that a similar spot was located at or close to the cathode surface. No attempt was made to investigate the nature of the spots but film exposure seems to indicate that they correspond to a source of harder radiation than the plasma column. Intensity of the anode spot (in terms of film density) was observed to decrease with the addition of air in the filling hydrogen. Single shot exposures with pure hydrogen produced an intense spot with no trace of the plasma column.

Fig. 4-27 shows typical microdensitometry traces of an exposure obtained by three shots at 0.33 Atm. The traces on the left correspond to an aluminium filter (F-5, Table 3-1) and the one on the right to a silver filter (F-3, Table 3-1). The image obtained with the Al filter is narrow, whereas that for Ag shows a narrow peak with a broad wing, which can be attributed to softer radiation emitted from the helical expansion phase. Scanning at different axial positions show no significant axial variation in the plasma emission.

A comparison of the observed ratio of exposure with the calculated one gives an estimation of the electron temperature. Results corresponding to 0.33 Atm are summarized in Fig. 4-28. Several filter combinations were used. Dots on the curves represent the measured ratios. An electron temperature Te = 69 ± 4 eV is inferred from the

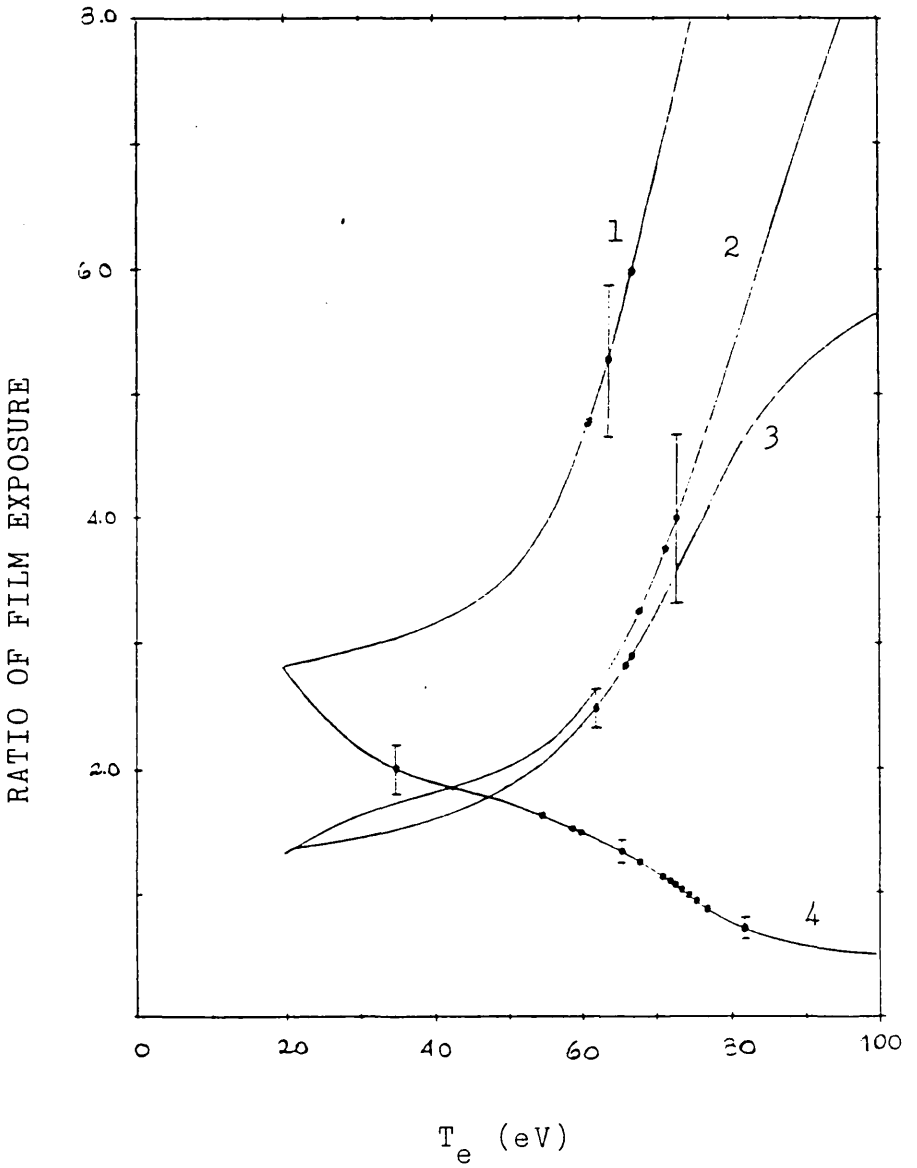


Fig. 4-28: Observed ratio of film exposure with different filter combinations. (1) F-4/F-1. (2) F-5/F-2. (3) F-3/F-4. (4) F-3/F-5. (Filters number as in Table 3-1)

figure. This value corresponds to the peak value in the microdensitometry traces. No significant axial fluctuations in the temperature were observed.

# CHAPTER V

## Discussion of Experimental Results

### 5.1. Introduction

The experimental results presented in the previous chapter are discussed in this chapter and an interpretation of some experimental observations is proposed. The laser initiation, preheat, equilibrium and unstable phase are discussed separately.

### 5.2. Laser Initiation

Typical voltages across the pinch electrodes at the time when the initiating laser pulse if fired are 20kV at 0.33 Atm. and 30kV at 1.00 Atm. The self-breakdown voltage for a 3 cm gap in hydrogen is 17 kV at 0.33 Atm and 43 KV at 1.00 Atm. This indicates that at the higher pressure the discharge is initiated at ~70% of self-breakdown voltage, whereas at the lower pressure initiation takes place close to the self-breakdown voltage. The experimental evidence of a more reproducible and uniform discharge at 0.33 Atm. seems to indicate that best results are obtained when the pinch electrodes are slightly over volted at the time when the laser pulse is fired.

## 5.3. Preheating Phase

### 5.3.1. A model of the preheating discharge

According to the experimental observations three main features characterize the preheating discharge:

i) the electron density remains nearly constant,

ii) the column expands with a velocity higher than the sound speed in the background gas, and

iii) a high density neutral layer builds up at the edge of the discharge channel.

Based on these results a simplified picture of the development of the discharge channel can be proposed. After pinch initiation a narrow current-carrying channel is formed in the gas, with high temperature and degree of ionization. Joule heating leads to an increase in the pressure and the channel expands. The channel expansion takes place faster than the sound speed and a shock is produced in the surrounding gas. The expanding channel acts as a piston, which sweeps-up the neutral gas as in the snow plough model and the high density neutral layer is formed. Neutrals are heated by the shock and dissociation takes place.

### 5.3.2. The expansion of the preheating channel

Braginskii (1958) proposed a theory for the development of a discharge channel in a high pressure gas. The equations describing the evolution of the channel are the continuity equation, the equation of motion and the equation of energy transfer. The physical processes determining the channel expansion are radial thermal conduction and pressure increase due to Joule heating. The current is assumed to be fully diffuse and the magnetic field pressure is neglected. This is justified by estimating the skin depth to be much greater than the radius of the discharge channel. The plasma line density is assumed to be constant. Dissociation of neutrals behind the shock front is neglected.

The boundary of the discharge channel plays the role of a piston which displaces the neutral gas surrounding the channel. If the time dependence of the radius of the discharge channel $r_c$ is given by:

$$r_c(t) = At^k \qquad 5\text{-}1$$

and if the pressure behind the shock front is much greater than the ambient gas pressure, then the motion in the region behind the shock is determined by the parameters A and $\rho_o$, where $\rho_o$ is the pressure of the background gas. Under these conditions the motion in the region behind the shock is self-similar.

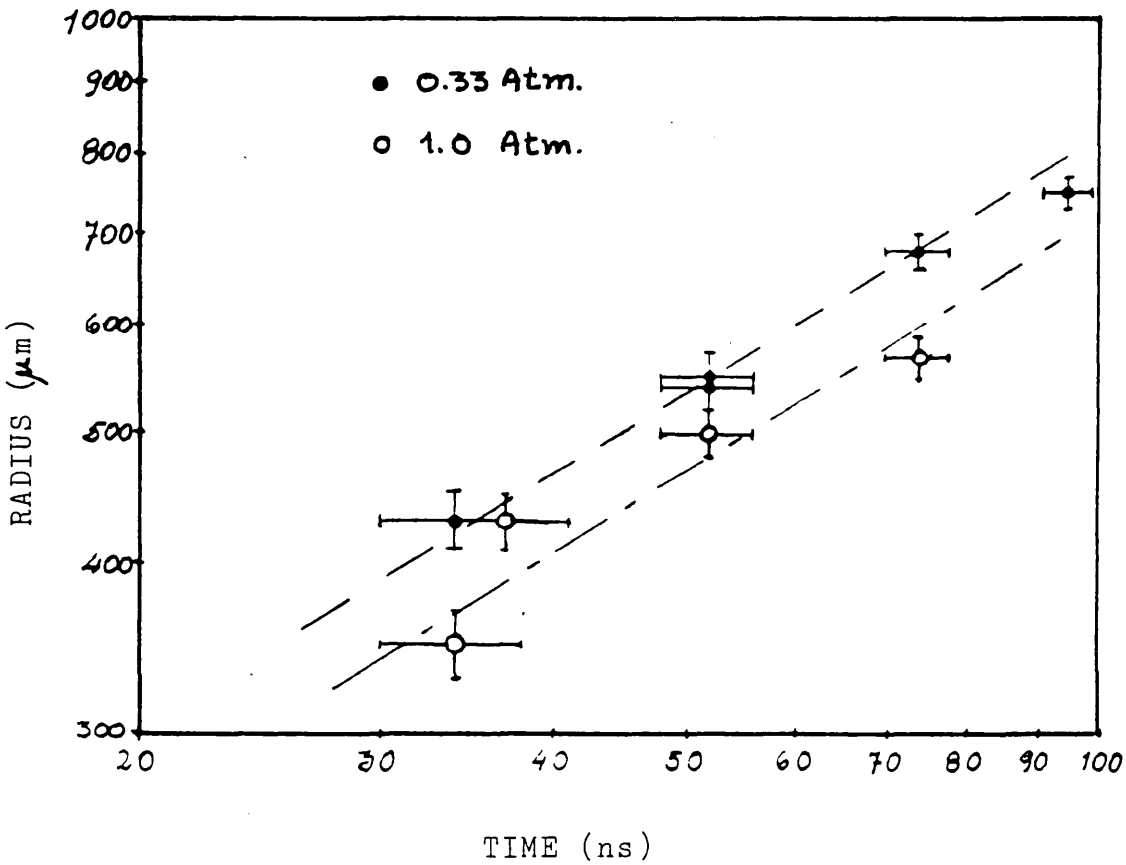


Fig. 5.1: Radial expansion of the discharge channel during preheat.

In a self-similar motion the position of the channel boundary and the shock front are linearly related, so the radius of the shock $r_s$ has the same time dependence:

$$r_s(t) = A' t^k \qquad 5\text{-}2$$

The value of k and A' can be determined from the observed evolution of the shock front, which is defined by the outer boundary of the high density neutral layerr. Fig. 5-1 shows a log-log plot of $r_s$vs t, at two pressures. From the experimental data for $r_s(t)$ a value of k = 0.6 is obtained at both pressures, with A' = 12.8 $m.s^{-3/5}$ at 0.33 Atm and A' = 11.4 $m.s^{-3/5}$ at 1.00 Atm.

The velocity, pressure and density in the region behind the shock have been calculated by Braginskii (1958) for different values of k and the ratio of specific heats $\gamma$. With k=0.6 and $\gamma$=7/5, the calculation gives A'/A=1.28. This value is obtained under the assumption of a strong shock, where the density jump across the shock front is given by:

$$\frac{\rho}{\rho_o} = \frac{\gamma+1}{\gamma-1} \qquad 5\text{-}3$$

Eq. 5-3 assumes M >> 1 where M is the Mach number associated with the shock.

It is difficult to estimate the ratio $\rho/\rho_o$ in the experiment because of dissociation in the high density neutral layer. For 0.33 Atm the ratio $n_n/n_o$ at peak density is around 6.5 at t=52ns. The dissociation fraction is estimated around 20% (see §5.3.4.). This indicates that at peak density $\rho/\rho_o \approx 5.7$ which is close to $\rho/\rho_o = 6$ obtained from Eq.5-3 with $\gamma = 7/5$. The mean Mach number is estimated to be $M \approx 6.9$ at the same pressure, which agrees with the above calculation.

Using the experimental values k = 0.6 and A'=12.8 and Braginskii's value A'/A=1.28, the self-similar expansion of the discharge channel at 0.33 Atm. is given by:

$$r_c(t) = A.t^k = 10.t^{0.6} \text{ m} \qquad 5\text{-}4$$

where t is in sec. From Eq.5-4 the radial expansion velocity of the channel is:

$$\dot{r}_c(t) = 6.03.t^{-0.4} \text{ m.s}^{-1} \qquad 5\text{-}5$$

The channel expansion predicted by the theory is compared with the experimental data in Fig.5-2.

In Braginskii's theory a self-similar expansion of the plasma channel as a function of the current is found when the current is proportional to $t^{0.75}$. In the experiment the

preheating current changes sinusoidally, but for the first quarter of cycle it can be taken as proportional to $t^{0.75}$ This is shown in Fig.5-3.

According to Braginskii the radius of the plasma channel in hydrogen is given by:

$$r_c(t)=1.53.10^3\rho_o^{-5/28}(I.t^{-0.75})^{2/7}.t^{0.75}\ \mu m \qquad 5-6$$

where $\rho_o$ is the background density in Atm, I is the current in kA and t is the time in μs. By differentiating Eq.5-6, the channel expansion velocity is given by:

$$\dot{r}_c(t) = 8.2.10^2\rho_o^{5/28}.I^{2/7}.t^{-13/28}\ m.s^{-1} \qquad 5-7$$

Calculated values of $r_c$ and $\dot{r}_c$ at the time of maximum current can be compared with an extrapolation of the experimental data. Results at 0.33 Atm are shown in Table 5-1. The time is t=20ns and the current I=4.4kA.

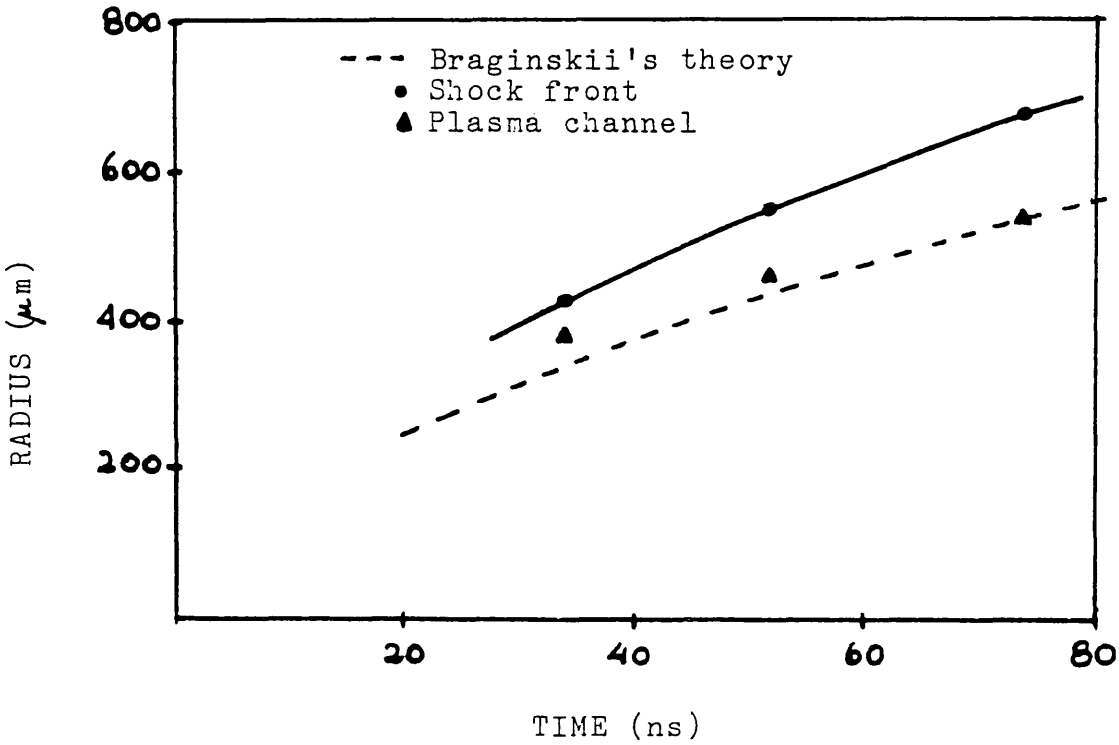


Fig. 5.2: Expansion of the preheating channel at 0.33 Atm. Experimental and predicted values using Braginskii's theory are shown.

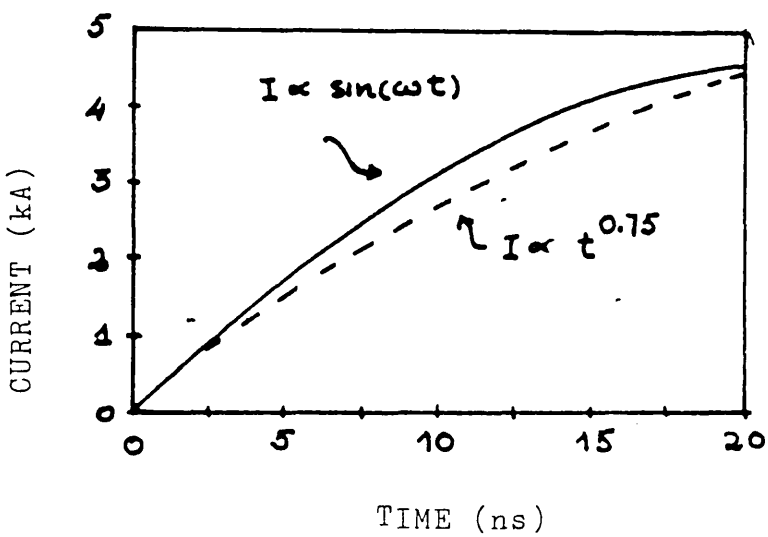


Fig 5.3: Comparison of the first quarter cycle of the preheating current with an $I \propto t^{0.75}$ current.

Table 5-1

Expansion of the preheating channel

| Extrapolated values | | Braginskii's theory | |
|---|---|---|---|
| $r_c$ (μm) | $\dot{r}_c$ ($m.s^{-1}$) | $r_c$ (μm) | $\dot{r}_c$ ($m.s^{-1}$) |
| 280 | 9.0 | 350 | 9.3 |

Pressure: 0.33 Atm

Time: t=20ns

Considering that the theory does not include molecular dissociation behind the shock front, the agreement with the experimental data is satisfactory.

5.3.3. The temperature of the preheating channel

The fact that the channel expands indicates that the kinetic pressure is greater than the magnetic pressure due to the self magnetic field of the current. An absolute minimum for the temperature in the plasma channel can be estimated by using the Bennett relation, $\mu_o I^2 = 16\pi N_e kTe$, which assumes pressure balance. At 0.33 Atm and at the time of maximum current, a temperature $T_e \geq 4eV$ is required for the channel to expand.

In Braginskii's theory of the channel expansion with $I(t) \alpha t^{0.75}$, the temperature in the channel for hydrogen is given by:

$$T_e = 3.5 . \rho_o^{1/14} . (I . t^{-0.75})^{2/7} \text{ eV} \qquad 5\text{-}8$$

where $\rho_o$ is the background density in Atm, I is the current in kA and t is the time in μs. Using Eq.5-8, the temperature at 0.33 Atm, with t=20ns and I=4.4kA is predicted to be $T_e$=11eV.

Tholl (1967) has measured the temperature and density of spark channels in hydrogen at 0.6 Atm. The discharges were produced in a 2cm gap with a peak current of 1.8kA in the first half cycle. The period of the current was 600ns. The measured temperature at t=20ns was 2.4eV, rising to a maximum of 4.5ev at t=150ns, which corresponds to the time of maximum current. At t=20ns Braginskii's theory predicts $T_e$=5.9eV and $r_c$=155μm. The observed radius of the channel was 130μm. At peak current the predicted temperature is 6eV. These results indicate that the theory by Braginskii tends to overestimate the temperature of the plasma channel.

The experiment reported by Tholl was characterized by a higher gas pressure and lower current than in the preheating discharge at 0.33 Atm, so a higher temperature is to be expected in this case. Hence, it can be concluded

that the temperature in the preheating channel at 0.33Atm is in the 4-11 eV range.

The theory by Braginskii can not be applied to the non-preheated gas-embedded Z-pinches reported by Hammel et al (1983) and Jones et al (1981). The high temperature, $T_e$>100eV, and fast rate of rise of current, $\dot{I}\sim 10^{12} A.s^{-1}$, break the assumption on the skin depth and make magnetic pressure effects to become important.

## 5.3.4. The high density neutral layer

The temperature and electron density in the high density neutral layer can be estimated by using the Saha relations for molecular dissociation and atomic ionization. The method is as follows:

i) The atomic $N_H$ and molecular $N_{H_2}$ line densities are calculated from the measured electron, $N_e$, and neutral $N_N$, line densities, by assuming particle conservation.

ii) The mean atomic, $\bar{n}_H$, and molecular, $\bar{n}_{H_2}$, number densities are calculated from $N_H$ and $N_{H_2}$ using the observed values of the pinch radius and thickness of the high density neutral layer, and

iii) The mean electron temperature, $\bar{T}_e$, and electron density, $\bar{n}_e$, in the layer are estimated from the Saha relations using the calculated values of $\bar{n}_H$ and $\bar{n}_{H_2}$.

Assuming no overlapping of the electron and neutral density distributions, the condition of conservation of number of particles is given by:

$$N_F = \frac{N_e}{2} + \frac{N_H}{2} + N_{H_2} \qquad 5\text{-}9$$

where $N_F$ is the line density of hydrogen molecules in a cylinder of the same radius as the shock front, $N_e$ is the measured electron line density in the discharge channel and $N_H$ and $N_{H_2}$ are the line density of atomic and molecular hydrogen in the high density neutral layer. The measured neutral line density $N_N$ is given by:

$$N_N = N_H + N_{H_2} \qquad 5\text{-}10$$

$N_H$ and $N_{H_2}$ are calculated from Eqs.5-9 and 5-10:

$$N_H = 2.(N_N - N_F) + N_e \qquad 5\text{-}11$$

$$N_{H_2} = 2N_F - (N_N + N_e) \qquad 5\text{-}12$$

Thus, $\bar{n}_H$ and $\bar{n}_{H_2}$ are given by:

$$\bar{n}_{H,H_2} = \frac{N_{H,H_2}}{2\pi \cdot r_c \cdot (r_s - r_c)} \qquad 5\text{-}13$$

The degree of dissociation $\alpha$ is given by:

$$\alpha = \frac{N_H}{N_H + 2N_{H_2}} \qquad 5\text{-}14$$

If the following molecular reaction takes place in equilibrium

$$A + C \rightleftharpoons AC \qquad 5\text{-}15$$

where A and C are the atomic species and AC is the molecular species, the atomic number densities, $n_A$, and $n_C$, and the molecular number density, $n_{AC}$, are related through the Saha distribution (Smirnov, 1977):

$$\frac{n_A \cdot n_C}{n_{AC}} = \frac{g_A \cdot g_C}{g_{AC}} \left( \frac{\mu k T}{2\pi \hbar^2} \right)^{3/2} \cdot \frac{B}{kT} \left[ 1 - \exp\left( - \frac{\hbar\omega}{kT} \right) \right] \cdot \exp\left( - \frac{D}{kT} \right) \qquad 5\text{-}16$$

where $g_A$ and $g_C$ are the statistical weights of atoms A and C, $g_{AC}$ is the statistical weight for the ground state of the molecule, $\mu$ is the reduced mass of the molecule, B is the rotational constant, $\hbar\omega$ is the energy of the lowest

vibrational state and D is the dissociation energy. In hydrogen: $g_H=g_{H_2}=1$, $\mu=\frac{m_p}{2}$, $B=7.6.10^{-3}eV$, $h\omega=0.54eV$ and $D=4.5eV$. With these values, Eq.5-16 gives for hydrogen:

$$\frac{n_H^2}{n_{H_2}} = 6.3.10^{23}.T^{\frac{1}{2}}.[1-\exp(-\frac{0.54}{T})].\exp(-\frac{4.5}{T})\ cm^{-3} \qquad 5\text{-}17$$

where T is in eV.

Values of the ratio $n_H^2/n_{H_2}$ are shown in Table 5-2 for temperatures in the range 0.2-1.0eV.

Table 5-2

Saha dissociation equilibrium

| T(eV) | $n_H^2/n_{H_2}\ (cm^{-3})$ |
|---|---|
| 0.2 | $4.3.10^{13}$ |
| 0.4 | $3.8.10^{18}$ |
| 0.6 | $1.5.10^{20}$ |
| 0.8 | $1.0.10^{21}$ |
| 1.0 | $2.9.10^{21}$ |

The values in Table 5-2 indicate that the ratio $n_H^2/n_{H_2}$ is very sensitive to the temperature so an estimate of the temperature can be made based on the mean values $n_H$ and $n_{H_2}$.

The electron number density $n_e$, the number density of neutral atoms $n_n$ and ions of the same species $n_+$, are related through the Saha distribution (Smirnov, 1977):

$$\frac{n_e \cdot n_+}{n_n} = \frac{2 \cdot g_+}{g_n} \left( \frac{M_e k T_e}{2\pi h^2} \right)^{3/2} \exp\left(- \frac{E_\infty}{k T_e} \right) \qquad 5\text{-}19$$

where $g_+$ and $g_n$ are the statistical weights of ions and atoms and $E_\infty$ is the ionization energy. For hydrogen in the ground state $g_+ = g_n = 2$, $n_e = n_+$ and $E_\infty$ = 13.6 eV. With these values, Eq.5-19 gives

$$\frac{n_e^2}{n_H} = 6.04 \cdot 10^{21} \cdot T_e^{3/2} \exp(-13.6/T_e) \, cm^{-3} \qquad 5\text{-}20$$

where $T_e$ is in eV.

The characteristic time for thermal equilibration between electrons and neutrals, $\tau_{e-n}$, is given approximately by (Zel'dovich and Raizer, 1967):

$$\tau_{e-n} \approx \frac{m_n}{2m_e} \cdot \frac{1}{n_n \cdot \sigma_{e-n} \cdot \bar{v}_e} \qquad 5\text{-}21$$

where $\sigma_{e-n} \approx 5 \cdot 10^{-15} cm^{-2}$ is the mean electron-neutral collision cross-section and $\bar{v}_e$ is the mean electron velocity over a Maxwellian distribution, which is given by:

$$\bar{v}_e = \left( \frac{8kT_e}{\pi m_e} \right)^{\frac{1}{2}} \qquad 5\text{-}22$$

For $n_n \simeq 2.10^{19} cm^{-3}$ and $T_e \simeq 0.5eV$, $\tau_{e-n}$ is estimated to be about 0.2ns. This indicates that the electron and neutral distributions in the high density neutral layer are characterized by the same temperature.

Characteristic parameters of the neutral layer are summarizad below:

Table 5-3

Characteristic parameters of the high density neutral layer

| t(ns) | $N_H(cm^{-2})$ | $N_{H_2}(cm^{-1})$ | $n_H(cm^{-3})$ | $n_{H_2}(cm^{-3})$ | $n_e(cm^{-3})$ | $\alpha$ | $T_e(eV)$ |
|---|---|---|---|---|---|---|---|
| 34 | $6.7.10^{16}$ | $1.5.10^{16}$ | $5.6.10^{19}$ | $1.3.10^{19}$ | $4.7.10^{15}$ | 0.70 | 0.6 |
| 52 | $4.9.10^{16}$ | $1.0.10^{16}$ | $1.8.10^{19}$ | $2.7.10^{19}$ | $2.4.10^{14}$ | 0.20 | 0.5 |
| 74 | $4.9.10^{16}$ | $1.3.10^{16}$ | $1.0.10^{19}$ | $2.6.10^{19}$ | $2.6.10^{12}$ | 0.16 | 0.4 |

In a hydrodynamic shock the density and temperature jump across the shock front are given by (D. Book, 1983):

$$\frac{\rho'}{\rho_o} = \frac{(\gamma+1)M^2}{(\gamma-1)M^2+2} \qquad 5\text{-}23$$

$$\frac{T'}{T_o} = \frac{((\gamma-1)M^2+2)(2\gamma M^2-\gamma+1)}{(\gamma+1)^2 M^2} \qquad 5\text{-}24$$

where $\rho'$ and $\rho_o$ are the density behind the shock and in the background gas, T' and $T_o$ are the temperature behind the shock and in the background gas, $\gamma$ is the ratio of specific heats and M is the Mach number.

At 0.33 Atm the observed mean shock velocity is $8.7.10^3 m.s^{-1}$ which corresponds to M=6.7, for a background temperature $T_o=2.5.10^{-2}eV$. Using these values and taking $\gamma=7/5$, the density jump is estimated $\rho'/\rho_o \approx 5.4$ and the temperature behind the shock $T' \approx$ 0.25 eV. The density jump is of the same order of the value $\rho'/\rho_o \approx 5.7$ estimated at 52ns, with a dissociation fraction $\alpha=0.20$. The temperature is of the order of the values shown in Table 5-3.

The estimated electron density is several orders of magnitude smaller than the neutral density. Inside the plasma channel the neutral density can be estimated using the Saha relation Eq.5-20. Assuming $T_e \approx 8eV$ and taking $n_e=9.8.10^{17}cm^{-3}$, which corresponds to the observed values

$N_e=9.3.10^{15}cm^{-1}$ and $r_p=5.5.10^{-4}m$ at t=52ns, the neutral density in the channel is estimated $n_n \approx 3.8.10^{13}cm^{-3}$. This indicates that the assumption of no overlapping of the electron and neutral particle distributions is justified.

### 5.3.5. The electron density distribution

Electron density profiles measured by Tholl (1967) show the same nearly uniform distribution with a minimum on axis at early times, as observed during the preheating discharge. Similar radial profiles are observed in the expanding plasma produced by laser breakdown in high pressure gases (Ostrovsky et al, 1980) and in the spark column of a laser triggered high voltage switch (Kimura et al, 1985). For a temperature of 10eV and a column radius of 250μm the ion sound radial transit time is calculated to be ~5ns. This indicates a nearly uniform pressure over the cross-section of the discharge channel. A nearly uniform pressure and electron density profile is indicative of a nearly uniform temperature distribution.

A 1-D two fluid M.H.D. numerical simulation (Parfenov, 1984) with parameters similar to those corresponding to the prheating discharge shows good agreement with the experimental results. The simulation gives a uniform temperature distribution and a nearly uniform electron

density profile with a minimum on axis at early times. A high density neutral layer is formed at the pinch boundary.

## 5.4 The Equilibrium Phase

According to the experimental observations, the main characteristics of the equilibrium phase are:

i) the radius of the discharge channel remains constant whereas the high density neutral layer continues to expand with a velocity higher than the sound speed in the background gas

ii) the electron line density increases in time, and

iii) the electron density distribution evolves into a bell shaped distribution, which is peaked on axis.

Based on these results, the following picture of the equilibrium can be proposed. At the time when the main current is injected a well defined plasma channel has been formed. The main current pulse heats the plasma channel. The rate of rise of current is such that radial equilibrium is achieved and the expansion of the plasma is stopped. Neutral particles diffuse into the plasma channel and become ionized causing the growth of the plasma line density.

Plasma particles are driven to the pinch axis by the JxB force and the density at the centre increases.

## 5.4.1. Initial conditions for radial equilibrium

The condition on $\dot{I}$ at early times (Eq.1-19) for a pinch to be Joule heated in radial equilibrium can be written, using Spitzer transverse resistivity, as:

$$\dot{I} \approx 5.5.10^{-4} \frac{\ell n\ \Lambda}{r_p^{\,2}} \cdot \frac{N_e^{\frac{1}{2}}}{T_e} A.s^{-1} \qquad 5\text{-}25$$

Using measured plasma parameters for 0.33 Atm at the end of preheat, $N_e=7.10^{17}m^{-1}$, $r_p=5.5.10^{-4}m$ and the initial rate of rise of current $\dot{I}\simeq 8.10^{11}A.s^{-1}$, the plasma temperature for an equilibrium pinch is estimated around 8 to 10eV. These values are in the 4-11eV temperature range estimated for the preheat.

## 5.4.2. The high density neutral layer

During preheat the shock in the neutral background gas is driven by the expansion of the plasma channel acting as a piston. When radial equilibrium is attained the piston effect disappears but the shock continues propagating. The mean expansion velocity of the neutral boundary during the equilibrium at 0.33Atm is $v_r=5.7.10^{3}m.s^{-1}$. This is approximately the same as the shock velocity at the end of

preheat which from the experimental observations is estimated at $5.6.10^3 m.s^{-1}$.

An estimate of the time taken by the shock to dissipate its energy can be obtained by assuming that no more energy goes into the shock after the channel expansion stops. Using approximations, similar to those of Zel'dovich and Reizer in their treatment of point explosions, but modified for cylindrical symetry it can be shown that the upper limit to the shock velocity is given by:

$$v_s(t) = \frac{dr_s}{dt} = A_o . r_s^{-1}(t) \qquad 5\text{-}26$$

where $A_o$ depends on the initial energy in the shock, the ratio of specific heats and the background gas density. Eq.5-26 can be integrated to give:

$$r_s(t) = (r_s(o)^2 + 2.A_o.t)^{\frac{1}{2}} \qquad 5\text{-}27$$

Eqs: 5-26 and 5-27 can be combined to give:

$$v_s(t) = \frac{A_o}{(r_s^2(o) + 2.A_o.t)^{\frac{1}{2}}} \qquad 5\text{-}28$$

From Eq. 5-28 the time $\tau_{\frac{1}{2}}$ for the propagation velocity of the shock to decrease to one half of the initial value $v_s(o)$, is given by:

$$\tau_{\frac{1}{2}} = \frac{3}{2} \frac{r_s(0)}{v_s(0)} \qquad 5\text{-}29$$

For 0.33 Atm, $r_s(0) \approx 5.5.10^{-4}$m and $r_s(0) \approx 5.6.10^{3}$m.s$^{-1}$, which gives $\tau_{\frac{1}{2}} \approx 0.15\mu$s. This time is much longer than the 40ns duration of the equilibrium phase at the same pressure.

Atomic and molecular hydrogen densities can be calculated in the same way as in the preheating phase. Mean values of characteristic parameters of the high density neutral layer are shown in Table 5-4.

Table 5-4

Characteristic parameters of the high density neutral layer during the equilibrium

| $N_H(cm^{-3})$ | $N_{H_2}(cm^{-3})$ | $n_H(cm^{-3})$ | $n_{H_2}(cm^{-3})$ | $n_e(cm^{-3})$ | $T_e$(eV) | |
|---|---|---|---|---|---|---|
| $1.6.10^{17}$ | $1.3.10^{17}$ | $1.9.10^{19}$ | $1.5.10^{19}$ | $5.5.10^{11}$ | 0.38 | 0.35 |

## 5.4.3 Ionization processes in the high density neutral layer

The ionization is due to the heating of the neutral gas produced by radial thermal conduction and dissipation of

the shock energy and also by direct absorption of plasma radiation.

According to the values in Table 5-4, the electron density in the high density neutral layer is estimated at around $5.10^{11}cm^{-3}$, for 0.33Atm.

At electron densities below $10^{17}cm^{-3}$ the relevant processes in determining ionization equilibrium are photionization and photorecombination (Zel'dovich and Raizer, 1967). According to this, the electron density in the high density neutral layer $n_e^n$ is given by:

$$\frac{dn_e^n}{dt} = \alpha_\nu n_n - \beta_\nu n^+ n_e^n + \dot{n}_\nu \qquad 5\text{-}30$$

where $\alpha_\nu$ and $\beta_\nu$ are the ionization and recombination coefficients and $\dot{n}_\nu$ is the photoionization rate due to absorption of radiation emitted by the plasma channel.

The coefficients for ground state ionization and recombination are given by (Zel'dovich and Raizer, 1967);

$$\alpha_\nu = 3.95.10^{23} T_e E_\infty^2 \sigma_\nu^o \exp(-E_\infty/T_e) s^{-1} \qquad 5\text{-}31$$

$$\beta_\nu = 6.7.10^{1} \frac{g_1}{g_+} \frac{E_\infty^2}{T_e^{\frac{1}{2}}} \sigma_\nu^o \quad s^{-1}.cm^3 \qquad 5\text{-}32$$

where $E_\infty$ is the ionization energy in eV, $g_1$ and $g_+$ are the statistical weights of the neutral and ionized states, $T_e$ is the electron temperature in eV and $\sigma_\nu^o$ is the photoionization cross-section. For hydrogen:

$$\sigma_\nu^o \approx 2.0.10^{-14} E_\nu^{-3} \quad cm^2 \qquad 5\text{-}33$$

where $E_\nu$ is the energy of the photon in eV ($E_\nu \geq 13.6.eV$). By approximating $\sigma_\nu^o$ for its value at the ionization threshold, neglecting molecular ionization and with $T_e$=0.35eV:

$$\frac{dn_e^n}{dt} = 2.9.10^{-9} n_H - 3.3.10^{-13} n_H^+ n_e^n + \dot{n}_\nu \qquad 5\text{-}34$$

With $n_H$=1.9.10$^{19}$cm$^{-3}$ and assuming $n_H^+ \approx n_e^n$, Eq. 5-34 gives:

$$\frac{dn_e^n}{dt} = 5.5.10^{10} - 3.3.10^{-13} (n_e^n)^2 + \dot{n}_\nu \qquad 5\text{-}35$$

For plasma temperatures of the order of the Bennett temperature (§5.4.4), it can be shown that $\dot{n}_\nu \ll 5.5.10^{16}$, thus in ionization equilibrium Eq.5-35 gives $n_e \approx 4.0.10^{11} cm^{-3}$. This value is in good agreement with

$n_e = 5.5.10^{11} cm^{-3}$ estimated with the Saha relation (§5.4. ).

A rough estimate of $\dot{n}_\nu$ can be obtained as follows:

i) photoionization is assumed to take place from the ground state of hydrogen atoms, so the minimum photon energy required is $E_{\nu_o} = 13.6eV$.

ii) for a photon to ionize a hydrogen atom the photoionization absorption length of the photon has to be less than the thickness of the high density neutral layer. This condition defines an upper photon energy limit, $E_{\nu_m}$.

iii) $\dot{n}_\nu$ is determined from the total power absorbed by photoionization $W_p$:

$$\dot{n}_\nu = \frac{W_p}{E_{\nu_o} \cdot V_n} \qquad 5\text{-}36$$

where $V_n$ is the volume of the high density neutral layer.

iv) $W_p$ is calculated from bremsstrahlung emission with photons in the energy range $E_{\nu_o} \leqslant E_\nu \leqslant E_{\nu_m}$.

The mean free path for photoionization $\ell_i$ is given by

$$\ell_i = \frac{1}{\sigma_\nu^o \cdot n_H} \qquad 5.37$$

Taking the mean free path to be equal to the thickness of the high density neutral layer $\delta$ and using Eq.5-33 for $\sigma_\nu^o$ , the photon energy range for photoionization is given by:

$$E_{\nu_o} = 13.6\text{eV}$$

$$E_{\nu_m} = (2.0.10^{-14}.n_H.\delta)^{1/3}\text{eV}$$

The power $U(E_\nu)$ radiated by bremsstrahlung emission per unit energy is given by:

$$U(E_\nu)dE_\nu = 3.9.10^{-28}.v_p.\bar{n}_e^{-2}.T_e^{\frac{1}{2}} \exp(-E_\nu/T_e)dE_\nu \qquad 5\text{-}38$$

where $v_p$ is the plasma volume, $T_e$ is the plsma temperature in eV and $\bar{n}_e$ is the mean electron density in the plasma channel. $W_T$ is therefore given by:

$$W_T = \int_{E\nu_o}^{E_{\nu_m}} U(E_\nu)dE_\nu \qquad 5\text{-}39$$

The neutrals and plasma volume are given by:

$$v_n = 2\pi r_p.\delta.\ell \qquad 5\text{-}40$$

$$v_p = \pi r_p^2.\ell \qquad 5\text{-}41.$$

Combining Eqs.5-38 to 5-41 with Eq.5-36, $\dot{n}_\nu$ is given by:

$$\dot{n}_\nu = 1.95.10^{-28} \frac{r_p}{\delta E_{\nu_o}} . \bar{n}_e^2 . T_e^{-\frac{1}{2}} \int_{E_{\nu_o}}^{E_{\nu_m}} \exp(-E_\nu / T_e) dE_\nu \qquad 5\text{-}42$$

With $\bar{n}_H = 1.9.10^{19} cm^{-3}$ and $\delta = 0.02cm$, an upper energy limit $E_{\nu_m} \simeq 20eV$ is estimated. Taking $r_p = 0.07cm$, $\bar{n}_e = 2.10^{18} cm^{-3}$ and with temperatures in the range $T_e = 20\text{-}40eV$ (§5.4.4), $\dot{n}_\nu$ is estimated to be around $10^9 cm^{-3}.s^{-1}$, which is nearly two orders of magnitude less than the leading photoionization term in Eq.5-35.

The electron density in the high density neutral layer is not zero, so finite resistivity might cause a fraction of the current to flow in the neutral region. The ratio of plasma resistance to the resistance of the neutral layer is given by:

$$\phi = \frac{2\delta}{r_p} . \frac{\eta_p}{\eta_n} \qquad 5\text{-}43$$

where $\eta_p$ and $\eta_n$ are the plasma and neutral region resistivity. Using Spitzer transverse resistivity for a fully ionized plasma in the channel and transverse resistivity due to electron-neutral collisions in the high

density neutral layer, Eq.5-43 is written as:

$$\phi = \frac{2.\delta}{r_p} \cdot \frac{6.9.10^{-14}}{T_e^{n\,1/2}\, T_e^{3/2}} \cdot \frac{\ell n\ \Lambda}{\sigma_{oe}} \cdot \frac{n_e^n}{n_n} \qquad 5\text{-}44$$

where $T_e^n$ and $T_e$ are the electron temperature in the neutral and plasma region in eV, $\ell n\ \Lambda$ is the Coulomb logarithm and $\sigma_{oe}$ is the electron-neutral collision cross-section typically $5.10^{-15}cm^2$. For temperatures in the range 20-40eV, the resistance ratio is estimated $\phi \approx 5.10^{-9}$, thus indicating that the fraction of the current flowing in the high density neutral layer is negligible.

### 5.4.4. The Bennett temperature

In radial equilibrium the Bennett relation can be used to estimate the electron temperature. This is given by:

$$T_B = 1.5\ 6.10^{11}\ \frac{I^2}{N_e}\ eV \qquad 5\text{-}45$$

where I is the pinch current in Amperes and $N_e$ is the electron line density in $m^{-1}$. The estimated Bennett temperature at different times during the equilibrium phase at 0.33 and 1.00Atm is shown in Table 5-5. The value at 40ns, which corresponds to the duration of the equilibrium, is an extrapolation based on a two-fold increase in the electron line density each 15ns. For $T_e$<50eV the electron-ion energy equipartition time is about 5ns, thus the assumption $T_e=T_i$ in the Bennett relation is reasonably satisified.

Table 5-5

The Bennett temperature during the equilibrium

pressure: 0.33Atm

| t(ns) | I(kA) | $N_e(10^{18}m^{-1})$ | $T_B$(eV) |
|---|---|---|---|
| 6 | 7.5 | 1.8 | 4.9 |
| 10 | 10.0 | 2.0 | 8.0 |
| 15 | 13.5 | 2.1 | 12.6 |
| 20 | 17.5 | 2.4 | 19.7 |
| 25 | 23.5 | 3.9 | 22.1 |
| 40 | 32.0 | 5.5 | 29.0 |

pressure: 1.00Atm

| t(ns) | I(kA) | $N_e(10^{18}m^{-1})$ | $T_B$(eV) |
|---|---|---|---|
| 5 | 8.0 | 2.0 | 5.0 |
| 15 | 17.5 | 2.9 | 16.5 |

## 5.4.5. The current distribution

The Bennett temperature can be used to estimate the current skin depth. For a cylindrical plasma with a transient current, the skin depth $\delta$ is given by (Haines, 1978):

$$\delta^2 = \frac{\eta \tau \gamma_1^2}{\mu_o} \qquad 5\text{-}46$$

where $\eta$ is the plasma resistivity, $\tau$ is the current growth time and $\gamma_1 = 3.83$ is a geometrical factor. $\tau$ is given by:

$$\tau = \frac{I}{\dot{I}} \qquad 5\text{-}47$$

where $\dot{I}$ is the rate of rise of current.

Using Spitzer transverse resistivity, Eq.5-46 can be written as:

$$\delta^2 = \frac{1.2.10^3 \ \ell n \ \Lambda . I/\dot{I}}{T_e^{3/2}} \ m^2 \qquad 5\text{-}48$$

where $T_e$ is the electron temperature in eV, I is the current in Amperes and $\dot{I}$ is in $A.s^{-1}$. Calculated values of the skin depth during the equilibrium phase at 0.33 Atm and assuming $T_e = T_B$ are shown in Table 5-6. The skin depth is found to be greater than the pinch radius at all times during this phase, thus indicating a diffuse current profile.

Table 5-6

Current skin depth

| t(ns) | $r_p$(mm) | δ(mm) |
|---|---|---|
| 6 | 0.71 | 2.1 |
| 15 | 0.71 | 1.4 |
| 25 | 0.73 | 1.3 |

Pressure: 0.33Atm

## 5.4.6. The electron line density

If the temperature in the plasma channel at the beginning of the equilibrium phase at 0.33Atm is taken to be $T_e$=8eV, the Saha relation, Eq.5-20, with $n_e=1.10^{18}cm^{-3}$ gives a neutral density in the plasma channel $N_n^P \simeq 4.0.10^{13}cm^{-3}$, thus the observed increase in plasma line density can not be explained by further ionization. A possible process for this increase is the diffusion of neutrals into the plasma channel.

The flux of neutrals diffusing across the plasma-neutrals interface is given by:

$$\Gamma = D.\nabla n_n \qquad 5\text{-}49$$

where D is the gas kinetic diffusion coefficient and $n_n$ the

density of neutrals. The self-diffusion coefficient is given by:

$$D = \frac{3\pi}{16\sqrt{2}} \cdot \frac{\bar{v}}{\sigma n_n} \qquad 5\text{-}50$$

where $\bar{v}$ is the mean atomic or molecular speed and $\sigma$ is the atomic or molecular collision cross-section. In the hard sphere approximation:

$$\sigma_H = 8.8.10^{-17} cm^{-2}$$

$$\sigma_{H_2} = 1.6.10^{-16} cm^{-2}$$

Taking into account diffusion of neutral atoms and molecules and assuming that they are ionized when entering the plasma region, the rate of increase of the electron line density in the plasma channel is given by:

$$\frac{dN_e}{dt} = \frac{2\pi r}{n_n} (4.7.10^{19}.\bar{v}_H.\nabla n_H + 2{\cdot}6.0.10^{19}.\bar{v}_{H_2}.\nabla n_{H_2}) m^{-1}.s^{-1} \qquad 5\text{-}52$$

A mean rate of increase in the electron line density due to the diffusion of neutrals can be estimated using the observed values of the neutral density gradients and the estimated temperature in the high density neutral layer (§5.3.4.). Calculated and observed values of $dN_e/dt$ are shown in Table 5-7.

Table 5-7

Mean rate of increase of the electron line density

| Pressure (Atm) | $dN_e/dt(cm^{-1}.s^{-1})$ (measured) | $dN_e/dt(cm^{-1}.s^{-1})$ (calculated) |
|---|---|---|
| 0.33 | $(7\pm0.25).10^{23}$ | $(3.0\pm1.5)10^{23}$ |
| 1.00 | $(1.0\pm0.25).10^{24}$ | $(4.2\pm1.5)10^{23}$ |

The calculated values are within a factor of two of the observed rates. This indicates that diffusion of neutrals is a major process in the increase of the plasma line density.

## 5.4.7. Plasma stability during the equilibrium phase

The characteristic growth time for an m=1 M.H.D. instability is the radial Alfven transit time (Tayler, 1957). Calculated values of the Alfven transit time $\tau_A$ at 0.33 and 1.00Atm and the corresponding observed stability times $\tau_{Ob}$ are given in Table 5-8. These values show that there is an enhancement of the duration of the pinch stability of as much as five.

Table 5-8

Stability times

| Pressure (Atm) | $\tau_{Ob}$(ns) | $\tau_A$(ns) | $\tau_{Ob}/\tau_A$ |
|---|---|---|---|
| 0.33 | 40 | 7.5 | ~5 |
| 1.00 | 15 | 9.0 | ~2 |

$\tau_{ob}$ : observed stability time

$\tau_A$ : Alfven transit time

This enhanced stability cannot be explained by finite Larmor radius effect. In radial equilibrium, the ratio of the ion Larmor radius $r_i$ to the pinch radius $r_p$ in a hydrogen plasma, according to the Bennett relation (§1.1.4.) is given by:

$$\frac{r_i}{r_p} = 5.7.10^8.N_e^{-1/2} \qquad 5\text{-}53$$

For the observed $N_e \sim 2\text{-}4.10^{18} m^{-1}$, the ratio is estimated $r_i/r_p \sim 0.3\text{-}0.4$. For FLR effects to be expected, the plasma has to be magnetized, i.e., $\Omega_i \tau_{ii} >> 1$, where $\Omega_i$ is the ion-cyclotron frequency and $\tau_{ii}$ is the ion collision frequency. For temperatures in the range 20-40eV, $\Omega_i \tau_{ii}$ is estimated to be between 0.05 and 0.25, so the condition is not satisified.

Stabilization due to the neutral gas blanket is not expected expected according to Eq.1-29. The thickness of the high density neutral layer is less than the pinch radius and $(\rho_p/\rho_g)^{\frac{1}{2}} \approx 0.6$ for the background gas, giving a stability enhancement of less than a factor of two.

In a dynamic situation with the current increasing, the instability growth rate changes in timee. It has been suggested by Haines (1985) that the MHD growth rate is modified by the heating rate. The heating rate is given by:

$$\gamma_H = \frac{J^2}{\sigma n_e k T_e} \qquad 5\text{-}54$$

where J is the current density and $\sigma$ is the plasma conductivity. The instability growth rate can be approximated to:

$$\gamma_{MHD} \approx \frac{V_A}{r_p} \qquad 5\text{-}55$$

Using the Bennett relation, the ratio of the heating rate to the instability growth rate for a pinch in radial equilibrium is given by:

$$\frac{\gamma_H}{\gamma_{MHD}} = \frac{0.4}{T_e^2 . r_p} \qquad 5\text{-}56$$

where $T_e$ is the plasma temperature in eV, $r_p$ is in metres and

Spitzer conductivity with $\ell n\ \Lambda = 6$ has been used. For $\gamma_H/\gamma_{MHD}<1$ the pinch is heated at a faster rate than the instability growth rate. When $\gamma_H/\gamma_{MHD}>1$, the pinch is expected to go MHD unstable. According to Eq.5-56, the condition $\gamma_H/\gamma_{MHD}=1$ is given by:

$$T_e = \left( \frac{0.4}{r_p} \right)^{\frac{1}{2}} eV \qquad 5\text{-}57$$

At 0.33Atm and for a typical pinch radius $r_p=7.10^{-4}m$, Eq.5-57 indicates that the instability growth rate becomes faster than the heating rate if $T_e \approx 24eV$. This temperature is similar to the estimated 29eV Bennett temperature at the end of the equilibrium phase. At 1.00Atm the typical pinch radius is $r_p=6.10^{-4}m$, giving a transition temperature $T_e \approx 26eV$. This is higher than the Bennett temperature at the end of the equilibrium, which is estimated around 16eV.

The fact that at the lower pressure the pinch is observed to be more stable, appears to be in contradiction with the theoretical prediction of higher instability growth rate. Both, the MHD growth rate and the MHD growth rate modified by heating rate predict a more stable pinch at the higher pressure. No explanation has been found for this observation.

## 5.5. The Temperature Measurement

The electron temperature inferred from the soft X-ray observations is about 2.5 times the maximum Bennet temperature. The measurement is time integrated over the duration of the pinch but because the emission from the plasma strongly depends on the temperature, the result is indicative of the highest temperature reached by the plasma. The observation of structures superimposed on the plasma column in the X-ray pin-hole photographs (see Fig.4-26) suggest that the highest temperature occurs at the time when the instability develops. This increase in temperature could be due to anomalous resistivity associated with the development of the MHD instability (Tidman, 1971). The uncertainties in the temperature measurement preclude any further analysis of this hypothesis.

The Bennett relation assumes a uniform temperature profile. For the temperature to be uniform over the pinch section in a pinch with diffuse current, the characteristic time for radial thermal diffusion has to be much shorter than the magnetic field diffusion time. The radial thermal diffusion time $\tau_{diff}$ is given by (Haines, 1978):

$$\tau_{diff} = \frac{3\, n\, r_p^2}{\gamma_1^2 \kappa_{\perp a}} \qquad 5\text{-}57$$

where $n=n_i=n_e$ is assumed and $\kappa_{\perp a}$ is the relevant radial heat transport coefficient across the magnetic field. The magnetic field diffusion time is given by (Haines, 1978):

$$\tau_B = \frac{\mu_o \sigma r_p^2}{\gamma_1^2} \qquad 5\text{-}58$$

Eqs.5-57 and 5-58 can be combined to give:

$$\frac{\tau_{diff}}{\tau_B} = 2.4.10^2 \frac{n \ln \Lambda}{T_e^{3/2} \kappa_{\perp a}} \qquad 5\text{-}59$$

where $T_e$ is in eV and Spitzer transverse conductivity has been used.

A calculation using Braginskii's transport coefficients published by Laing (1981) indicates that for plasma parameters corresponding to the equilibrium phase at 0.33Atm, $\kappa_{\perp e} > \kappa_{\perp i}$, thus radial electron thermal conduction dominates. Calculated values of $\kappa_{\perp e}$, $\kappa_{\perp i}$ and $\tau_{diff}/\tau_B$ at different times during the equilibrium are shown in Table 5-9.

$$\gamma_{s.w.} = k.V_A.K_o^{\frac{1}{2}} (k.r_p) \qquad 5\text{-}60$$

where $V_A$ is the Alfven velocity and $K_o$ is the Bessel function of order zero. The growth rate given by Eq.5-60 is found to be maximum for $k.r_p \simeq 1.57$. This value is similar to the observed values of $k.r_p$ shown in Table 4-3 (§4.5).

Measured and calculated values of the instability growth rate are shown in Table 5-10. Calculated growth rates show good agreement with observed values.

m=1 MHD modes with $k.r_p < 1$, which according to Manheimer et al (1973) are more likely to develop, are not observed.

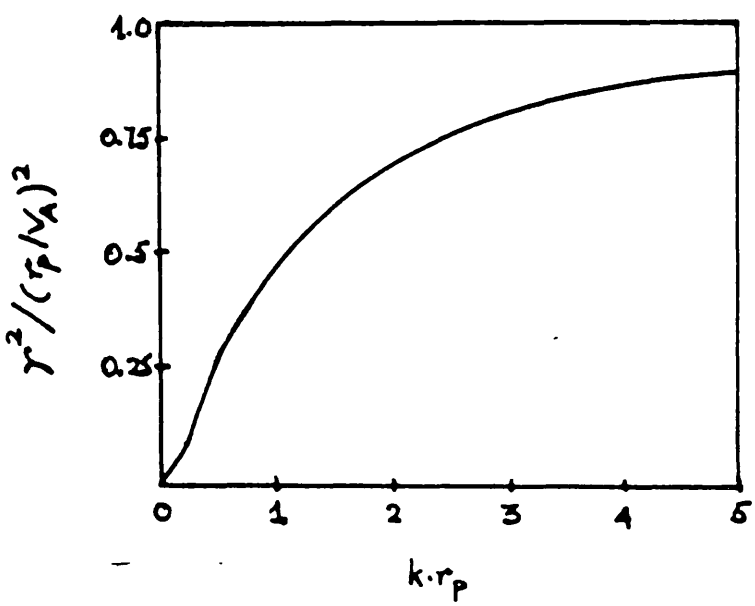


Fig. 5.4: Growth rate for the m=1 MHD instability calculated by Tayler (1957).

Table 5-9

Calculated ratio of $\tau_{diff}$ to $\tau_B$

| time(ns) | $\kappa_{\perp\ e}(m^{-1}.s^{-1})$ | $\kappa_{\perp\ i}(m^{-1}.s^{-1})$ | $\tau_{diff}/\tau_B$ |
|---|---|---|---|
| 6 | $1.9.10^{24}$ | $8.0.10^{22}$ | 74.1 |
| 15 | $8.0.10^{24}$ | $7.7.10^{23}$ | 5.4 |
| 25 | $1.3.10^{25}$ | $2.9.10^{24}$ | 2.7 |

The calculation indicates that radial heat diffusion occurs at a slower rate than curent diffusion, therefore the possibility of a non-uniform temperature profile exists.

## 5.6. The Unstable Phase

The measured growth rate of the instability can be compared with a theoretical prediction for an m=1 MHD mode by Tayler (1957). The growth rate, $\gamma$, calculated by Tayler is plotted as a function of $k.r_p$ in Fig.5-4. The theory by Tayler predicts that the fast growing mode corresponds to $k.r_p=\infty$ (or $\lambda=0$). Felber and Rostoker (1981) have calculated growth rates for kink instabilities in imploding wire arrays. They assume flexible constant radius wires which move under the influence of the magnetic field generated by their own current and the curent in the other wires of the array. The growth rate for a single wire is found to be:

Table 5-10

Instability grow rates

| Pressure (Atm) | $\kappa.r_p$ | $\gamma_{ob}$ ($10\ s^{-1}$) | $\gamma_{MHD}$ ($10^8 s^{-1}$) | $\gamma_{sw}$ ($10^8 s^{-1}$) |
|---|---|---|---|---|
| 0.33 | 1.7 (1) | 0.73 | 1.25 | 0.97 |
| 0.33 | 1.64 (2) | | 1.22 | 0.97 |
| 1.00 | 1.67 (2) | 0.83 | 0.96 | 0.91 |
| 1.00 | 4.16 (3) | | 1.01 | 0.53 |

$\gamma_{ob}$ : observed growth rate

$\gamma_{MHD}$ : m=1 MHD growth rate (Tayler, 1957)

$\gamma_{sw}$ : m=1 kink growth rate in single wire (Felber and Rostoker, 1981)

Pinch radius measurement: interferometry

Wavelength measurement: (1) Framming

(2) Schlieren

(3) Interferometry

## 5.6.1. The helical pinch

The transformation of the cylindrical pinch into a helix has been observed in all gas-embedded Z-pinch

experiments (§1.5.4.). The absence of the m=0 MHD instability has not been explained. The possibility that the helix is due to relaxation to a lower energy configuration is currently under investigation (Coppins, 1985).

The change from a cylindrical to a helical pinch involves a change in inductance.

The voltage across the end of the transmission line is given by:

$$V = \frac{d}{dt} (L.I) \qquad 5\text{-}61$$

where L is the pinch inductance plus the inductance associated with the pinch assembly.. From Eq.5-61

$$V = L\dot{I}.(1+ \frac{I}{\dot{I}} . \frac{\dot{L}}{L} ) \qquad 5\text{-}62$$

At the time when the instability develops, $I \simeq 30kA$, $\dot{I} \simeq 7.10^{11} A.s^{-1}$ (conditions for 0.33 Atm). Replacing these values in Eq.5-62 gives:

$$V = L.\dot{I} \ (1+4.3.10^{-8} \frac{\dot{L}}{L} ) \qquad 5\text{-}63$$

For the helical instability to be detected in the voltage waveform, $\frac{\dot{L}}{L} \geq 4.3.10^{-8}s^{-1}$ is required. No significant change in the voltage waveform has been observed at the time when the instability develops. This might indicate that L is below the value specified by Eq.5-63. Unfortunately no analytic approximation of the inductance of a helix is available in order to compare with the experiment.

A further possible explanation for the non-observation of a change in the voltage at the time of the transition to a helix relies on flux conservation. The voltage across the end of the line is also given by:

$$V = \frac{d\Phi}{dt} \qquad 5\text{-}64$$

when $\Phi$ is the magnetic flux inside the pinch chamber. If a re-arrangement of the curent path conserves flux, no change is to be expected in the voltage waveform.

Relaxation to a lower magnetic energy configuration could result in plasma heating by absorption of the extra energy in the magnetic field. This mechanism provides a further possible explanation to the higher temperature observed at the time of the transition to the helical configuration.

# CHAPTER VI

# Conclusion

## 6.1. Introduction

This chapter begins with a review of the main results obtained in this investigation. A discussion of the shortcomings of the present experiment is presented. Future work in the gas-embedded Z-pinch is considered: this is the use of extra diagnostics to characterize the pinch more fully and new experiments to further assess the potential of the high density Z-pinch as a thermonuclear fusion device.

## 6.2. Review of Experimental Results

A laser initiated, 0.7mm radius, preheated plasma filament is Joule heated in radial equilibrium for 30 to 40ns. This time is about five times the Alfven radial transit time. Typical electron density for a pinch in 0.33Atm hydrogen is of the order of $10^{18}cm^{-3}$. Based on the Bennett relation the temperature at the end of the equilibrium phase is estimated to be about 30eV. To preheat the plasma channel a current of peak 5kA is applied for 60 to 80ns, which is followed by a 50kA, 100ns main current pulse.

During preheat the plasma channel expands continuously with supersonic velocity. The electron density profile changes from a hollow to a flat distribution and a high density neutral layer builds up at the plasma boundary.

During the equilibrium phase the electron density profile changes to a distribution which is peaked on axis. The electron line density is found to grow continuously with an e-folding time of ~20ns. The mean rate of increase of the electron line density is found to agree within a factor of two with the calculated rate of diffusion of neutrals into the plasma channel.

An instability develops and the plasma column is transformed into an expanding helical structure. The observed growth rate of the instability is in good agreement with MHD calculations. The instability is observed to start inside the plasma channel and is characterized by a sinusoidal perturbation of the number density around the pinch axis. A peak electron temperature of around 70eV is inferred from soft X-ray observations, which is estimated to correspond to the time when the instability develops.

The observation of a constant radius pinch and the existence of a high density neutral layer at the pinch boundary have not been reported in previous gas-embedded Z-pinch investigations.

The measurements of the plasma density are direct and the increase in plasma line density has been determined unambiguously.

The observation of the early stages in the development of the instability as an internal perturbation of the electron density distribution is an important new result which provides an experimental base for theoretical studies of the stability of a high density Z-pinch.

## 6.3. Shortcomings of the Present Work

This experiment is certainly not complete.

To investigate further the relation between preheat and the establishment of radial equilibrium a better diagnostic of the preheating discharge is required. This involves a measurement of the electron temperature. For temperatures of the order of 100 eV optical spectroscopy of hydrogen lines (McWhirter, 1965) can be applied. When an independent measurement of the electron density is available, the electron temperature can be estimated from the relative intensity of lines belonging to successive ionization stages of impurity ions (Griem, 1964). The OV (2781Å) and OVI (3811Å) lines were used by Smars (1964) to estimate a temperature of 14eV in a gas-embedded pinch.

Time and space resolved measurements of the electron temperature during the equilibrium phase are essential for a better understanding of the plasma dynamics. In a Z-pinch in radial equilibrium with diffuse current, the plasma dynamics can be described by the following equations:

$$J(r) = \alpha E_o T^{3/2}(r) \qquad 6\text{-}1$$

$$\frac{1}{r} \cdot \frac{d}{dr} (rB(r)) = \mu_o J(r) \qquad 6\text{-}2$$

$$\nabla(2n(r)kT(r)) = -J(r).B(r) \qquad 6\text{-}3$$

where $J(r)$ is the current density, $E_o$ the uniform axial electric field and $B(r)$ the azimuthal magnetic field. Eq.6-3 assumes $n_e(r) = n_i(r) = n(r)$ and $T_e(r) = T_i(r) = T(r)$. Eqs. 6-1 to 6-3 can be combined to give:

$$\frac{d\theta(x)}{dx} = - \frac{\theta x}{N(x)} \left\{ \frac{dN(x)}{dx} + \beta \frac{\theta^{1/2}(x)}{dx} \int_o^x x'\theta^{3/2}(x')dx' \right\} \qquad 6\text{-}4$$

where:

$$x = \frac{r}{r_o} \; ; \; \theta(x) = \frac{T(r)}{T_o} \; ; \; N(x) = \frac{K(r)}{n_o}$$

$$\beta = \frac{\mu_o \alpha^2 E_o^2 T_o^2 r_o^2}{2 n_o k}$$

If the electron density distribution is known $n_o$ can be taken to be the electron density on axis and $r_o$ the pinch radius. If the pinch current has been measured, a measurement of the axial electric field or the temperature on axis allows Eq.6-4 to be solved numerically to obtain the temperature distribution. This is possible because the integral of Eq.6-1 over the pinch section is the total pinch current, which is a constraint on the solutions of Eq.6-4 obtained with different values of $\beta$. The integral of Eq.6-1 over the pinch section gives:

$$I = 2\pi r_o^2 \alpha E_o T_o^{3/2} \cdot \int_o^1 x \, \theta^{3/2}(x) dx \qquad 6\text{-}5$$

When the electron density and temperature distributions are known, the equilibrium pressure profile is determined. This information can be used to assess the MHD instability of the pinch. A shooting Code (Coppins, 1984) is available to investigate the stability of a Z-pinch to the m=O MHD instability.

Time resolved measurements of the electron temperature in the range 20-50eV are difficult to perform due to the low

photon flux available in the visible spectrum. This problem can be overcome by using U.V. spectroscopy of line radiation from impurity ions (Griem, 1964; De Michelis and Mattioli, 1981). These measurements were not attempted because the required equipment was unavailable.

The transformation of the pinch into a helix is expected to be associated with a redistribution of the current into a helical path. This involves the appearance of an axial magnetic field. Several probes were designed to attempt a measurement of the axial magnetic field but due to the large azimuthal magnetic field and electromagnetic interference, no conclusive results were obtained.

Radial equilibrium and constant plasma line density are basic requirements of an ohmically heated Z-pinch of thermonuclear interest. The observation of a constant radius phase with a stability time longer than the MHD prediction in a regime where enhanced stability is not expected is an encouraging result.

The Bennett relation indicates that a high electron line density might preclude the establishment of thermonuclear temperatures by requiring an extremely high current, which is not consistent with the Pease-Braginskii limit (§1.3). The observation of an increasing line density identifies a potential problem in this context. The rate of

increase in line density measured in this experiment is about one third of the value reported by Schlachter (1982), for a gas-embedded Z-pinch in continuous radial expansion. These measurements do not account for high density neutrals at the pinch boundary.

The stability of the pinch is found to be determined by MHD considerations. If the instability growth rate is modified by the Ohmic heating rate, the pinch is expected to go unstable at temperatures below 100eV for any realistic value of the pinch radius (see Eq.5-57).

FLR effects are expected to enhance pinch stability. In the FLR regime the conditions $r_i/r_p \ll 1$ and $\Omega_i \tau_{ii} \gg 1$ have to be satisfied. In the experiment $r_i/r_p$=0.3-04 and $\Omega_i \tau_{ii}$=0.05-0.25, so the condition on $\Omega_i \tau_{ii}$ is not satisfield.

In a Z-pinch in radial equilibrium, $\Omega_i \tau_{ii}$ is given by:

$$\Omega_i \tau_{ii} = 3.9.10^{31} \frac{r_p I^4}{\ell n\ \Lambda \cdot N_e^{5/2}} \qquad 6\text{-}6$$

Eq.6-6 has been used to calculate the pinch current which is required to achieve $\Omega_i \tau_{ii} \geq 1$ for different electron line densities and pinch radii. Results for $r_i/r_p$ = 0.4 and $r_i/r_p$ = 0.57 are shown in Fig.6-1. The figure indicates

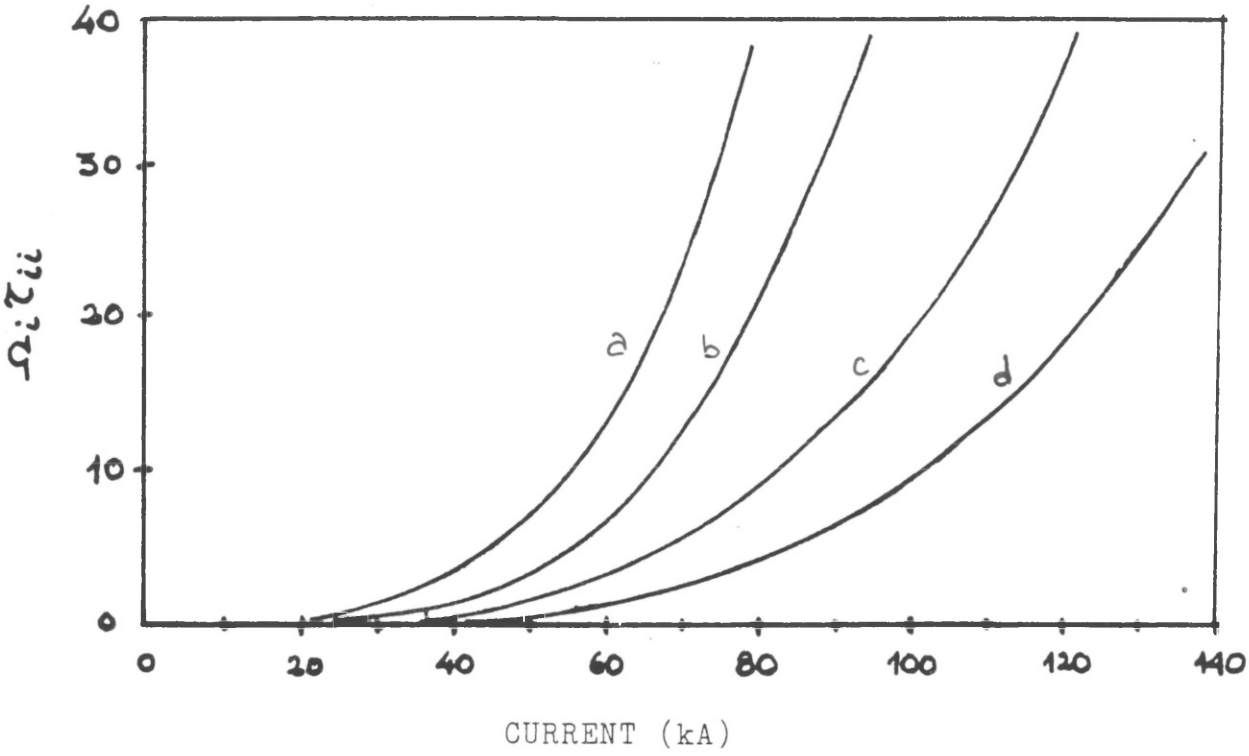


Fig. 6.1: $\Omega_i \cdot \tau_{ii}$ for a constant radius pinch. (a) $N_e = 2.10^{18}$m, $r_p = 10^{-3}$m, (b) $N_e = 2.10^{18}$m, $r_p = 0.5.10^{-3}$m, (c) $N_e = 4.10^{18}$m, $r_p = 10^{-3}$m, (d) $N_e = 4.10^{18}$m, $r_p = 0.5.10^{-3}$m.

Fig. 6.2: Photograph of the new transmission line. Maximun current: 200kA.

that the current required to achievd $\Omega_i \tau_{ii}=10$ is of the order of 60 to 100kA, which is higher than the maximum current delivered by the generator used in these experiments.

## 6.4. Future Work

A thermonuclear Z-pinch has to satisfy the Lawson condition $n\tau_c \approx 10^{20} m^{-3}.s$, when $\tau_c$ is the confinement time. With pinch parameters $I=9.0.10^5 A$, $r_p=2.10^{-5} m$ and $n_e=4.5.10^{27} m^{-3}$, the radial Alfven transit time is estimated to be $\tau_A \approx 10^{-11} s$. For the same electron density the Lawson condition gives $\tau_c \approx 2.10^{-8} s$ or $\tau_c \approx 2{,}000 \tau_A$. It is then clear that for a high density Z-pinch to work as a thermonuclear fusion device plasma stability has to be enhanced far beyond the MHD limit. Testing of FLR effects appears as an obvious step in this direction.

To investigate possible FLR stability a new current generator has been designed and built during the course of these investigations. The current generator is identical to that used in this experiment but at a higher voltage. It consists of an 8-capacitor Marx bank and a two section water dielectric transmission line. Commissioning of the new generator has already been completed. The main characteristics of the generator are:

| | | |
|---|---|---|
| Marx working voltage | : | 600kV |
| Line impedance | : | ~3Ω |
| Current pulse | : | 210kA peak into a ~ 40nH load |
| | | dI/dt ~ $3.10^{12}A.s^{-1}$ |
| | | 10-90% rise time: 50ns |
| | | FWHM: 160ns |
| | | Width at the base: ~275ns. |

A photograph of the new transmission line is shown in Fig.6-2.

At a pinch current of 150kA and with a line density of $3.10^{18}m^{-1}$, the Bennett relation gives a temperature of ~1.2keV in radial equilibrium. Several spectroscopic techniques are available to obtain time resolved measurements of the electron temperature in this regime (Griem, 1964; McWhirter, 1965; De Michelis and Mattioli, 1981).

A better understanding of the observed increase in the electron line density requires an investigation of the plasma-neutral gas interface. Two wavelength holographic interferometry can be used to separate the electron and neutral density distributions, giving an improved description of the interaction region.

As a result of this investigation it appears that the main process responsible for the increase in plasma line density is the diffusion of neutrals into the plasma channel. To avoid the diffused neutrals being ionized, the plasma channel has to be separated from the high density neutral layer. A possible method to produce this separation is to have a fast rising current at the beginning of the main current pulse, such that the preheated plasma column is pinched and a vacuum or cold low density coronal region is formed between the plasma and the high density neutrals. After this initial compression is completed the rate of rise of current has to be programmed to achieved ohmic heating in radial equilibrium. A vacuum or coronal region separating the plasma column from the neutrals can also decrease radial thermal conduction and reduce the heating of the neutrals.

The effect of the neutral blanket on the pinch stability does not seeem to be very important. An alternative approach to the high density Z-pinch, where no neutrals around the pinch are to be expected is the formation of the Z-pinch in a gas jet. This experiment has not been performed.

It has been shown that with laser initiation a well defined pinch is formed in high pressure gas with typical initial diameter 150-200μm. A conceptual Z-pinch of thermonuclear interest requires a smaller diameter (~40μm)

and a high number density ($n_e \sim 10^{27} m^{-3}$). To achieve these plasma parameters further compression of the plasma channel might be required. Two methods have been suggested to compress a preformed plasma column. Adiabatic compression using a programmed slowly rising current has been discussed by Potter (1978). Contraction of a Z-pinch due to radiation collapse has been discussed by Shearer (1976). In contrast with adiabatic compresion radiation collapse requires a large increase in current up to values which are above the Pease-Braginskii limit. This further compression of the pinch to reach the required density and final radius might produce the required separation of the plasma channel from the neutral blanket, in order to keep a constant plasma line density.

## 6.5. Conclusion

The results obtained in this investigation have shown experimentally that it is possible to achieve Joule heating of a high density Z-pinch with constant radius which is stable for a time longer than predicted by MHD theory. This is an important step in assessing the potential of the high density Z-pinch as a thermonuclear fusion device. The experimental results presented in this thesis constitute a basis to develop further experiments along this line.

In the general context of plasma physics the gas-embedded Z-pinch appears as a well established plasma device which is characterized by a high electron density with a temperature below 100eV. This combination of plasma parameters and cylindrical geometry seems to be a suitable configuration for a photolytic laser scheme. (Asmus and Lovberg, 1984).

# APPENDIX A

## Particle Density Calculations

### A.1. Introduction

The method used to calculate the particle density distribution is presented in this appendix. An Abel inversion of the fringe shift is made numerically. The accuracy of the method is discussed.

### A.2. The Abel inversion

A typical fringe shift profile observed in the experiment is shown in Fig.A-1. The fringe shift is related to the pinch coordinates. The fringe shift at a point y in the figure is given by ( 3.3):

$$s(y) = \frac{l}{\lambda} \int_{L(y)} [(\mu-1)_e + (\mu-1)_a - (\mu-1)_o] d\ell \qquad \text{A-1}$$

where $\lambda$ is the wavelength of the probing beam, $(\mu-1)_e$ and $(\mu-1)_a$ are the refractive index due to electrons and neutrals $(\mu-1)_o$ is the refractive index of the background gas and the integration is preferred along the beam path L(y).

According to Eq. 3-6 and 3-7 the refractive indexes at the ruby wavelength are given by:

$$(\mu-1)_e = -2.16.10^{-22} n_e \qquad \text{A-2}$$

$$(\mu-1)_a = 5.085.10^{-24} n_a \qquad \text{A-3}$$

where $n_e$ and $n_a$ are the electron and neutral density. The neutral density in the backgroundd gas is given by:

$$n_o = L.p \qquad \text{A-4}$$

where $L = 2.69.10^{19} cm^{-3}$ is the Loschmidt's number and p is the gas pressure in Atm. Using Eqs. A-3 and A-4, the refractive index of the background gas is given by:

$$(\mu-1)_o = 1.368.10^{-4}.p \qquad \text{A-5}$$

The axial symmetry observed in the interferograms indicates that $n_e$ and $n_a$ depend only on the pinch radius. This axial symmetry can be used to perform an Abel inversion of Eq.A-1 to obtain the electron and neutral density. The method is as follows:

i) The pinch is divided in concentric rings of the same thickness.

ii) The particle density in each ring is asumed to be constant and determined by the fringe shift corresponding to the center of the ring.

iii) The electron and neutral density distributions are assumed not to overlap. This is based on the fact that the fringe shifts at the edge and inside the pinch are observed to have opposite signs and that the fringe shift due to electrons is about 40 times the fringe shift due to neutrals with the same number density.

iv) The calculation starts at the outermost ring with the assumption that the observed fringe shift is due to a high density neutral layer.

v) The calculation continues towards the pinch center up to a point where a negative neutral density is required to account for the observed fringe shift. This point is taken to be the edge of the electron density distribution.

vi) The calculation of the electron density distribution is continued up to the pinch center.

The pinch is divided in M rings. A diagram of the rings is shown in Fig. A-2. The thickness of each ring is given by:

$$\Delta r = \frac{R}{M} \qquad \text{A-6}$$

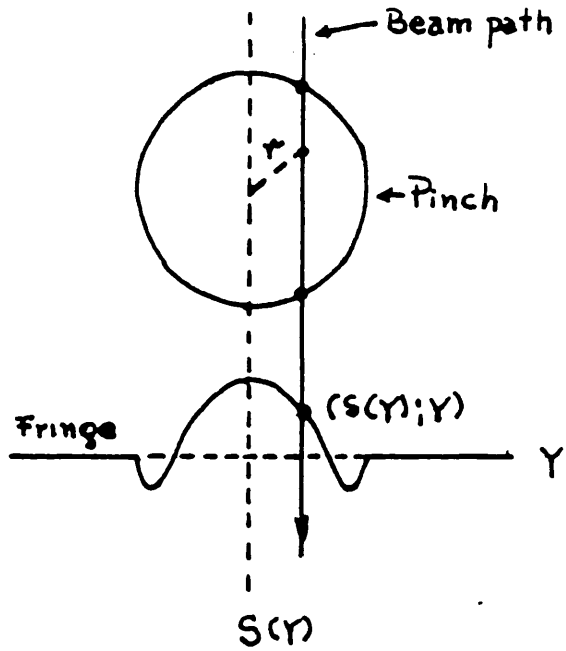


Fig. A-1: Cross-section of the pinch with characteristic fringe shift pattern.

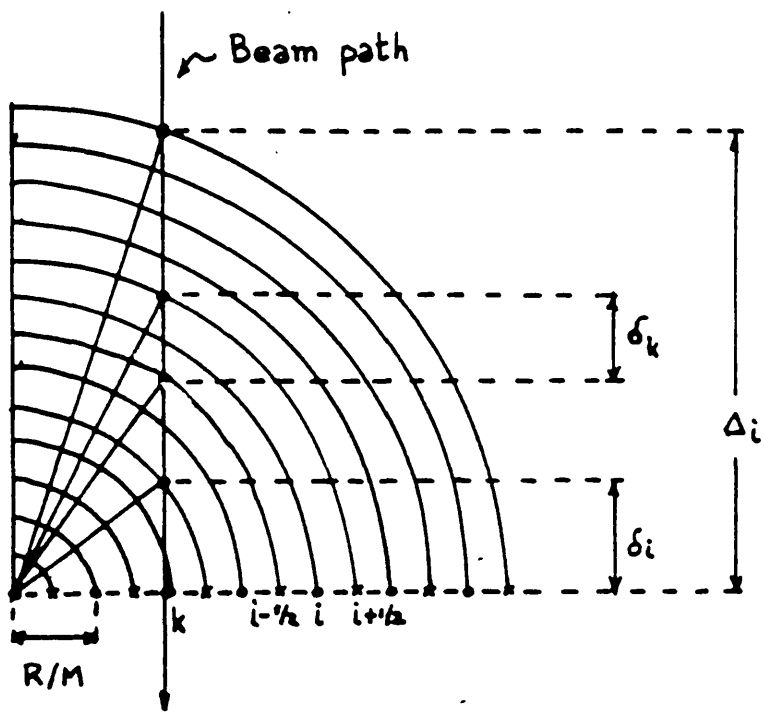


Fig. A-2: Cross-section of the pinch showing the constant particle density rings used in the Abel inversion precess.

where R is the radius of the pinch.

With the approximations introduced by the method, Eq.A-1 can be replaced by:

$$s(y_i) = \frac{2}{\lambda} \left[ \sum_{k=1}^{M} ((\mu(r_k)-1)_e + (\mu(r_k)-1)_a) \cdot \delta_k - (\mu-1)_o \cdot \Delta_i \right] \qquad \text{A-7}$$

where:

$$r_k = \frac{k}{M} \cdot R \qquad \text{A-8}$$

From Fig.A-2, $\delta_k$ is given by:

$$\delta_k = \Delta_r \cdot \{(k^2-(i-\tfrac{1}{2})^2)^{\frac{1}{2}} - ((k-1)^2-(i-\tfrac{1}{2})^2)^{\frac{1}{2}}\} \qquad \text{A-9}$$

if $k < i$,

and

$$\delta_k = \Delta_r \, (k^2 - (i-\tfrac{1}{2})^2)^{\frac{1}{2}} \qquad \text{A-10}$$

if $k = i$

Using Eqs. A-7 and A-10, $\Delta_i$ is given by:

$$\Delta_i = R.\left(1 - \left(\frac{i-\frac{1}{2}}{M}\right)^2\right)^{\frac{1}{2}} \qquad \text{A-11}$$

If q is an integer such as $r_p = q.\Delta r$, where $r_p$ is the radius of the electron density distribution, Eq. A-7 can be written as:

$$S(y_i) = \frac{2}{\lambda}\left[\sum_{k=1}^{q}(\mu(r_k)-1)_e.\delta_k + \sum_{j=q+1}^{M}(\mu(r_j)-1)_e).\delta_j - (\mu-1)_o.\Delta_i\right] \qquad \text{A-12}$$

Using Eqs.A-2, A-3 and A-5 for the refractive indexes, the neutral density at $r_i$ is given by:

$$n_a(r_i) = \frac{1}{\delta_i}\left[6.83.10^{18}\ S(y_i) + 2.69.10^{19}.p.\Delta_i - \sum_{k=i+1}^{M} n_a(r_k).\delta_k\right] \qquad \text{A-13}$$

with $q < k \leq M$.

The electron density at $r_\ell$ is given by:

$$n_e(r_e) = \frac{-1}{\delta_\ell}\left[1.61.10^{17}.S(y_\ell) + 6.33.10^{17}p.\Delta_\ell + \sum_{k=\ell+1}^{q} n_e(r_k).\delta_k - 2.35.10^{-2}\sum_{k=q+1}^{M} n_e(r_k).\delta_k\right] \qquad \text{A-14}$$

with $1 \leq \ell \leq q$.

A computer program was written to solve Eqs.A-13 and A-14 to obtain the electron and neutral density distributions. A digitized fringe shift profile is provided as an input to the program. The fringe shift at the required radial position is obtained by linear interpolation. The number of rings is fixed at M=200.

## A.3. The accuracy of the particle density measurements

The accuracy of the particle density measurements can be affected by three types of erros: i) error in the fringe shift measurement, ii) error introduced by the computation method, and iii) error due to the assumption of non-overlapping electron and neutral particle distributions.

Errors due to the fringe shift measurement have been considered by introducing error bars in the particle density profiles. A calculation of error bars was performed for shot 160310, assuming an accuracy of 1/20th of a fringe in the measurement. The result is presented in Fig.A-3. It is assumed that similar error bars can be associated to all density measurements in the experiment.

To estimate possible error due to the computational method, the number of rings considered in the calculation was increased from M=200 to M=500. Result for both calculations agreed within 1%.

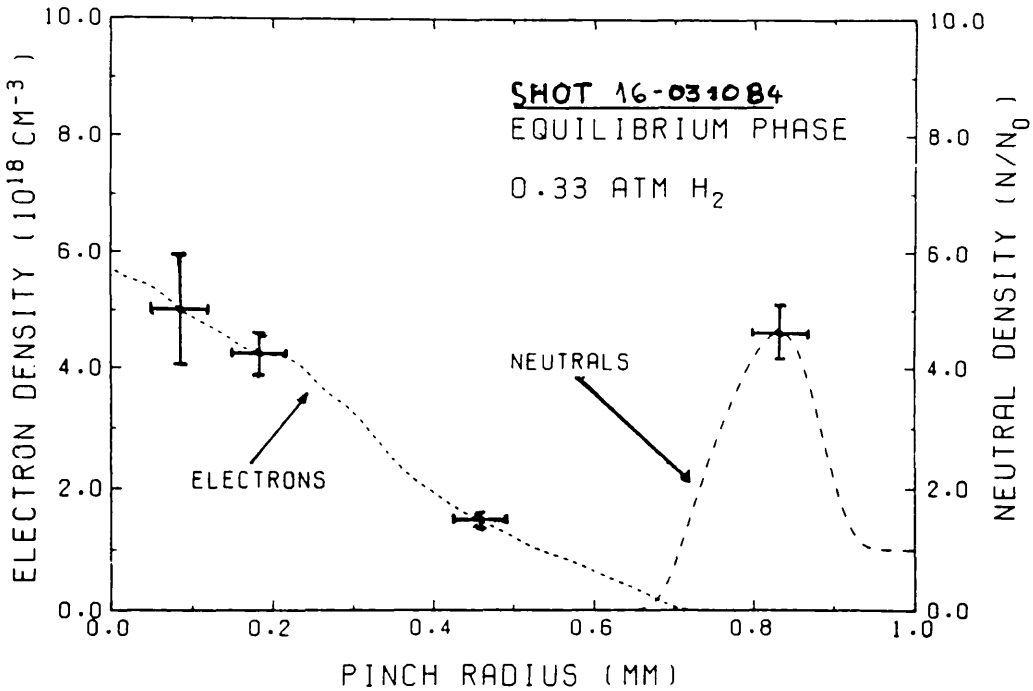


Fig. A-3: Error bars calculated for a typical density profile during the equilibrium phase. An accuracy of 1/20 of a fringe has been assumed.

The following method was used to asses the error introduced by the assumption of non-overlapping distributions:

i) Different particle density profiles with interpenetrating electron and neutral density distributions were assumed.

ii) The fringe shift expected from the different overlapping distributions was calculated.

iii) The resulting fringe shift was used to calculate particle density profiles with the assumption of non-overlapping distributions.

Results are shown in Fig.A-4 for two typical particle density distributions observed in the experiment. Apart from the overlapping region the calculated electron density profiles is almost identical to the asumed profiles. The neutral density can be underestimated if the electron density in the high density neutral layer is of the order of the values assumed in the calculation, i.e. $n_e \approx 2.10^{17} cm^{-3}$. If $n_e \leq 10^{16} cm^{-3}$ in the neutral region, no significant error is expected in the neutral density calculation.

The electron line density is estimated by integrating the electron density distribution over the pinch section.

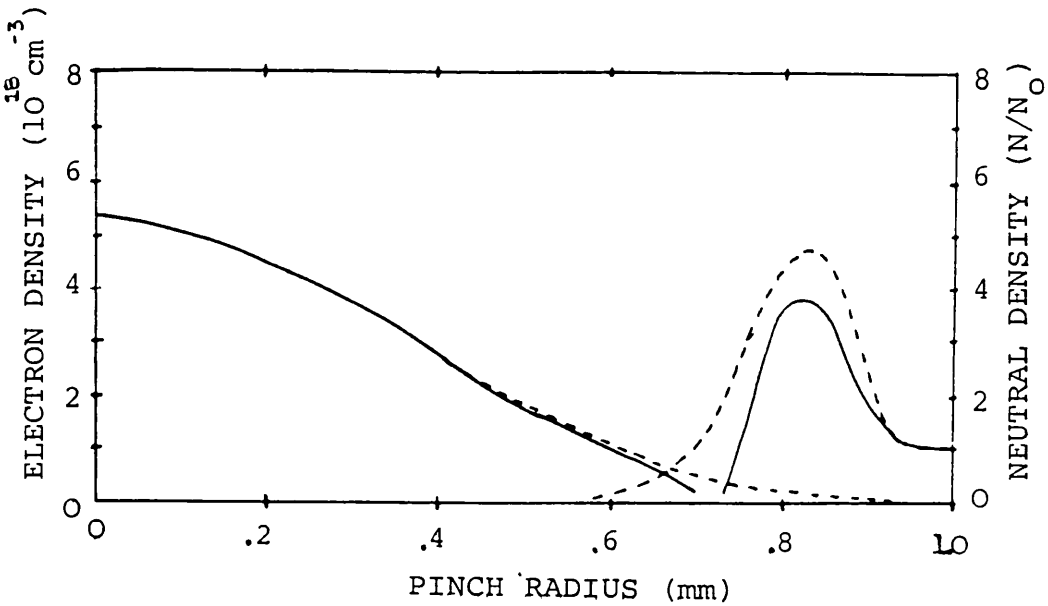


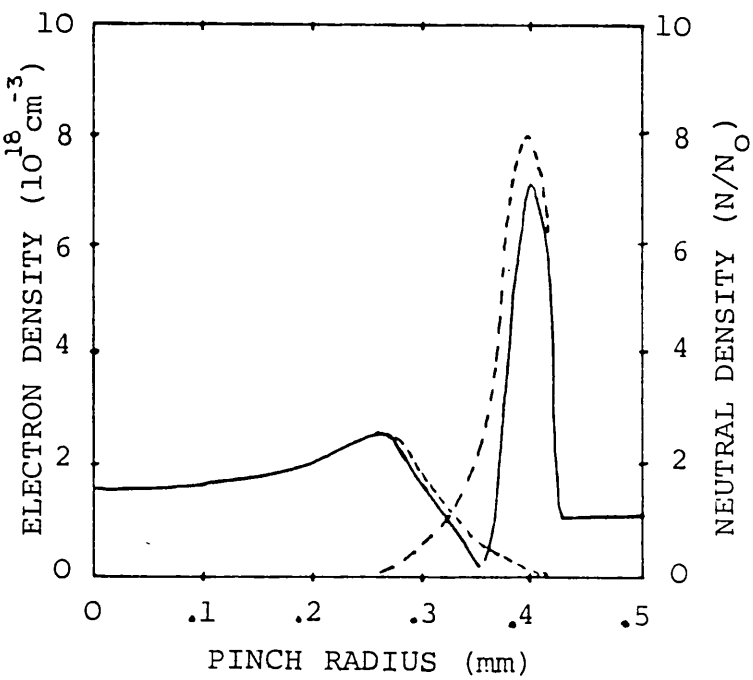


Fig. A-4: Segmented line: given particle density profiles. Full line: particle density distributions calculated from the fringe shift corresponding to the given distributions and with the assumption of non-overlapping electron and neutral density profiles.

The difference between the electron line density resulting from the calculated and original profiles is less than the error bar due to the accuracy in the fringe shift measurement. The neutral line density, which is calculated in the same way as the electron line density can be underestimated by as much as 25% if $n_e \simeq 2.10^{17} cm^{-3}$. If $n_e < 10^{1} m^{-3}$ in the neutral region, the error in the neutral line density is dominated by the accuracy in the fringe shift measurement.

REFERENCES.


Asmus, J. F. and Lovberg, R. H., Univ. of California (San Diego) report, 1984.

Allen, C. W., 'Astrophysical Quantities', 2nd. Edition, Oxford Unversity Press, 1963.

Book, D. L., N. R. L. Plasma Formulary, Naval Research Lab., Washington, 1983.

Bowers, E. A. and Haines, M. G., Phys. Fluids, 14,p.165, 1971.

Braginskii, S. I., Sov. Phys, JEPT, 34, p.1068, 1958.

Brown, D. B. et al., J. Ap. Phys., 47, p.3722, 1976.

Brown, R. et al., J. Phys. B, 16, p.2053, 1983.

Carruthers, R. and Davenport, P. A., Proc. Phys. Soc.B70, p.49,1957.

Coppins, M., Ph. D. Thesis, Univ. of London, 1984.

Coppins, M., Private Communication, 1985.

Decker, G. and Wienecke, R., Physica C82, p.155,1976.

DeMichelis, C. and Mattioli, M., Nucl. Fus. 21, p.677, 1981.

Eddleman, J. L. and Hartmann, C. W., Lawrence Livermore Report UCID-16992, 1976.

Ekdhal, C. A., Rev. Sci. Instrum. 51, p.1645, 1980.

Falthammar, C. G., Phys. Fluids 4, p.1145, 1961.

Felber, F. S. and Rostoker, N., Phys. Fluids 24, p.1049, 1981.

Gray, D. E., A. I. P. Hand Book, 2nd. Edition, 1963.

Greve, P. et al., Phys. Rev. A 24, p.429, 1981.

Griem, H. R., 'Plasma Spectroscopy', McGraw-Hill, 1964.

Hagenson, R. L. et al., Nucl. Fus. 21, p.1351, 1981.

Haines, M. G., Proc. Phys. Soc. 76, p.250, 1960.

Haines, M. G., Proc. Phys. Soc. 77, p.643, 1961.

Haines, M. G., J. Phys. D 11, p.1709, 1978.

Haines, M. G., Phil. Trans. R. Soc. Lon. A300, p.649, 1981.

Haines, M. G., Physica Scripta T2/2, p.380, 1982.

Haines, M. G., Private Communication, 1985.

Hammel, J. E. et al., Nuc. Inst. and Meth. 207, p.161, 1983.

House, L. L., Ap. J. Supp. 7(81), p.307, 1964.

Jones, L. A. et al., Appl. Phys. Lett. 38, p.522, 1981.

Kimura, W. D. et al., Private Communication.

Kolb, A. C. and McWhirter, R. W. P., Phys. Fluids 7,p.519, 1964.

Koppel, L. N., Advances in X-ray Analyses 18, p.146, 1975.

Kruskal, M. and Schwarzchild, M., Proc. Roy. Soc. A223, p.348, 1954.

Laing, E. W., 'Plasma Physics and Nuclear Fusion Research', Ed. by R. D. Gill, Academic Press, 1981.

Lawson, J. D., Proc. Phys. Soc. B70, p.6, 1957.

Marshall, W., 'Kinetic Theory of an Ionized Gas', A. E. R. E., T/R2419, 1958.

McWhirter, R. W. P., 'Plasma Diagnostic Techniques',Ed. by R. H. Huddlestone and S. L. Leonard, Academic Press, 1965.

Meyerott, A. J., Rev. Sci. Inst. 35, p.669, 1964.

Menheimer, W. M. et al., Phys. Fluids 16, p.1126, 1973.

Ostrovsky, Y. I. et al., 'Interferometry by Holography', Springer-Verlag, 1980.

Parfenov, O., Private Communication, 1984.

Pease, R. S., Proc. Phys. Soc. 70, p.11, 1957.

Pechacek, R. E., Bull. Am. Phys. Soc. 17, p.974, 1972.

Post, P. F., Plasma Phys. 3, p.273, 1961.

Potter, D. E., Phys. Fluids 14, p.1911, 1971.

Potter, D. E., Nuc. Fus. 18, p.813, 1978.

Rockett, P., Private Communication, 1985.

Robson, E. E., Proc. 1st. Conf. on Dense Z-pinches for Fusion, Alexandria, U. S. A., 1984.

Schlachter, J. S., Ph. D. Thesis, Univ. of California (San Diego), 1982.

Scudder, D. W., Phys. Fluids 26, p.1330, 1983.

Seaton, M. J., 'Atomic and Molecular Precesses', Ed. by D. R. Bates, Academic Press, 1962.

Shearer, J. W., Phys. Fluids 19, p.1426, 1976.

Sincerny, J., 5th. I. E. E. E. Pulsed Power Conference, Arlington, U. S. A., 1985.

Smars, E. A., Arkiv for Fysik, Band 29, p.97, 1964.

Smirnov, B. M., 'Intriduction to Plasma Physics', Mir Publishers, 1975.

Tayler, R. J., Proc. Phys. Soc. B70, p.31, 1957.

Tholl, H., Z. Naturforsch. 22a, p.1068, 1967.

Tidman, D. A., Versar Inc. Report, 1971.

Zel'dovich, Y. B. and Reizer, 'Physics of Shock Waves and High Temperature Phenomena', Academic Press, 1967.

B. L. Henke and E. S. Abisu,Advances in X-ray Analyses 17, p.150, 1973.

AKNOWLEDGEMENTS.

I would like to thank all the individuals and institutions which have made this work possible. Amongst them I would like to mention:

Mr. A. E. Dangor, my supervisor, for his friendly and constant encouraging and advice,

Dr. P. Choi, for sharing his enthusiasm and expertise,

Professor M. G. Haines, for his interest in this work,

Dr. S. Lee, for his advice and assistance in the early stages of this work,

Mr. J. Westlake and Mr. J. Beckwith for technical assistance,

Dr. A. K. L. Dymoke-Bradshaw, for proof-reading the manuscript,

Miss A. Begg, for typing the manuscript,

The Pontificia Universidad Catolica de Chile, for granting a leave and providing partial financial support,

The Fondo Nacional de Becas (ODEPLAN, Chile), for finacial support,

The O. R. S. S. (U. K.), for partial finantial support.

Lastly, and by no means least, I would thank mi wife Marina for her help and permanent support and understanding along these years. Whithout her contribution this work would not have been possible.